ORNL-3239
UC-20 – Controlled Thermonuclear Processes
TID-4500 (16th ed. Rev.)

THERMONUCLEAR DIVISION PROGRESS REPORT

FEBRUARY 1, 1961 – OCTOBER 31, 1961

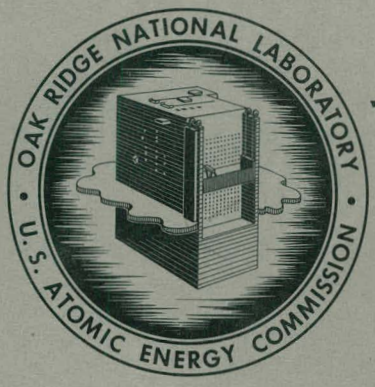

OAK RIDGE NATIONAL LABORATORY
operated by
UNION CARBIDE CORPORATION
for the
U.S. ATOMIC ENERGY COMMISSION

DISCLAIMER

Printed in USA. Price $2.25. Available from the

Office of Technical Services
Department of Commerce
Washington 25, D.C.

ORNL-3239
UC-20 – Controlled Thermonuclear Processes
TID-4500 (16th ed. Rev.)

Contract No. W-7405-eng-26

THERMONUCLEAR DIVISION PROGRESS REPORT

February 1, 1961 – October 31, 1961

DATE ISSUED

JAN 24 1962

OAK RIDGE NATIONAL LABORATORY
Oak Ridge, Tennessee
operated by
UNION CARBIDE CORPORATION
for the
U. S. ATOMIC ENERGY COMMISSION

THIS PAGE

WAS INTENTIONALLY

LEFT BLANK

Contents

THIS PAGE

WAS INTENTIONALLY

LEFT BLANK

Introduction

A. H. Snell

This is a sesquisemiannual report, covering an extended period to meet a changed Laboratory schedule for progress reports. The interval has yielded developments that place in our hands three major lines of approach to controlled fusion. The first is the classic approach of DCX-1, the second is the extended DCX concept embodied in DCX-2, and the third is radio-frequency heating, which has forced itself into prominence through preliminary experimental successes. An increased emphasis on plasma physics will also be evident in the following pages, as compared with foregoing reports in this series. All of this, of course, has been supported by invaluable work in theory, computation, magnetics, vacuum development, and engineering.

In the DCX-1 research, we now speak in terms of confinement times of *seconds* instead of milliseconds, albeit at the familiar rather modest densities of 10^8 fast protons/cm^3. As hinted earlier, this trapped circulating population of protons is not simple, and much of Sec 1 of this document describes measurements of its magnetic radiation and of its potential relative to ground, and contributes further to the discussion of the stability of the DCX-1 plasma relative to the Harris and the "negative mass" instabilities.

DCX-2 has been through a heavy phase of design and construction, and is rather lightly treated herein in relation to the work that has been involved. A recent photograph (Fig. 2.1) gives some concept of the present status, and suggests that the turn-on date may not be remote. Component testing has been encouraging; in particular, the generation of a hydrogen ion beam of 0.2 amp at 600 kev should be noted (Sec 5).

The radio-frequency heating is described in Sec 3.1. So far it has been applied only as electron cyclotron heating in a magnetic mirror configuration, but the results as summarized by the statements $\beta = 0.1$, $\tau = 0.1$ sec are remarkable. By all means look to Sec 3.1 for further details.

In other realms of plasma physics we have a wide-ranging investigation of ionic sound waves (Sec 3.2), and, as an outgrowth, a simple ballistic means of measuring plasma pressure; that is, $n_e kT_e$ (Sec 3.2.5). Methods have also been evolved for measuring ion densities and temperatures by sweeping the plasma along the magnetic field lines onto a collecting electrode (Sec 3.3). Turbulence can also be graphically seen on repeated oscilloscope traces that show the collected current as a function of time; in the circumstances of the experiment the turbulence increased with magnetic field strength and in the presence of a mirror field (Sec 3.3.3).

Vacuum arc research (Sec 4) has included more work on ion temperatures in the carbon arc. The lithium arc work has been concentrated upon the part of the arc that streams past the cathode. The deuterium arc has been given a rather comprehensive analysis, which is outlined in Sec 4.3. A hot-cathode arc in the particle density range of 10^{11}/cm^3 has been developed (Sec 4.4).

The techniques of handling ion beams of tenths of amperes are gradually being evolved. In particular, space-charge spreading seems to be tractable in at least two ways; either by deliberate injection of electrons (Sec 5.2), or by trapping the electron population yielded by the residual gas between, for example, magnetic lenses (Sec 5.1).

In theory (Sec 6) several questions are discussed that are related closely to the DCX approach, but more general aspects of plasma physics are dealt with also. A notable contribution comes from the application of existing ORNL computing methods to the forward-looking problem of the breeding ratio in a lithium-tritium fusion system; a healthy figure of 1.45 is found for a two-region, beryllium-loaded blanket (Sec 6.2).

Much of the magnetics effort during the past period has been in support of DCX-2, and does not appear explicitly in these pages. The high-field superconductors have had their impact on local thinking, however, and as they introduce a new aspect of volume optimization in coil windings while emphasizing the problem of current distribution, these matters have been studied on a rather general basis, and applied as examples (Sec 7.1).

Useful experience in vacuum technique is described in Sec 8. Apparently, under some circumstances sticking fractions of molecules on titanized surfaces can be made so close to unity that in these combinations there is little more to be gained. The comforting observation of Sec 8.4 should also be noted, in which deuterium ions of 10 to 25 kev are found to give very little sputtering of titanium, at least under normal incidence.

Our next period should be an interesting one. DCX-2 will come into operation, the radio-frequency heating will be pushed a stage further, and DCX-1 will hopefully be forced to higher densities. The construction phase of other experiments has been largely passed, and in several directions we can see how we will come to a better understanding of the problems that lie on the path to controlled fusion.

Abstracting Summary

1. DCX-1 PLASMA EXPERIMENTS

A new source featuring preanalysis of the ion beams now permits the injection of up to 10 ma of H_2^+. Modifications to the apparatus, primarily the addition of pumping by titanium films deposited on surfaces cooled by liquid N_2, reduced the operating pressure in the presence of this beam to about 1×10^{-8} Torr.

With gas dissociation, fast protons were trapped at densities of about 10^8 per cm^3 (corresponding to a 9-ma beam); the mean proton lifetimes were in excess of 5 sec, and charge exchange was the dominant loss mechanism. Studies with currents from 0.2 to 9 ma have shown no dependence of proton lifetimes on the injected current.

Studies of rf signals from the plasma region were extended to include analyses of the first four harmonics of the cyclotron radiation. Further stabilization of the 600-kv power supply allowed beam turn-on studies at the higher injected currents, and the responses of the rf signals and of the neutral-particle detectors were measured during plasma buildup.

A lithium-ion beam probe for determining plasma potentials was developed and used to measure the potential of the DCX-1 plasma as a function of pressure and injected current.

A discussion of observations pertaining to DCX-1 instability is included.

2. DCX-2

Construction of the DCX-2 apparatus is almost complete. The magnet coils were tested for strength and adequacy of cooling with satisfactory results. The accelerator was installed and found to hold its full 600 kv in the presence of the stray magnetic field. Tests of a scale model of the injection channel showed the expected magnetic shielding capability and suggested that perturbation of the external field will not be serious. Low-density lithium and deuterium plasmas are being developed for use as trapping plasmas. The vacuum system, which will make use of the ion-pumping action of the trapped plasma, has several novel features which are described.

3. PLASMA PHYSICS

Studies are continuing on the plasma formed by heating electrons at the cyclotron frequency (3-cm, 0.75-kw microwave source) in a magnetic-mirror configuration. Two distinct regimes of operation are demonstrable: a low-pressure regime (5×10^{-6} mm Hg) in which the density ranges from 10^9 to 10^{10} particles/cm^3 and the electron temperature is greater than 0.1 Mev, and a high-pressure regime (10^{-5} mm Hg) in which densities are greater than 10^{12} particles/cm^3 and electron temperatures are about 5 kev. This plasma is very highly ionized, as evidenced by neutral-beam-transmission experiments. Determinations of energy density and temperature were made in the two regimes. Results and techniques are described.

The original evidence concerning the existence of ionic sound waves is supported by subsequent experiments. They are more completely investigated in mode I arcs. An addition and correction to a recent paper by F. W. Crawford on ionic sound waves in discharge tubes is discussed. Ionic sound waves are shown to occur in a spherical discharge tube in the absence of an applied magnetic field. The axial pressure exerted by a magnetically confined plasma is measured and used to determine the electron temperature or density.

A new method of measuring the average ion density in magnetically supported plasmas is discussed. This method, called the "plasma sweeper," may perhaps measure ion temperature and the ion velocity and density distributions. The method is applied to a volume of plasma formed at the intersection of an electron stream and a gas jet. The results imply turbulence in the plasma which increases with increasing magnetic field

strength. The effect of adding magnetic mirrors to further contain the plasma is reported.

4. VACUUM ARC RESEARCH

The Carbon Arc

Ion temperatures in a long (84-in.) magnetically confined carbon arc are about 1,400,000°K at a point 72 in. from the anode. The line profile of λ4647 A of C^{2+} is Gaussian, suggesting that thermalization of these ions does exist.

The Lithium Arc

High-resolution spectroscopic studies revealed Doppler shifts (anode-to-cathode drifts and transverse precession) and broadening of Li^+ lines in the long (120-in.) solenoid. Electron excitation temperature, as measured from relative intensities of Li^+ lines, appears to be low (~2 ev). No Li^{2+} lines were observed with certainty.

The Deuterium Arc

Investigation of the high-vacuum deuterium arc plasma was oriented toward the measurement of basic properties, intercomparison of measuring techniques, and effects of parameter changes on the properties. The measurements were predominantly spectroscopic, supplemented by Langmuir-probe and microwave measurements. The properties investigated include ion and electron densities and temperatures, current oscillations, and cyclotron radiation. It is concluded that the plasma column is relatively quiescent and stable.

5. ION PRODUCTION, ACCELERATION, AND INJECTION

Further development of the injector system for DCX-2 is reported. The tube has been operated at a voltage of 700 kv, and has produced a mixed-ion beam of 100 ma at 650 kv, and 215 ma at 630 kv. At the upper current limit the external x-ray field causes voltage breakdown in the air around the tube. New electrodes with internal lead shielding were built to reduce this effect. Changes in electrode shape have greatly reduced cleanup time. The ion beam in the field-free region below the magnetic solenoid lens is self-space-charge neutralized. This effect was first observed in the 100-kv beam analysis facility when a magnetic solenoid lens was used. Such a lens permits electron trapping by the space-charge field of the beam.

A hollow-cathode reflux-type arc discharge, which serves as ion source, was combined with an electron gun for a study of ion current output. The electrons are injected axially through the cylindrically symmetric ion source along lines of magnetic flux. Thermal power measurements of a 7-kv argon-ion beam output were made with and without electron injection. In the latter, ion currents are as expected under space-charge-limited operation. With electron injection, the target power goes up by a factor of 10, while power dissipated on the accelerating electrode goes up by a factor of only 2 to 3.

6. THEORY AND COMPUTATION

Topics discussed are as follows: Fokker-Planck coefficients for a plasma, including cyclotron radiation; the tritium breeding ratio in a fusion reactor blanket; the energy distribution of ions and electrons in DCX after burnout; the dissociation of H_2^+ by electrons and protons; instability in DCX-1; a possible approach to the mode I–mode II transition problem; stable plasmas; instabilities in a homogeneous anisotropic plasma; electrostatic ion cyclotron plasma instabilities in a two-fluid hydrodynamic theory; reduction of the Vlasov equation; calculations of H_2^+ orbits in the dip region of DCX-2.

7. MAGNETICS

Optimization of superconducting solenoids is discussed with regard to both conductor volume and current distribution. The methods of optimization are illustrated by examples.

Calculations are made of the effect of dislocations of coils upon the uniformity of the magnetic field that they produce in iron-free configurations. Lateral, angular, and axial displacements are treated, as well as current changes.

8. VACUUM SYSTEMS AND TECHNIQUES

Work is reported on getter pumping by vapor-deposited titanium films, calibration of ionization gages in magnetic fields, calibration of gages with different gases, and results of accelerated decomposition tests on some diffusion-pump oils. Results of energetic deuteron bombardment on titanium are presented, in which at normal incidence deuterons of 10–25 kev are found to give inappreciable sputtering.

9. DESIGN AND ENGINEERING

A numerical summary of design and fabrication activities of the Engineering Services Group is given. Significant engineering contributions are usually described as parts of the various project activities.

THIS PAGE

WAS INTENTIONALLY

LEFT BLANK

1. DCX-1 Plasma Experiments

C. F. Barnett
J. L. Dunlap
R. S. Edwards
G. R. Haste
L. A. Massengill
H. Postma
J. A. Ray
R. G. Reinhardt
W. J. Schill
R. M. Warner
E. R. Wells

1.1 ENGINEERING MODIFICATIONS

The previous progress report[1] described engineering modifications that were then being made. These included (1) installing a new ion source, with analysis between the source and the 600-kv accelerator tube; (2) mounting a 10,000-liter/sec Varian Vaclon pump at the bottom of the main vacuum tank to dispose of the undissociated portion of the H_2^+ beam; and (3) adding pumping by batch evaporation from titanium-clad tantalum filaments to the liner and the intermediate vacuum regions. These modifications were completed near the beginning of the present report period.

The initial tests of the new ion source showed that although as much as 20 ma of H_2^+ could be accelerated to 600 kev, the requirement of a proper beam focus inside the vacuum tank limited the maximum current to 5 ma. Attempts to improve the focus at higher currents by changing the potential distributions in the first stage of the accelerator tube were not successful. A pair of electrostatic quadrupole lenses was then installed at the base of the tube. These lenses and careful alignment of the beam injection system to compensate for the effects of the stray magnetic field have allowed the injection of up to 12 ma of H_2^+ with the acceptable $\frac{1}{4}$-in.-diam spot focus. Ten milliamperes of H_2^+ is normally easily obtainable.

With the proper H_2^+ focus, scans across the undissociated portion of the beam after it had emerged from the inner vacuum region showed that it had a considerably larger divergence than was previously thought. (The beam was to have passed through the bottom of the vacuum tank and then to have impinged on a target mounted within the Varian pump.) This wide divergence required that the beam target be much closer to the aperture through which the beam emerged from the inner vacuum region. The Varian pump was removed and the beam was then stopped near the aperture on a rotating water-cooled copper drum. Pumping was provided by continuously evaporating titanium onto the drum. This rotating target is essentially that described in a previous report.[2]

With a ~.5-ma beam the revised vacuum system operated with base (ion gage) pressures of 1.5×10^{-8} Torr in the liner region. The encouraging response of the trapped proton containment time to the reduction in operating pressure (Sec 1.2) prompted additional modifications designed to produce even lower pressures at higher H_2^+ beam currents. These modifications consisted in the following:

1. Adding a resistance-heated superheater section in a steam line to the high-vacuum liner. The superheater allows baking at temperatures to 225°C.

2. Removing the section of the liner that ties the plasma region to the H_2^+ beam tube. This permits part of the gas load from the beam-tube region to be pumped by the intermediate vacuum system, and provides space for mounting two additional titanium evaporators in the intermediate region. These alterations are shown in Fig. 1.1.

[1] *Thermonuclear Div. Semiann. Progr. Rept. Jan. 31, 1961*, ORNL-3104, p 16.

[2] *Ibid.*, pp 79–82.

3. Changing the configuration of the liner to reduce by a factor of 10 the size of the apertures through which the H_2^+ beam passes. This change reduced the conductance between the liner and the higher-pressure region surrounding the rotating titanium target for the undissociated H_2^+ beam. (See Fig. 1.1.)
4. Adding an oil diffusion pump with a bakeable cold trap to pump on the liner region. (See Fig. 1.1.)
5. Adding in the liner region two small cold traps suitable for operation with liquid helium.

The latest modifications have resulted in lower base pressures (to 5.5×10^{-9} Torr without the H_2^+ beam) and longer proton lifetimes (twice as long). The response of the vacuum system to a 10-ma H_2^+ beam has been encouraging. With titanium freshly deposited onto liquid-nitrogen-cooled surfaces, the pressure rise associated with this beam is less than 1×10^{-9} Torr (ion-gage pressure) in both the liner and intermediate regions. The effectiveness of the surface pumping gradually decreases. Two or three hours of normal operation result in pressure rises of about 10^{-8} Torr in the intermediate region but only about 10^{-9} Torr in the liner region. Other modifications to produce lower operating pressures are being explored.

A series electronic regulator, designed by R. A. Dandl and F. T. May,[3] was refined and installed to stabilize the 600-kv power supply against rapid fluctuations that would otherwise be induced by corona, power-supply ripple, or changing the H_2^+ load. Stabilization against the effects of corona and ripple has reduced the modulation level of the the H_2^+ beam by a factor of 3. Oscilloscope traces of the current to the rotating target show that the H_2^+ beam now turns on with a 50-μsec rise time. Without the regulator, the rise time can be as long as 150 msec.

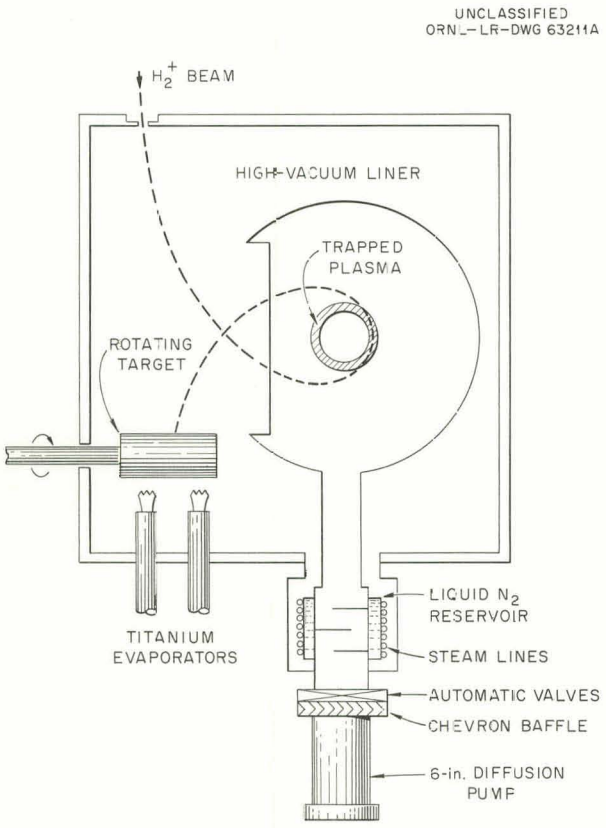

Fig. 1.1. Schematic Drawing of the DCX-1 High-Vacuum System.

1.2 MEASUREMENTS OF TRAPPED-PROTON LIFETIME

There is a radial flux of energetic neutral hydrogen atoms from the plasma region as a result of electron-capture collisions between the circulating protons and residual gas molecules. In these experiments some of the energetic neutrals were passed through a 10^{-5}-in.-thick nickel foil, centered on the median plane, to establish a charge-state equilibrium; the emerging beam, essentially all protons, was monitored by a Faraday cup. The current from the cup was amplified by a transistor circuit and then displayed on an oscilloscope. Photographs of the oscilloscope trace after interruption of the H_2^+ beam provided curves of the decay of the fast-proton density. The lifetime of the circulating protons was defined as the time interval required for the trace to decay to $1/e$ of the steady-state value.

Figure 1.2 is a plot of the reciprocal of the lifetime of the circulating protons as a function of pressure for plasmas established by dissociation in helium, hydrogen, and background gas. The H_2^+ beam was 1.4 ma, and the steady-state fast-proton density was about 10^7 cm^{-3}. Also shown are the reciprocals of the lifetimes calculated from the loss of 300-kev protons by charge-exchange

[3] F. T. May, *Thermonuclear Project Semiann. Rept. July 31, 1959*, ORNL-2802, pp 75–78.

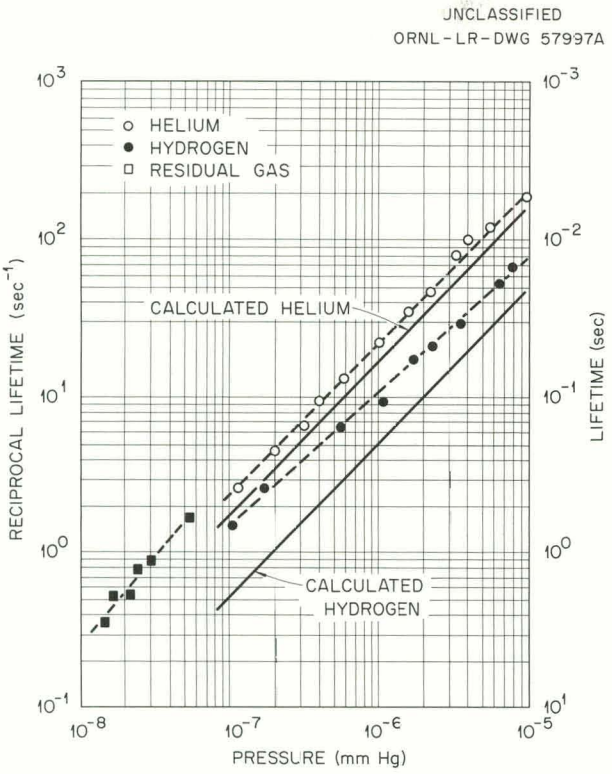

Fig. 1.2. Reciprocal Lifetime as a Function of Helium, Hydrogen, and Residual-Gas Pressure for Gas Dissociation of a 1.4-ma H_2^+ Beam.

collisions in each gas. The deviation of the hydrogen curve from a 45° slope results from the presence of background-gas contaminants with larger electron-capture cross sections. This effect is less pronounced in the case of the helium run, and the helium curve has a 45° slope. For helium the measured lifetimes are 80% of the calculated. For hydrogen at the higher pressures, where the effects of contaminants are the smallest, the measured lifetimes are 60% of the calculated. The discrepancies can be accounted for in terms of the effects of contaminants, errors in measurements, and the energy lost (approximately 10 kev) by the protons through ionization and excitation collisions with the gases.

The residual-gas curve of Fig. 1.2 was obtained by cooling the liner which surrounded the plasma region with liquid nitrogen and photographing the neutral-particle-detector decay traces as the pressure decreased. The reciprocals of the lifetimes are plotted at the pressure indicated by the ion gage, which itself was operating at ambient room temperature. The lowest indicated pressure during this run was 1.5×10^{-8} Torr, where proton lifetimes of 3 sec were observed.

The neutral-particle-detector decay traces were exponential throughout the range from base pressure to 1×10^{-5} Torr. Figure 1.3 is a semilogarithmic plot showing the exponential character of a decay with a time constant of 3 sec.

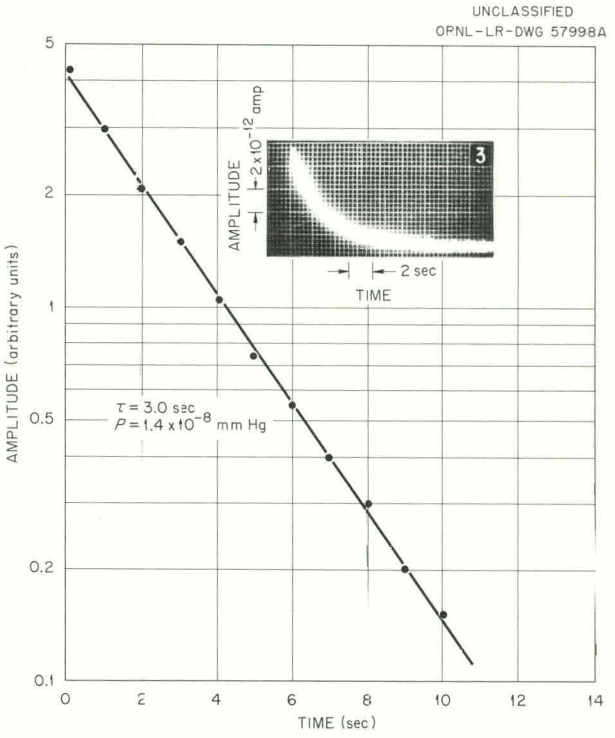

Fig. 1.3. Amplitude of Neutral-Particle Detector Signal as a Function of Time.

After additional efforts to achieve lower operating pressures were completed (the second series of modifications described in Sec 1.1), several other gas dissociation runs were made. Operation has been possible at pressures down to 1×10^{-8} Torr, and proton lifetimes greater than 5 sec were observed. From 1×10^{-8} to 1×10^{-5} Torr the pressure response of the proton lifetimes was examined as a function of current in the range from 0.2 to 9 ma. No dependence of lifetime on injected current was detected. The steady-state amplitude of the neutral-particle-detector signals varied essentially linearly as a function of pressure and as a function of the injected beam current. The amplitude profiles of signals from three neutral-particle detectors displaced slightly from one another along the magnetic field lines were sensitive to changes

in the Z-extent of the circulating plasma. These profiles showed the usual slight contractions with increases in pressure and indicated no dependence on injected current in the range investigated, which was 1 to 5 ma.

Comparisons have been made of plasma buildup and decay times with a 10-ma beam at pressures down to about 1×10^{-8} Torr. At high pressures (beginning at about 4×10^{-8} Torr) the oscilloscope traces of the neutral-particle-detector signals showed exponential buildups and decays with the same time constants. As the pressure approached the base, the buildup traces became much sharper than exponential and indicated that the plasma buildup times were shorter than the decay times, which remained exponential. The character of the buildup traces near base pressure and the failure to observe the predicted effects (see Sec 1.6) are not yet understood.

1.3 MEASUREMENTS OF RADIO-FREQUENCY SIGNALS

Work has continued on measurements of ion cyclotron radiation from plasmas accumulated by gas dissociation of the H_2^+ beam. The magnetic-induction field picked up by an electrostatically shielded loop antenna mounted in the median plane has been studied with a set of harmonic analyzers tuned to the first four harmonics. Figure 1.4 is a diagram of the equipment employed for these observations. Figure 1.5 shows oscilloscope photographs representative of those obtained during steady-state operation and during the time of plasma buildup immediately after injecting the H_2^+ beam.

The steady-state photographs show strong modulation of harmonics at frequencies near 100 kc. The patterns suggest that the second, third, and

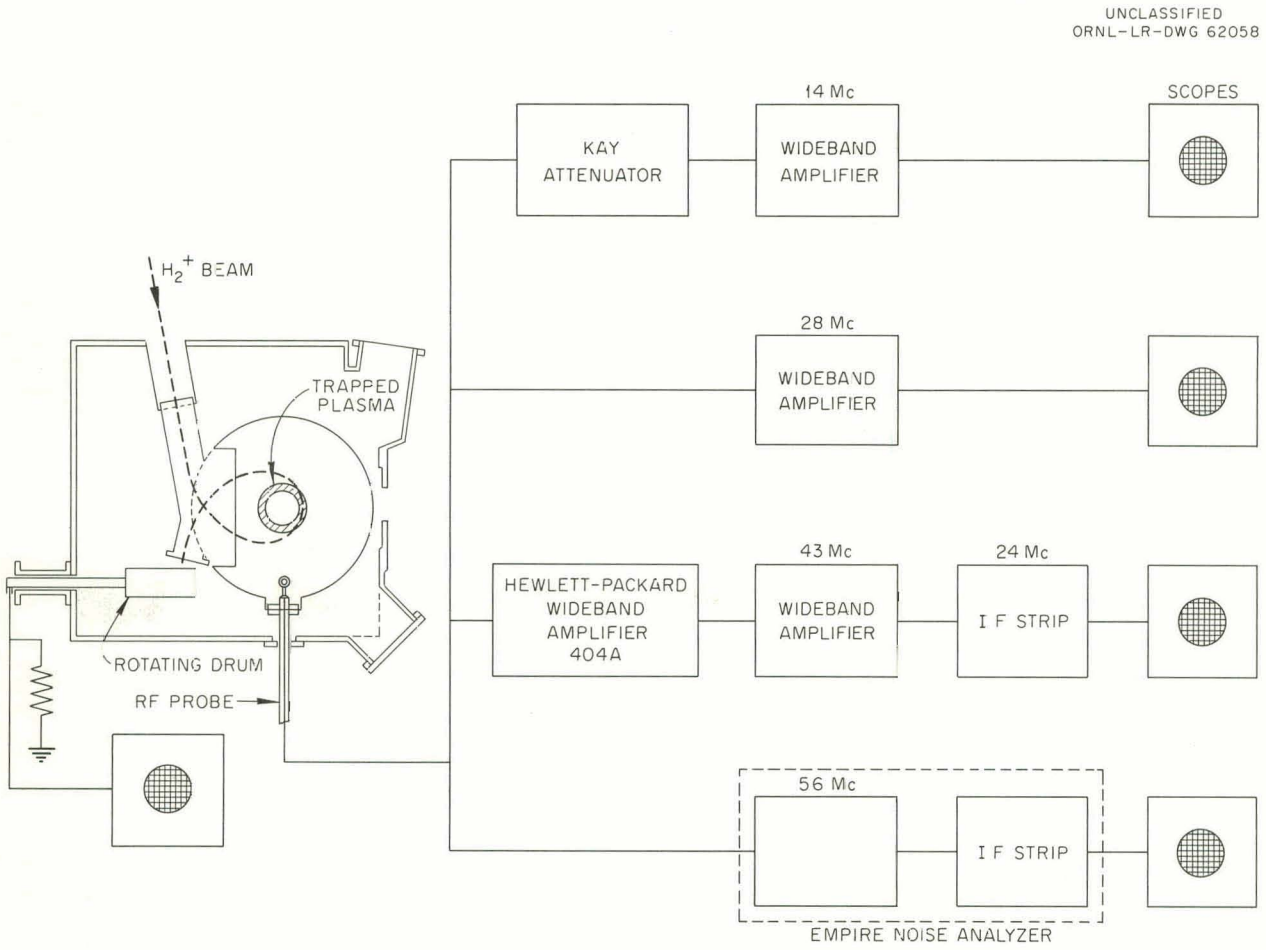

Fig. 1.4. Equipment Diagram of Harmonic Analyzers for RF Measurements.

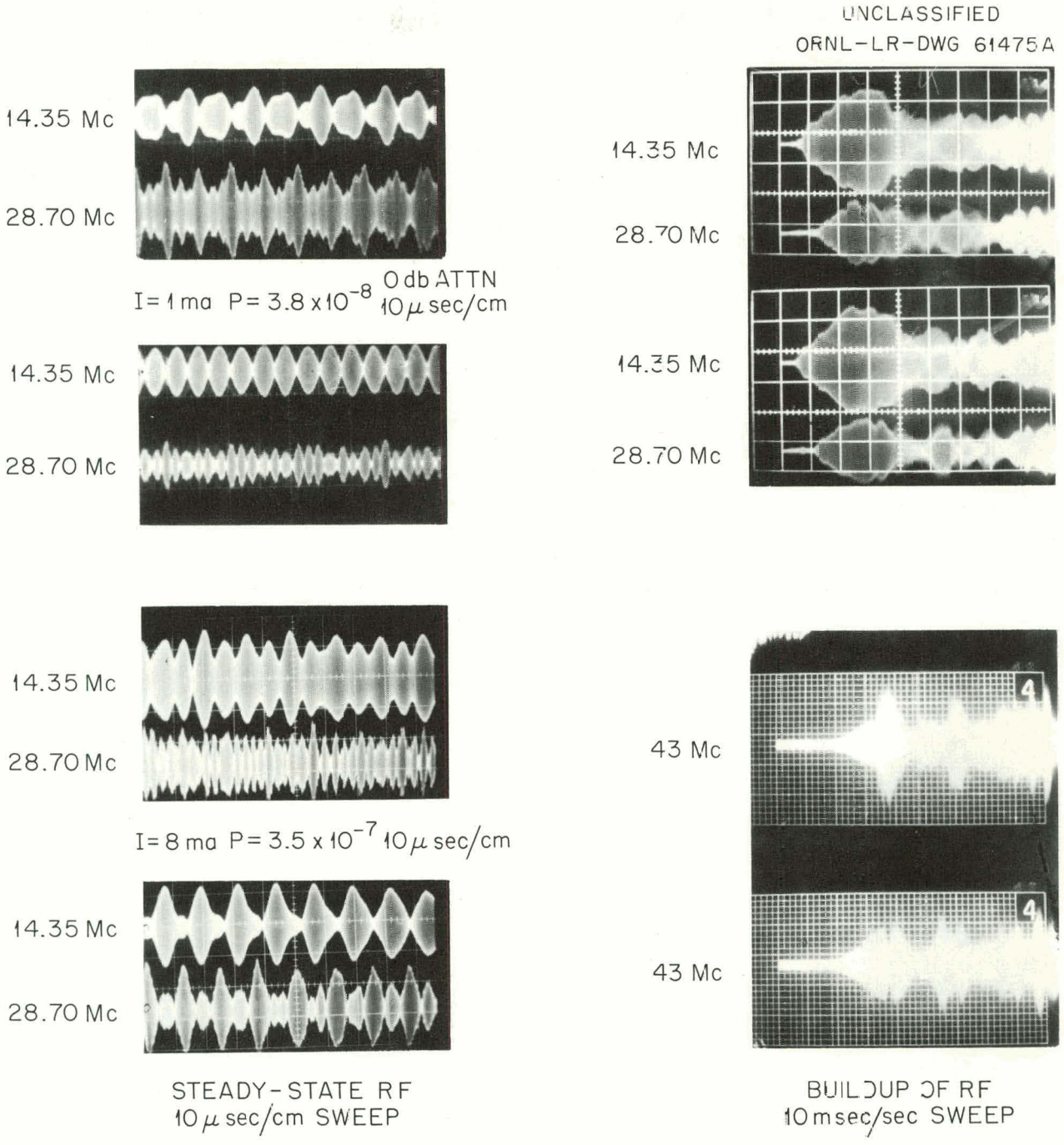

Fig. 1.5. Oscillographs of Cyclotron Radiation from DCX-1.

fourth harmonics are modulated in phase with each other but out of phase with the fundamental. At the lower pressures (less than 10^{-5} Torr) the intensities of the radiation in the successive harmonics are in the approximate ratios 10:4:1:0.1. At fixed pressures the amplitude of each of the harmonics varies approximately linearly with the injected current.

The series of photographs taken during plasma buildup have certain common features: a quiescent

interval following the injection of the H_2^+ beam before the appearance of significant radiation, a smooth increase in intensity to a peak value, and then modulation about a reduced amplitude level.

The interval of quiescence increases with the order of the harmonic, and for each harmonic the interval varies nearly inversely with H_2^+ beam current. The intervals also become shorter as the pressure is increased. Correlations with buildup of the fast-proton density at a number of pressures and H_2^+ currents suggest that the intervals are linked to the fast-proton density, though perhaps not directly. The quiescent period of the fundamental appears to end when this proton density builds up to about 10^6 cm^{-3}. The proton densities at which the quiescent periods of the first three harmonics end appear to be in the ratios of about 1:2.5:5.

The character of the cyclotron radiation is unchanged, and the amplitude is reduced only slightly, by no more than a factor of 2, when the plane of the loop antenna is rotated perpendicular to the median plane.

1.4 MEASUREMENTS OF PLASMA POTENTIAL

A lithium-ion beam probe has been used in investigating the space potential of the plasma formed by gas dissociation of the H_2^+ beam in DCX-1.[4] A beam of positive ions from a thermionic source at one end of the apparatus is accelerated through a variable potential and then directed along lines of magnetic induction to intersect the plasma torus. In the range of plasma densities and background gas pressures in which DCX-1 operates, calculations indicate that the effect on the lithium beam of charge exchange, further ionization, or scattering is negligible. The ions are able to penetrate the plasma barrier and register at a Faraday cup at the other end of the apparatus only if the acceleration potential exceeds the plasma potential. Thus the plasma potential with respect to the container walls can be determined from the transmission of the ion beam as a function of the acceleration potential.

In preliminary tests, the plasma region was simulated by a long hollow cylinder mounted coaxially with the source. For several values of acceleration potential the transmission of the ion beam was observed as the potential of the cylinder was varied. The transmission was independent of this potential until it reached the value of the acceleration potential, where a sharp cutoff less than 1 v wide occurred. These tests indicated that the beam from the ion gun is essentially monoenergetic.

Figure 1.6 shows plots of the collector current as a function of the acceleration potential which are representative of measurements made with and without the plasma present. The definition of the plasma potential is indicated. This potential is given in Fig. 1.7, as a function of helium pressure for various injected currents. The potential developed at the lowest pressures was about 70 v/ma of injected beam. A more approximate linear dependence was preserved as the pressure was increased to 10^{-6} Torr. The validity of the points above 2×10^{-6} Torr is questionable, since the collector also measures a fluctuating current of slow ions formed by ionization of the background gas in the plasma region. Above 2×10^{-6} Torr this current is comparable to that of the lithium beam itself, which is about a microampere.

In contrast with the sharp cutoffs observed in the preliminary tests, the measured cutoffs typically extend 30 or 40% about the acceleration potential required for 50% transmission of the ion beam. These gradual cutoffs are taken as evidence for fluctuation of the plasma potential. With the accelerating potential set for 50% transmission of the beam, the signal from the lithium-ion collector

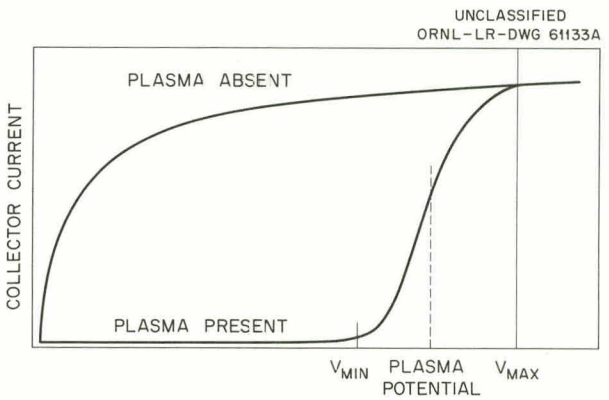

Fig. 1.6. Representative Plots of Collector Current as a Function of Accelerating Potential.

[4] G. R. Haste and C. F. Barnett, to be published in the *Journal of Applied Physics*.

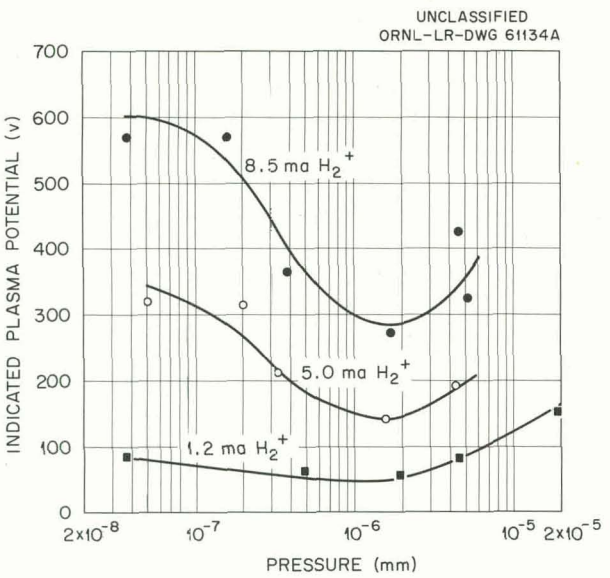

Fig. 1.7. Plasma Potential as a Function of Helium Gas Pressure for Various Injected Currents.

has been examined for modulation due to a fluctuating potential. Strong variations were evident, with periods of a fraction of a second.

The rf spectrum from the circulating plasma, the proton containment times, and the plasma volume (as determined from the longitudinally displaced neutral-particle detectors) are not affected by the presence of the lithium beam. It does not appear then that any complicated interaction of the two ion streams is taking place.

1.5 DCX-1 INSTABILITY

That the protons in the trapped ring might be "bunching" was advanced as a tentative explanation for certain observations presented in the previous progress report.[5] These observations included features of the energy distributions of the circulating protons, of optical radiation from the plasma region, and of rf signals in the magnetic-induction field near the trapped plasma. More recent studies (Sec 1.3) have added information gained from harmonic analysis of the rf signals.

The plausibility of this explanation can now be more firmly established by a number of largely qualitative arguments, which are presented in this section along with some as yet unanswered questions that relate to the subject.[6]

The first arguments concern the effects of charge bunching on the energy distribution of circulating protons. If bunching develops, there appears a potential well (or wells) rotating with the bunches at cyclotron frequency, and ions oscillate relative to the minimum of this rotating well. In the rotating frame, the kinetic energy relative to the potential minimum ϕ is just $e\phi$, and the spread in relative velocities is $\Delta v = \pm\sqrt{2e\phi/m}$. In the laboratory frame, however, the energy spread due to the oscillations is amplified to $\Delta E = 4\sqrt{(e\phi)E}$. For DCX-1 E is about 300 kev. For $e\phi$ = 300 ev, ΔE = 40 kev, which is the order of the measured energy spreads with arc dissociation. The smaller spreads observed with gas dissociation could be associated with the smaller space-charge potentials to be expected in the lower-density situations. It appears that charge bunching could result in ϕ values of the order required to produce the observed energy spreads. Some features of the work with the lithium-ion beam (Sec 1.4) indicate wide fluctuations in the potential sensed by this probe, and these fluctuations may be those associated with the rotating charge clumps.

The role of charge bunching in accounting for the shift in energy distributions to lower energies with increasing H_2^+ currents is not so clear. Models can be proposed that contribute to such an effect, but these will not be presented here since there are very few other data in support of the models. In addition, the recent observations (Sec 1.2) of proton lifetimes independent of a wide variation of injected H_2^+ current indicate that with gas dissociation the dependence of the proton-energy loss rate on injected current is not nearly as severe as was earlier suspected. More measurements of the proton-energy distributions are planned.

The magnitude of the signals from the magnetic pickup loop indicates coherence in ion motion, which is a consequence of charge bunching. With gas dissociation of an 8-ma H_2^+ beam at 2×10^{-8} Torr, the magnitude of the fundamental is that

[5] C. F. Barnett *et al.*, *Thermonuclear Div. Semiann. Progr. Rept. Jan. 31, 1961*, ORNL-3104, pp 1–10.

[6] Numerous people have contributed to discussions leading to these arguments. We wish to particularly cite the contributions of C. E. Nielsen and K. R. Symon of MURA, E. G. Harris of the University of Tennessee, H. S. Robertson of the University of Miami, and T. K. Fowler of the Physics Division.

which would be caused by bunches of about 10^9 ions.

The modulation patterns shown in steady state by the fundamental (Fig. 1.5) have been closely reproduced in a laboratory model of the DCX-1 radiating plasma. Three loop antennas with the diameter of the circulating plasma were mounted in a copper cavity that resembled the high-vacuum liner. These antennas were positioned in the median plane, and each was connected to a separate signal generator tuned to 15 Mc. A magnetic pickup loop of the type used in DCX-1 was also mounted in the median plane. The position of this loop relative to the radiating loops was the same as that of the loop in DCX-1 relative to the circulating protons. Modulation patterns similar to those of Fig. 1.5 were obtained at the pickup loop by tuning one or two of the signal generators to slightly different frequencies. This experiment suggests that the modulation patterns observed in DCX-1 could be caused by the rotation of bunches at slightly different frequencies, such as would arise from bunches at slightly different radial or longitudinal positions and hence at different magnetic-field values.

In the model, rotating the plane of the pickup loop perpendicular to the plane of the radiating antennas reduced the signal level (at 15 Mc) by a factor of about 200. In measurements on the DCX-1 apparatus (Sec 1.3) the reduction was not as great as a factor of 2. These observations suggest significant variations of longitudinal current in the trapped ring. Longitudinal currents are presumably present in the form of electrons oscillating along field lines in response to periodic potential fluctuations caused by the rotating charge clumps. These oscillations, however, should be nearly symmetric with respect to the median plane, and magnetic-field variations induced by them at the position of the pickup loop should largely cancel. A more complicated model may be required to account for this feature of the observations.

Two instabilities have been suggested that provide bunching of the protons. One is the "negative-mass" instability which was initially considered in connection with magnetic storage rings of high-energy accelerators.[7] Important parameters are the linear density of the trapped ions, the negative radial magnetic field gradient, and the initial spread in angular velocity of the trapped protons. The second instability is based on the work of Harris and Burt[8] and emphasizes the oscillations of electrons along the field lines, which were ignored in the calculations of the negative mass instability. More discussion of these instabilities is given in another section of this report.[9]

The data available at present have not permitted a determination of which is the dominant mechanism in DCX-1. The rf measurements during plasma buildup showing that the interval of quiescence increases significantly with the order of the harmonic perhaps weight the data in favor of the Harris instability. This evidence is not considered definitive, primarily because of the lack of correlation with the buildup of electron density in the plasma region.

1.6 EXPONENTIATION EQUATIONS

When operating with gas dissociation, basic equations for the buildup and the decay of the fast-proton density (corresponding to gating the H_2^+ beam on and off) are:

1. (Buildup) $$\frac{dn_+}{dt} = \frac{I(\Sigma n_0 \sigma_{BUO} X)}{V} + \left(\frac{I \sigma_{BU+} X}{V} - \Sigma' n_0 \sigma_{cx} v_+ \right) n_+ ,$$

2. (Decay) $$\frac{dn_+}{dt} = -(\Sigma n_0 \sigma_{cx} v_+) n_+ ,$$

where

I = injected H_2^+ current,
n_0 = neutral density,
σ_{BUO} = cross section for dissociation of H_2^+ by collision with a neutral,
X = path length for dissociation over which the protons are effectively trapped,
V = plasma volume,
σ_{BU+} = cross section for dissociation of H_2^+ by collision with a trapped proton,

[7] C. E. Nielsen *et al.*, pp 239–52 in *International Conference on High Energy Accelerators and Instrumentation*, CERN, Scientific Information Service, Geneva, Switzerland (1959); *Rev. Sci. Instr.* 30, 80 (1959).

[8] Philip Burt and E. G. Harris, *Thermonuclear Div. Semiann. Progr. Rept. Jan. 31, 1961*, ORNL-3104, pp 83–84.

[9] See sec 6.5.

σ_{cx} = electron-capture cross section for a trapped proton,
v_+ = velocity of the trapped protons,
n_+ = density of trapped protons.

When the rate at which protons are trapped by collisions on the already trapped circulating protons exceeds the rate at which trapped protons are lost by charge exchange, the coefficient of n_+ in the buildup equation becomes positive. The trapped-proton density then exponentiates to a value hopefully limited only by scattering. Calculations of the H_2^+ current required to make this coefficient positive in DCX-1 are very approximate but indicate that with the lowest operating pressures the presently available 10-ma beam might amount to a significant fraction of the required critical current. For currents below the critical value the proton density builds up with a time constant

$$\tau_B = \frac{1}{\Sigma' n_0 \sigma_{cx} v_+ - \frac{I \sigma_{BU^+} X}{V}} .$$

The decay time is determined by the charge-exchange reactions,

$$\tau_D = \frac{1}{\Sigma n_0 \sigma_{cx} v_+} .$$

The response of the DCX-1 vacuum system to the injectior of the H_2^+ beam (Sec 1.1) suggests that the two Σ terms are nearly the same; so τ_B is longer by a factor which measures the importance of trapping by dissociation on the circulating protons. Ccmparisons of buildup and decay times as functions of the injected H_2^+ current could give useful information on the value of the critical current in DCX-1.

2. DCX-2

P. R. Bell, J. S. Culver, S. M. DeCamp, J. C. Ezell, G. G. Kelley, N. H. Lazar, R. J. Mackin, Jr., J. D. G. Rather, J. C. Thompson, C. W. Wright

2.1 INTRODUCTION

The DCX concept consists of achieving a dense high-temperature plasma by accelerating ions to high energy and trapping them in a magnetic container. Several approaches are being tried: the injection and ionization of energetic neutral atoms formed by neutralizing previously accelerated charged particles (ALICE, Phoenix); high-efficiency arc dissociation of molecular ions (DCX-1 in original version); and various schemes for low-efficiency dissociation of quasi-trapped molecular ions (OGRA, DCX-2, Pivot machine, "Sinelnikov Injection," and "Wingerson's Corkscrew").

DCX-2 is conceptually the simplest of the devices in the last category. A magnetically shielded injector channel, or "snout," is used to transport molecular ions to a point near one end of a magnetic mirror machine in such a way that they will follow a tight helical path to the opposite mirror and back. The attainable path length depends upon the tightness of the helix which can be achieved. This concept was analyzed previously.[1] Several schemes for extending the path length still further appear feasible and will be exploited if found necessary.

Two other notable features of DCX-2 are the use of the ion-pumping effect of the trapped plasma to maintain a low pressure of neutral gas, and a magnetic field of such strength and scale as to make the mirror losses no greater than those predicted by adiabatic orbit theory. The design is such that any of several trapping plasmas now undergoing development may be used.

Calculations relating the attainable density to input current and various machine parameters have been given by Simon,[2] Mackin,[3] and Fowler.[4] The most recent progress report describes fairly completely the overall machine design,[5] gives details of the magnetic field and orbit calculations,[6] and reports associated component developments.[7]

The past nine months have been devoted mainly to fabrication and testing of components and to assembly of the machine. This phase is now almost complete. Except for certain components, notably the magnet coils, the detailed design was carried out by the Y-12 Engineering Division in consultation with Thermonuclear Division personnel. A late photograph, Fig. 2.1, illustrates a concluding phase of the construction program.

The following paragraphs will review the status of the various elements of the machine.

---

[1] P. R. Bell *et al.*, *Thermonuclear Project Semiann. Progr. Rept. July 31, 1960*, ORNL-3011, pp 13–29.

[2] A. Simon, *J. Nuclear Energy, Pt. C* **1**, 215 (1960).

[3] R. J. Mackin, *Nuclear Fusion* **1**, 131–38 (1961).

[4] T. K. Fowler, *Effect of Energy Degradation of the Critical Current in an OGRA-Type Device*, ORNL-3037 (Dec. 28, 1960).

[5] P. R. Bell *et al.*, *Thermonuclear Div. Semiann. Progr. Rept. Jan. 31, 1961*, ORNL-3104, pp 17–21.

[6] M. Rankin, *Thermonuclear Div. Semiann. Progr. Rept. Jan. 31, 1961*, ORNL-3104, pp 21–22; G. R. North, pp 23–24; G. R. North *et al.*, pp 24–28; W. F. Gauster, pp 101–12; P. A. Thompson, pp 113–15.

[7] J. E. Francis *et al.*, *Thermonuclear Div. Semiann. Progr. Rept. Jan. 31, 1961*, ORNL-3104, pp 49–55; R. A. Gibbons *et al.*, pp 58–63; R. C. Davis *et al.*, pp 71–75; R. L. Brown, pp 97–98, 117–20; C. E. Normand *et al.*, pp 123–25.

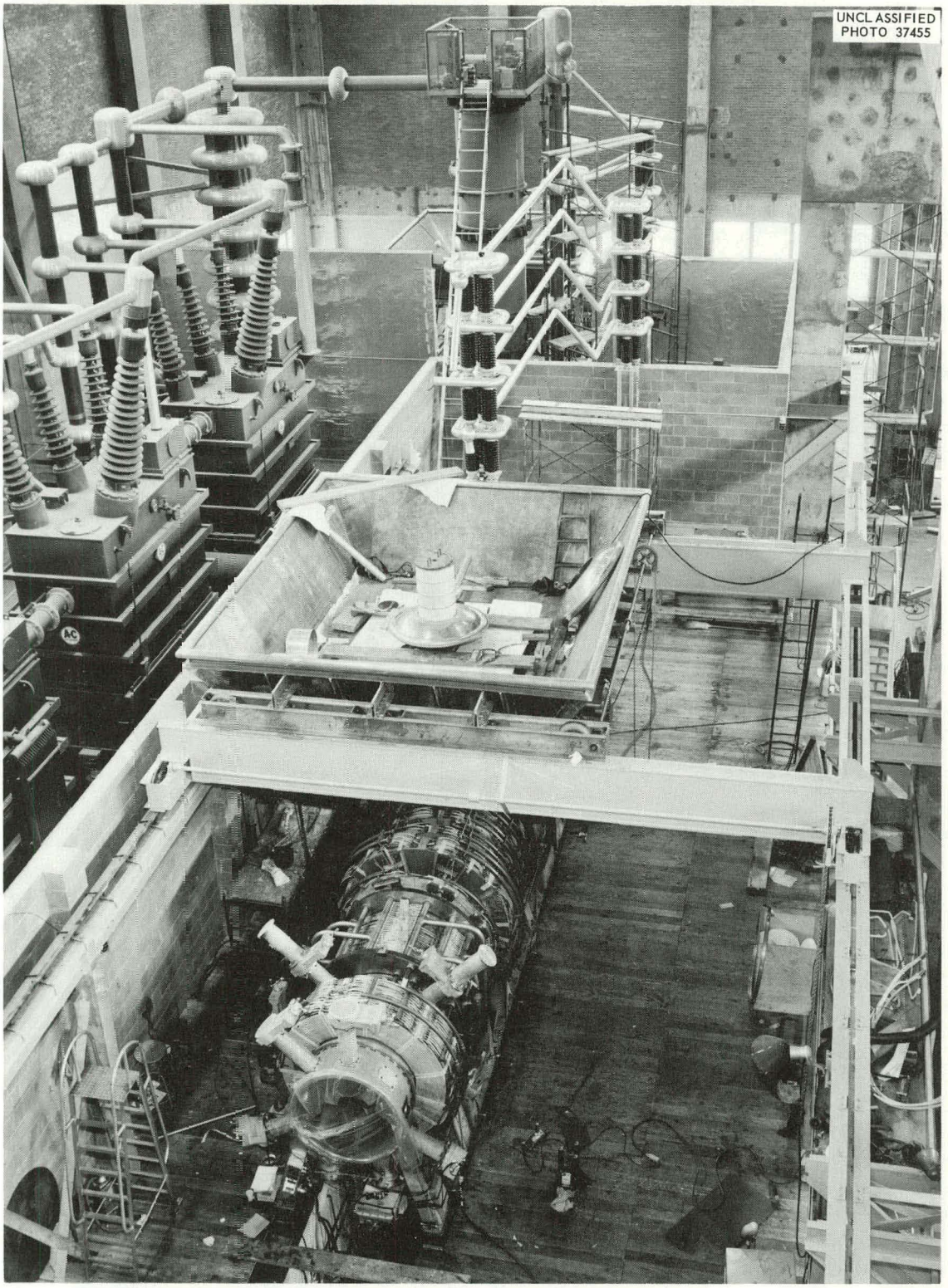

Fig. 2.1. DCX-2 and High-Voltage Supply.

2.2 MAGNET

The DCX-2 magnet system is designed to produce a mirror ratio of 3.3, a central axial field homogeneous to better than 0.1% over a length of about 1.5 m, and a field dip of about 2% at the injection point. Electrical and cooling requirements and the coil-design concept were described earlier.[1] The 12 coils which compose the system have been tested for strength under forces much greater than will be encountered in initial operation (i.e., with hydrogen injection). Coil cooling has been found adequate at twice the 10-Mw power level of the initial experiments.

The overall magnet control system is complete and is in the process of being made operational. The system includes trimming resistors and supplementary supplies for fine adjustment of the relative currents in the six central-field coils; a circuit providing for automatic trimming of these currents in order to maintain a uniform field as the current in the "dip" coils is varied; the usual interlocks with other systems; and water-flow protection for each of the more than 600 cooling channels.

2.3 INJECTION SYSTEM

Most of the components of the DCX-2 injector have been described previously.[1,7] Performance of the ion source and accelerator tube is described elsewhere in this report.[8]

At present the injector is complete and installed except for the magnetically shielded injection channel. This part has been fabricated and is being assembled.

The accelerator tube is mounted on a platform in a lead-lined tub 12 ft wide (transverse to the axis of DCX-2) by 14 ft long. The platform may be tilted through an angle of 0 to 10° about the point of entrance of the injection channel into the main vacuum system, and may be translated 4 in. along the axis of the machine. It is also provided with jacks for 2 in. of vertical motion. The tub is mounted on a bridge crane which runs the length of the main track.

Just below the tub is a pumping manifold provided with a liquid-nitrogen-trapped 10-in. diffusion pump, and air locks for two titanium evaporators like those used on the main vacuum system. The titanium vapor condenses on a removable water-cooled copper liner. Shields keep titanium vapor out of the beam.

The ion beam passes through the injection channel into the 12-kilogauss central field of DCX-2. Scale-model mechanical and magnetic tests have been carried out which indicate the validity of the design concept. The channel has a clear aperture of 1.7 in. at the tip and shields the beam for a distance of 20 in. in the high field. A target in the upper section of the channel is provided for stopping the defocused H_3^+ and H^+ components of the beam.

Correction coils on the exterior of the ferromagnetic (Hiperco) shield tube reduce the disturbance of the external field to a very small amount. Both a transverse and a longitudinal correction are required since the injector must be tilted in order to permit the beam to miss the channel on the first turn in the field. The coils require a power of about 350 kw at 2000 amp.

In a half-scale model test at 100 gauss, the field perturbation on axis at 2 in. from the tip of the duct was 1.5%. In a region corresponding to the plasma region in DCX-2, readings were within ±0.5%, the limit of accuracy of the measurement. Optimum perturbation cancellation was obtained when the longitudinal winding had the current predicted on the basis of a thin current sheet at the surface of the iron shield tube and when the solenoidal current produced a field deep in the solenoid equal to the axial component of the main field.

2.4 VACUUM SYSTEM

The design of the vacuum system in DCX-2 is predicated on the assumption that the injected beam will constitute the principal source of neutral gas. Therefore, the pumping system was designed, primarily, to handle, at only modest pressures, the very large gas quantities inherent in beams of the required magnitude.

For example, a 500-ma beam constitutes a gas load of ~ 0.1 mm-liter/sec. For the estimated conductance from the plasma region, somewhat less than 1000 liter/sec for air, a base pressure of 10^{-7} mm Hg represents only $\sim 10^{-4}$ mm-liter/sec. However, because of its larger charge-exchange cross section, each molecule of background gas is about 60 times as important as a molecule of H_2. Even so, the effective background gas throughput will will be only 6% of the H_2 throughput.

[8] R. C. Davis *et al.*, this report, sec 5.

In order to achieve the high pumping speed required to handle the injected beam, a form of ion pumping will be required. The mechanism envisioned for this purpose consists of ionizing the neutrals in the trapped plasma and, after their drift through the mirrors along field lines, disposing of them as neutrals in evaporated titanium layers on the walls of the "ballast" region. The system is designed to give this disposal process an efficiency greater than 90%. By the use of contoured tubes which follow the field lines in the mirror region, the gas conductance through the mirror was designed to be ~2000 liters/sec for H_2; therefore, 20,000 liters/sec is required to ensure 90% of the gas being pumped before returning to the plasma region. The detailed considerations leading to the design of the vacuum system have been covered previously. Figure 2.2 is an up-to-date schematic representation.

The construction and installation of the various parts of the vacuum system are now complete. The heat load resulting from fast-neutral-particle flux and arc radiation, if any, is borne on a water-cooled copper liner, shown in Fig. 2.3. The main section is constructed of two metallurgically bonded copper sheets (Roll-Bond, manufactured by Olin Mathieson Chemical Corp., East Alton, Illinois). Water passages, tailored to accommodate the heat load in the various regions, have been formed by hydrostatic inflation of the thinner, outer copper sheet to a predetermined pattern. The liner was formed by welding together several panels of Roll-Bond.

The liner surfaces will be outgassed before experiments by operating a strongly radiating energetic argon arc[9] in the machine for extended periods at low pressure. It is hoped that this treatment will also help alleviate any problems arising from large fluxes of energetic particles incident on the liner surface.

Provision was made for access into the central region of the machine through approximately 40 ports. Low-conductance joints between the inner and outer vacuum regions permit radial motion of probes and their replacement through air locks while the system is still under vacuum.

Titanium is evaporated in the ballast regions from wire wound on tantalum filaments. By using a supplementary winding of niobium nearest the tantalum, formation of molten titanium is prevented[10] and the evaporation may be carried out in a magnetic field. To assist in pumping gases not absorbed by titanium films, two PMC-4100 liquid-nitrogen-trapped diffusion pumps are also used in each ballast region. The outer vacuum region is pumped by four such pumps. The diffusion pumps are backed up by a Kinney mechanical pump-blower system.

Initial experiments with the PMC-4100 pumps[11] showed considerably greater oil backstreaming

[9]R. A. Gibbons *et al.*, *Thermonuclear Project Semiann. Rept. Jan. 31, 1960*, ORNL-2926, pp 47–51.

[10]R. E. Clausing, *Thermonuclear Project Semiann. Progr. Rept. July 31, 1960*, ORNL-3011, p 122.

[11]Consolidated Vacuum Corp., Rochester, New York.

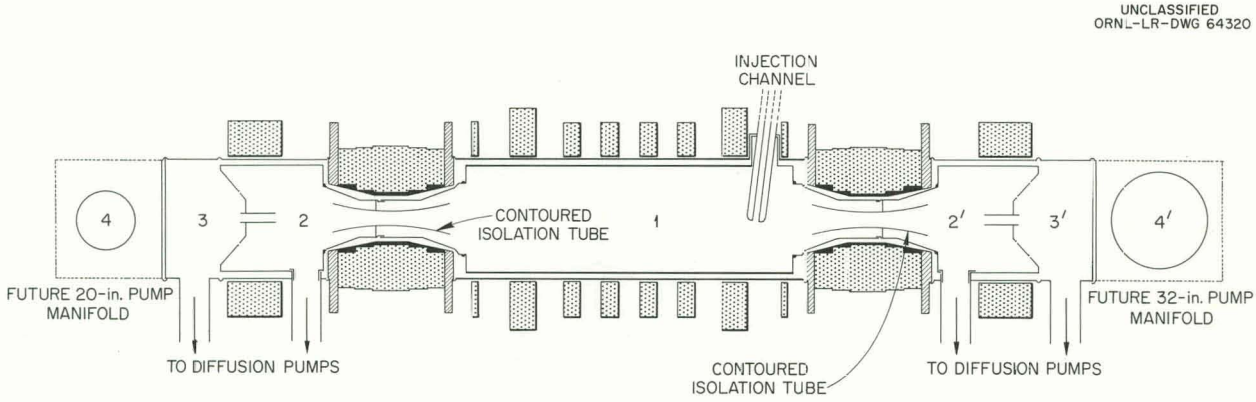

Fig. 2.2. Schematic Representation of Differential Pumping Arrangement in DCX-2. The various regions are: ballast regions, 2 and 2′; intermediate vacuum regions, 3 and 3′; and future electrode regions, 4 and 4′.

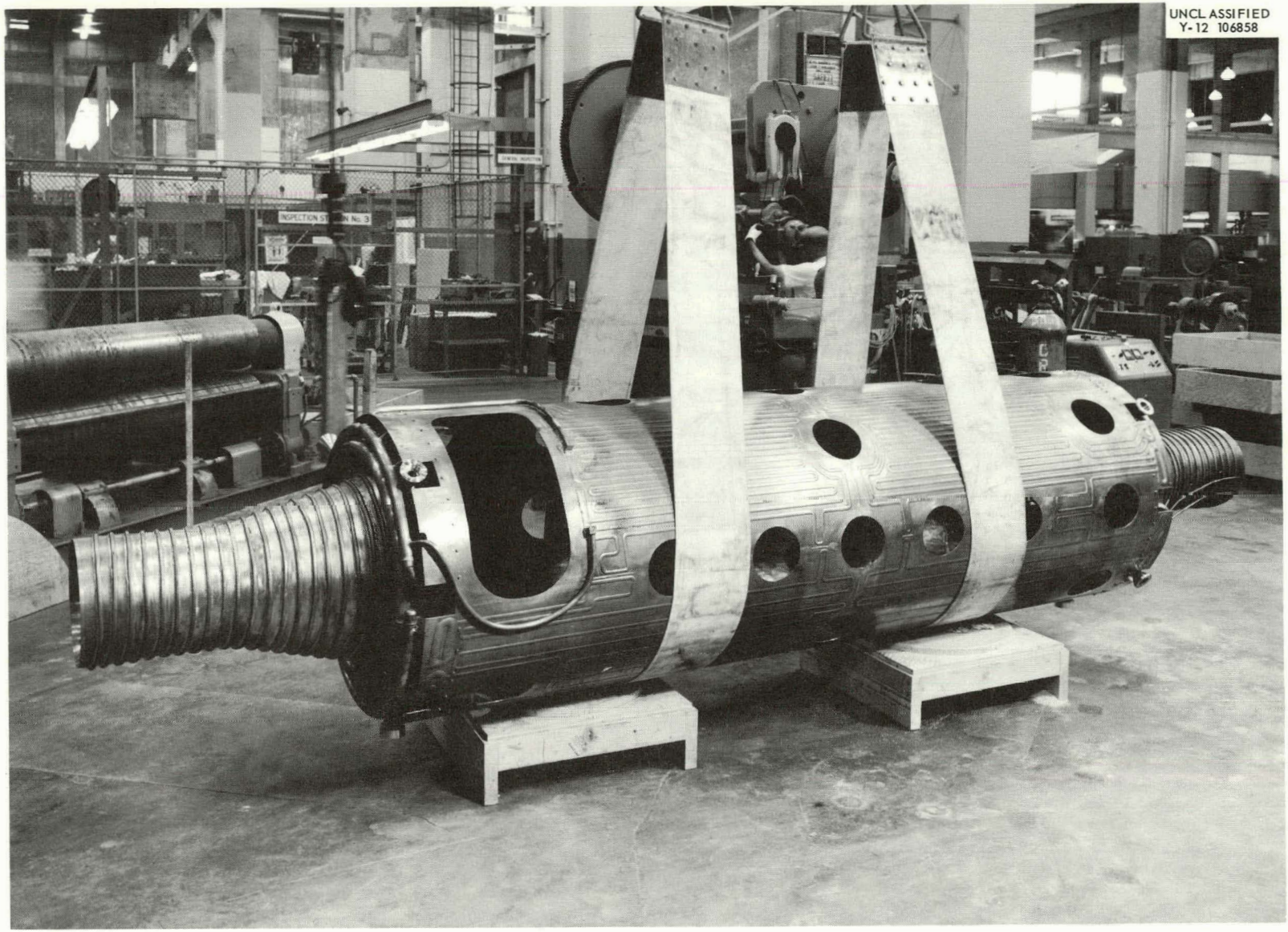

Fig. 2.3. DCX-2 Vacuum Liner.

rates from these pumps, even with water-cooled caps, than from the older MCF-1400 series pumps, or from the prototype originally tested.[12] Modification of the upper jet assembly by insertion of a heat shield and baffle is being carried out in accordance with the directions of the manufacturer, in order to reduce these rates to an acceptable level.

2.5 TRAPPING PLASMAS

Estimates suggest that the expected molecular-ion beam current may be adequate for the achievement of a dense plasma (the "burnout" condition) with no other initial trapping (dissociating) mechanism than the background gas. However, use of a low-density fully ionized cold plasma may greatly reduce the current necessary for "burnout." Several such plasmas are being developed.

It is important that the density of the cold trapping plasma not be too high[13] because of energy losses to the cold electrons. If the electrons can be heated to temperatures above a few hundred ev, the energy losses become less important.

For a carbon arc (not seriously considered at this time) an optimum density appears to lie just above 10^{11} cm^{-3}; it should not be markedly different for other arcs. Thus, the lithium and deuterium arcs presently being studied, with densities between 10^{13} and 10^{14} cm^{-3} do not appear to be directly useful. Details of this work and other arc investigations appear elsewhere in this report.[14]

---

[12] C. E. Normand, *Thermonuclear Project Semiann. Rept. Jan. 31, 1959*, ORNL-2693, pp 70–72; *Thermonuclear Project Semiann. Rept. July 31, 1959*, ORNL-2802, pp 128–29.

[13] R. J. Mackin, *Nuclear Fusion* **1**, 131–38 (1961).

[14] J. E. Francis *et al.*, this report, sec 4; R. A. Gibbons *et al.*, this report, sec 4.

3. Plasma Physics

3.1 ELECTRON-CYCLOTRON HEATING EXPERIMENT

R. A. Dandl
H. O. Eason
R. J. Kerr
A. C. England
M. C. Becker
W. B. Ard[1]

3.1.1 Experiments in the Magnetic-Mirror Configuration of the Physics Test Facility

In the previous semiannual report,[2] preliminary experiments were described on the initial heating of a plasma through electron-cyclotron resonance in a magnetic mirror. Heating at the electron-cyclotron frequency is the most effective means of transferring energy to the individual electrons. However, one is interested in the conditions that make this process efficient for heating a thermal distribution of electrons.

Initially the electrons are present with random velocities and random phases. The condition that an appreciable number of them gain energy by a resonance process is that they must effectively be brought into phase with the microwave electric field. The qualitative condition necessary for the electrons to be "phased" is that they gain an amount of energy between scattering events greater than they had initially. This requirement is fulfilled by providing sufficient electric field or, practically speaking, sufficient microwave power to heat a large number of the electrons out of the scattering-dominated distributions. When the electrons are heated, their losses are determined by the time required to scatter out of the mirrors. However, as the density increases, this scattering time decreases, less efficient stochastic processes take over, and the electrons continue gaining energy, though very slowly.

The cavity or reflecting box in which the resonance process takes place requires some description. Common characteristics of most types employed in our experiments included the following: (1) cylindrical symmetry about the axis of the magnetic mirror field, (2) excitation by the microwave electric field perpendicular to the magnetic-mirror field, and (3) water-cooled perforated copper walls for good vacuum characteristics.

The earliest cavities were excited in fundamental modes; however, it was later found that the cavities in high modes (that is, several free-space wavelengths in dimension) were satisfactory. The concept is essentially that of confinement of the microwave power in a chamber with highly reflecting walls. This chamber also surrounds the plasma which in turn provides the principal energy-dissipative element through electron-cyclotron absorption. The ability to operate in high mode situations is very significant from the practical standpoint, in that fundamental restrictions on cavity size at a given magnetic field are considerably relaxed. The principle may thus be extended to higher magnetic fields, higher densities, and other geometries which are more desirable from the controlled thermonuclear standpoint.

The more useful experiments performed with the 14-cm apparatus were the observation of microwave noise radiation, x-ray spectral measurements, molybdenum-powder experiments, and diamagnetic measurements. The first observations of the microwave noise yielded decay times (upon turning off the klystron) which were considerably longer than anticipated. One explanation for the length of the decay times was a rather high electron temperature. The scattering-loss-dominated lifetime of the electron gas was sufficiently long to require electrons in the 10- to 20-kev region.

The necessarily high electron temperature as required for these decay times indicated the possibility of x radiation from the device, and subsequent measurements were made of the x-ray spectra.

---

[1] Consultant, University of Florida, Gainesville.

[2] *Thermonuclear Div. Semiann. Progr. Rept. Jan. 31, 1961*, ORNL-3104, sec 3.1.

From these spectra a "temperature" in excess of 10 kev was inferred. Molybdenum powder was dropped through the plasma to obtain information on its geometrical configuration. Figure 3.1 is a photograph of the incandescent molybdenum powder outlining the plasma in the resonant region of the magnetic field. Some rather crudely quantitative estimates of the amount of incandescent light from molybdenum powder indicated energy densities of the order of 10^{15} ev/cm^3. These energy densities indicated that diamagnetic measurements would be feasible. If the dimensions of the plasma are small compared with the distance to the diamagnetic detector, the signal should obey a $1/r^3$ dependence. Figure 3.2 indicates that the plot of diamagnetic field intensity as a function of a radius obeys this dependence. The significance of this observation is that the plasma is small compared with the radial distance of the diamagnetic probe to the axis of the machine, indicating that cold secondary plasma was not confusing the measurement.

One of the chief limitations of the electron-cyclotron heating method of generating plasma is that strong magnetic fields require short-wavelength microwave generators. Unfortunately, very-short-wavelength microwave generators having sufficient power capability are not available. However, sufficient power is available at 3 cm, and experiments were undertaken at 3 cm to determine the efficiency of heating the plasma at higher frequencies. A 1-kw 3-cm Magnetron was employed, and significantly higher energy densities were observed.

One observation that had been made in connection with the 14-cm heating experiments was that

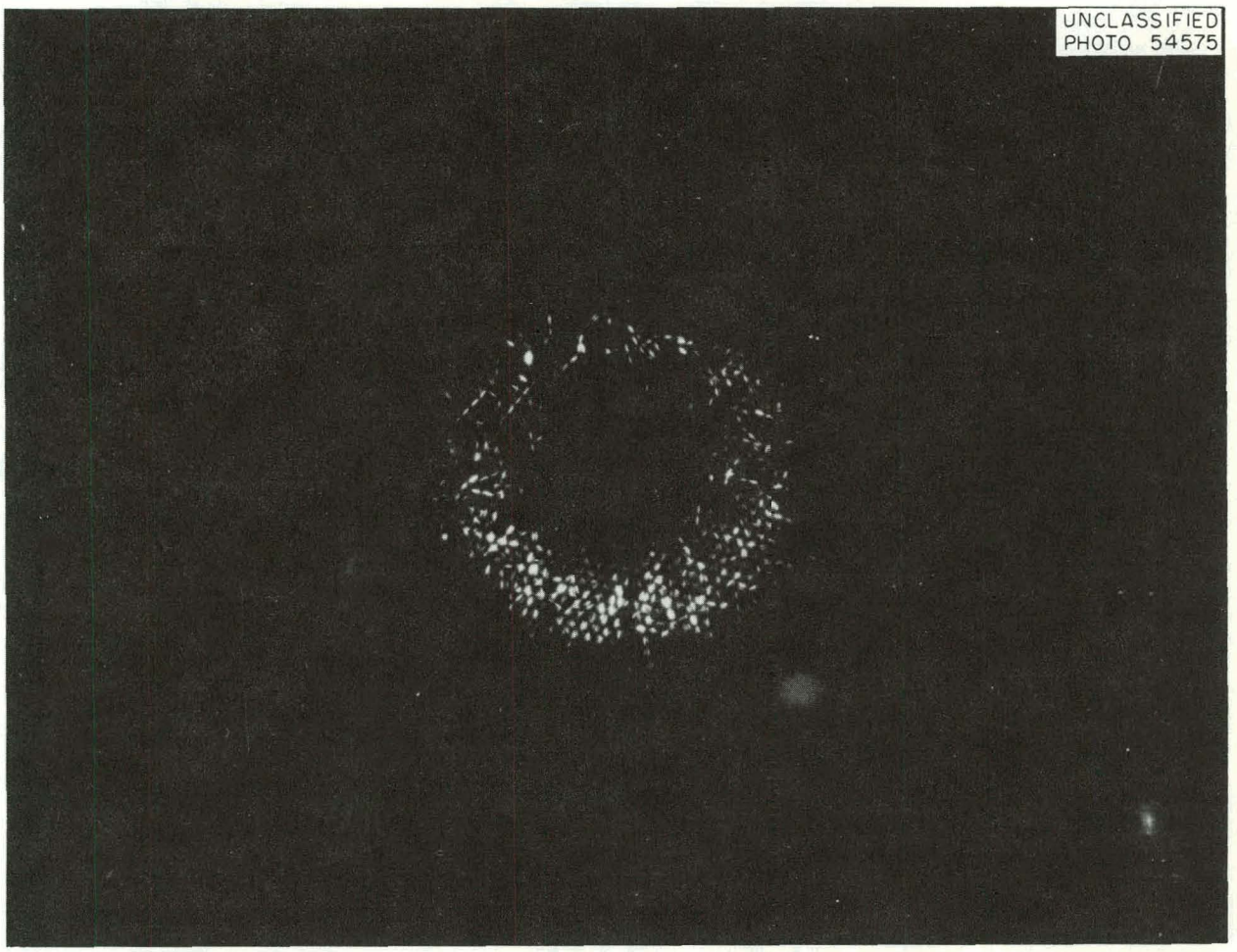

Fig. 3.1. Incandescent Molybdenum Powder Outlining the Hot Electron Plasma in the Resonant Magnetic Field Region.

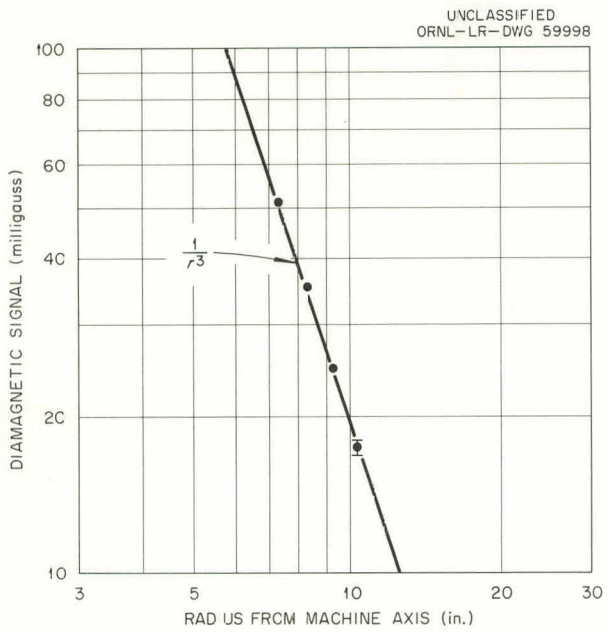

Fig. 3.2. Diamagnetic Field Intensity as a Function of Radius for Axial Resonance.

for higher gas pressures ($\sim 10^{-5}$ mm Hg) a different plasma mode appeared in the cavity. This was called the glow mode because of the bright blue glow that accompanied it. This mode had not been studied at 14 cm because it was accompanied by a very low x-ray emission. During the 3-cm experiments this mode again appeared, and it was accompanied generally by an apparently lower energy and an x-ray flux of lower intensity.

The transition between the two modes was quite sharp. If the pressure was increased while the plasma was in the high-temperature mode, an upper critical pressure was reached at which the plasma suddenly went into the glow mode. However, to cause the rapid transition to the low-pressure high-temperature mode, the pressure had to be lowered by a factor of almost 2 to a lower critical pressure.

A thermal neutral gas beam was designed to measure the density of the plasma. This beam is described in more detail in Sec 3.1.3. To date, the neutral beam transmission through the high-temperature mode has been able to give only an upper limit on the electron density. This limit is $n_e \leq 2 \times 10^{11}$ electrons/cm^3. In the high-pressure low-temperature glow mode the density has been determined as $n_e \simeq 5 \times 10^{12}$ electrons/cm^3.

Since the neutral beam was almost entirely attenuated by the plasma, it was reasonable to assume that the plasma was doing some pumping. Observations of both the end pressure of the machine and the center pressure were made and are shown in Fig. 3.3. In this figure it can be seen that raising the center pressure induces the transition to the high-density (glow) mode. After the transition, the end pressure is higher, and the center pressure is lower. Upon reducing the center pressure, the transition takes place back to the high-temperature mode, after which the end pressure drops lower. Plasma pumping is the most adequate explanation for these changes.

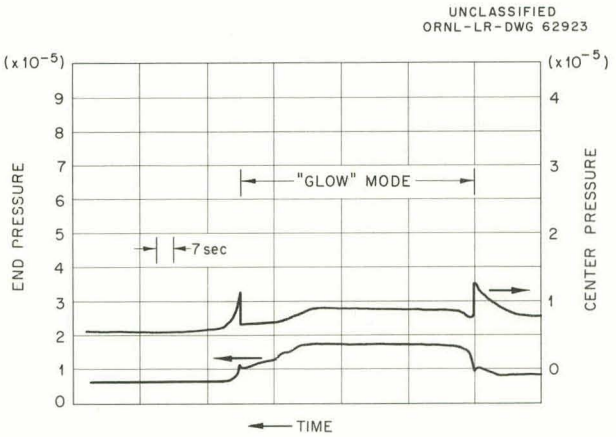

Fig. 3.3. Center Pressure and End Pressure in the PTF, Indicating the Probable Effect of Plasma Pumping.

Microwave noise was again a useful measurement parameter. Both the noise intensity and the decay time of the microwave noise were monitored. The measurements were made at 1.25 cm. The absolute radiation was measured by comparison against a noise source, and the decay time was the measurement of the e-folding time after the microwave power was turned off. The top trace of Fig. 3.4 shows the decay of the microwave noise after the microwave power was turned off. An interesting feature of the dynamic behavior is observed here. After the microwave power is turned on, the plasma immediately goes into the high-temperature low-density mode, and then it fluctuates before it passes into the high-density mode. In the high-density mode, the microwave noise is much more intense. The lower trace is a pressure indication

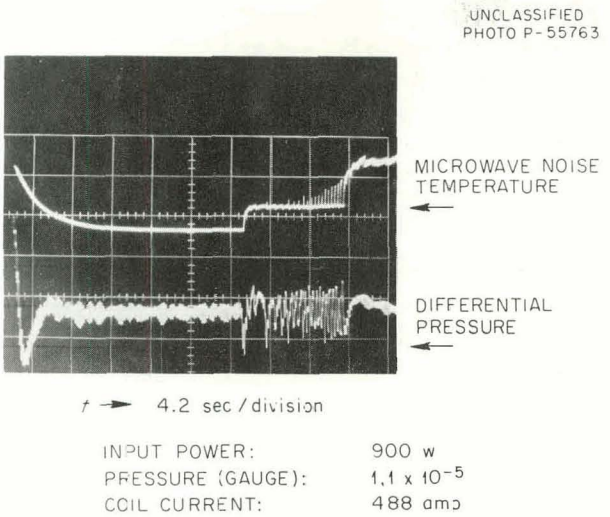

Fig. 3.4. Microwave-Noise Decay and Buildup and Differential Pressure Indication Under Pulse Conditions.

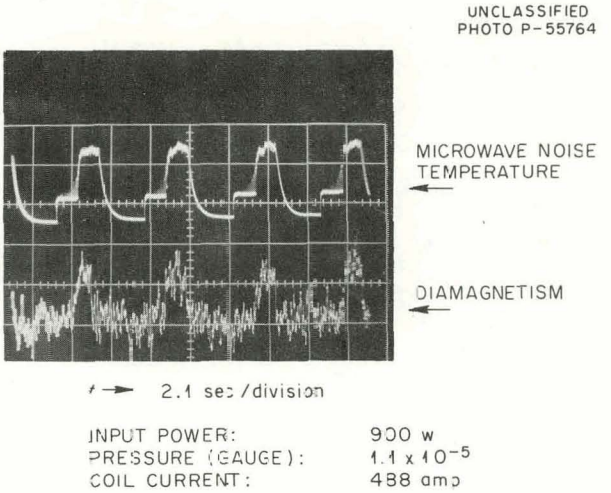

Fig. 3.5. Microwave Noise and Diamagnetic Signal for the High-Density Mode Under Pulse Conditions.

showing the pressure difference between the tank and the cavity.

In order to validate the containment time as indicated by microwave-noise decay, it seemed advisable to monitor diamagnetic signal strength as a function of time, but this was rather difficult to do. As shown in Fig. 3.5, the source was pulsed, with a period of 2.5 sec. The rather "grassy" signal, which has a gross shape similar to the microwave-noise decay, is the diamagnetic signal from a probe on the axis 8 in. from the midplane. The peak-to-peak amplitude on this signal is 5 gauss ± 1 gauss. Notice that the decay times here are on the order of $\frac{1}{4}$ sec. The plasma is believed to be about 4 in. long and about 2 in. in diameter. The energy density required for a plasma of these dimensions to produce a 5-gauss field at the diamagnetic probe is on the order of 10^{17} ev/cm^3. This energy density, along with the measured electron density of 5×10^{12}, implies a "temperature" of well over 10 kev for the plasma electrons.

Some mention should be made of the way in which the density, energy density, temperature, and decay time correlations are made in order to infer a plasma temperature and a plasma density. Expressions due to Spitzer[3] relating the decay time, kinetic temperature, and density in a hot electron gas were plotted in Fig. 3.6. The shaded area indicates the range of these parameters in the high-temperature mode observed in the 14-cm heating experiments. The densities were between 10^{11} and 10^{12} electrons/cm^3, with a mean energy near 10 kev. For the 3-cm heating experiments, the diamagnetic and x-ray measurements in the high-temperature low-density mode implied densities on the order of 10^{11} electrons/cm^3, with the mean energies near 100 kev. Rough agreement for the high-density mode was also found. The measured density of 5×10^{12} electrons/cm^3 and energy density of 1 to 3×10^{17} ev/cm^3 implied an energy near 100 kev and a decay time near 0.2 sec as measured. Diamagnetic probe measurements were made by using a Hall probe on the axis of the machine. The Hall probe was withdrawn, and again the $1/r^3$ dependence was roughly validated, indicating that even at these high energy densities and with much secondary plasma evident in the cavity the high energy density region of the plasma is confined to a rather small volume.

Future plans include the addition of ion cyclotron heating coils inside the cavity. Indications are that the very hot electron gas will facilitate ion heating by retarding the formation of the electric fields caused by charge separation. These fields shield the plasma from the ion heating fields. A neutral Laval beam feed is also under

[3] L. Spitzer, *Physics of Fully Ionized Gases*, pp 76–81, Interscience, New York, 1956.

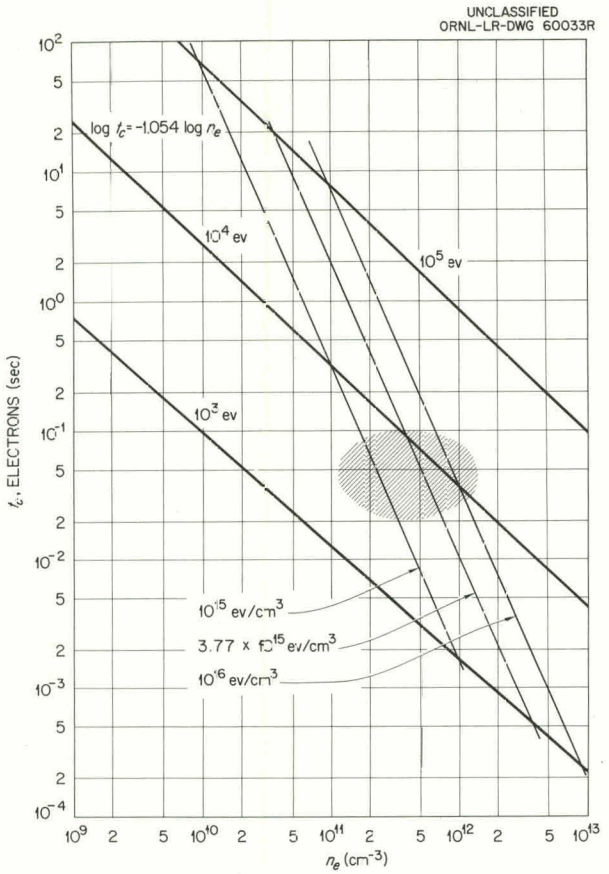

Fig. 3.6. Self-Collision Time as a Function of Energy and Density.

preparation. This kird of directed feed should aid in the elimination of secondary cold plasma which would help to screen the ion cyclotron fields from the hot plasma.

3.1.2 "Elmo"

Future activities include plans for electron heating in a flexible magnetic field configuration. Figure 3.7 is a schematic diagram of the new experimental facility called "Elmo." The current in the two sets of coils can be continuously adjusted for the following field configurations: (1) a field with nearly zero axicl and radial gradients, (2) a mirror field with positive axial gradient and negative radial gradient, and (3) a "folded cusp" field with positive axial ard radial gradients. The third one is the configuration illustrated.

One way of understanding the folded cusp is to consider the inner ard outer coils as two sets of mirror coils in opposition. Figure 3.8 is an iron-filings field plot for the folded cusp in which the current in the two sets of coils is adjusted for zero resultant field at the centers of the configuration. For this case in Elmo the outer coil current is approximately twice the inner coil current and oppositely directed. The folded-line cusps leading diagonally outward from the field center appear clearly. These line cusps, along with the regular point cusps from the single mirror which are also present, will constitute large leaks for particles.

However, it has proved possible to produce high energy densities and large field perturbations with hot-electron-generated plasmas. The energy densities of these plasmas may be limited at present by the negative radial field gradient of the mirror field in which they have been produced. Therefore, an attempt will be made to accumulate plasma in a field with a positive radial gradient. If plasma can be accumulated in spite of the single-particle leaks, advantage may be taken of the inherent stability of the cusp for dense plasma containment.[4]

[4] J. Berkowitz *et al.*, *Proc. U.N. Intern. Conf. Peaceful Uses Atomic Energy, 2d, Geneva, 1958* **31**, 171 (1959).

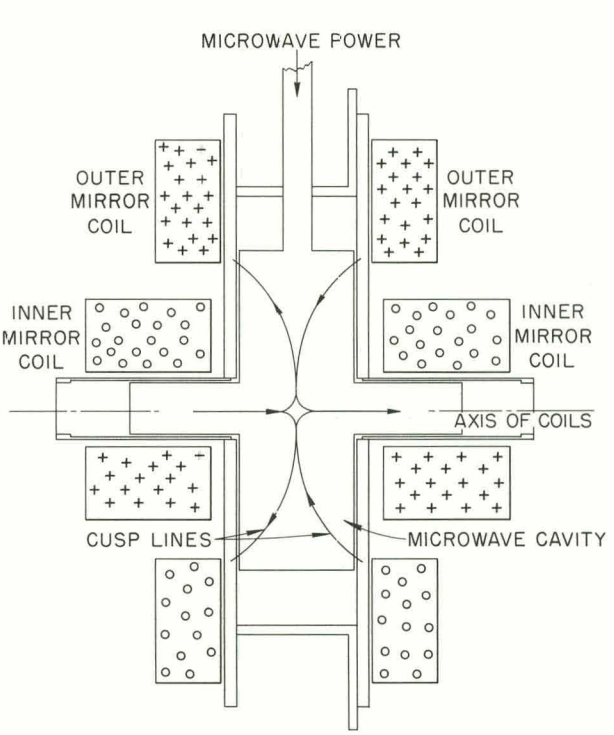

Fig. 3.7. Schematic of "Elmo."

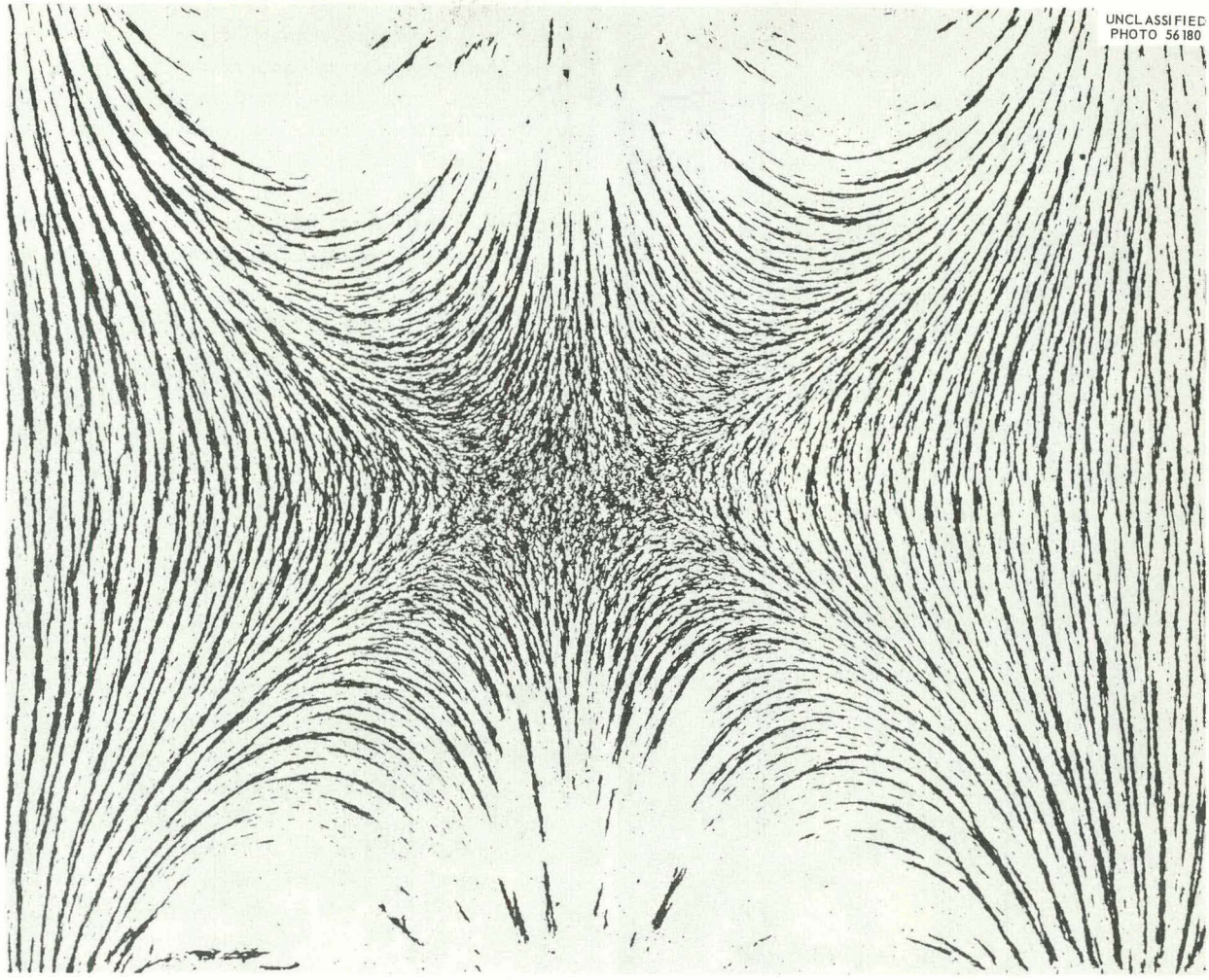

Fig. 3.8. Iron-Filings Plot of Folded Cusp.

Details of the accumulation process, if it exists, are not known. An optimistic approach is to assume that field perturbation produced by the plasma will act to seal up the leaky-cusp magnetic bottle. Electron resonance heating zones for the folded cusp appear in Fig. 3.9.

The new facility is expected to be in operation in December. All of its components except the microwave cavity have been received from the shop. It is now being erected and connected to operational and experimental services. A photograph of Elmo in its present state appears as Fig. 3.10.

Experiments to be performed with Elmo will be similar to those already performed on the Physics Test Facility (PTF), except that the approach will be more careful and fundamental, with an aim at more detailed understanding of the electron heating and containment process. The four parameters, energy, density, volume, and containment time, will naturally furnish the key toward the understanding desired.

The following table lists briefly a few experimental possibilities for measuring these parameters.

Plasma Parameter	Method of Measurement
Electron energy or temperature	X-ray spectrum and microwave noise measurements
Energy density	Hall probe
Density	Neutral beams
Volume and shape	Hall probes, incandescent metal powder, ion beams
Containment time	Decay of microwave noise, x rays, diamagnetic signal

Much of the information obtained on Elmo will be applicable to the PTF experiment, and vice versa.

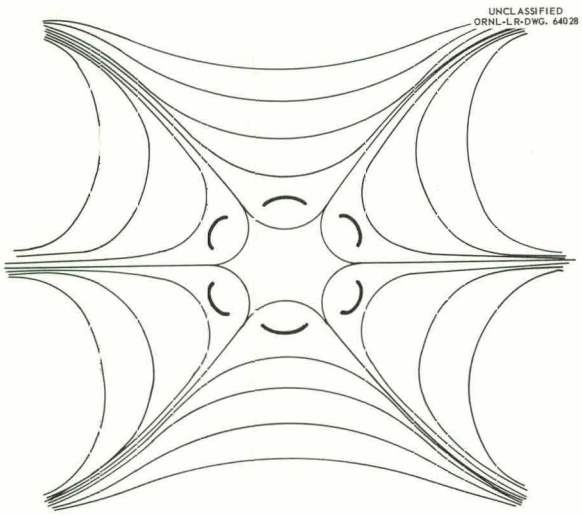

Fig. 3.9. Folded Cusp Heating Zones.

3.1.3 Neutral-Beam-Transmission Experiment

The source for the neutral molecular hydrogen beam used to measure plasma densities was of the "oven" type.[5] Figure 3.11 shows the gas bottle, source, and beam-defining collimators. Hydrogen gas is held in the bottle at room temperature and at a pressure of 75 μ Hg. It emerges through a 1×10 mm slit. Since the slit width is less than the normal mean free path for molecular collisions, the gas molecules travel approximately in straight lines. The collimators then define a "beam," provided that all particles they interrupt are promptly disposed of by differential pumping.

The particle current I_0 derivable from such a source is fixed by the gas scattering probability and by the allowable beam divergence. It is given by the expression

$$I_0 = \frac{nvA}{4},$$

where n is the molecular density, and v is the molecular velocity. The source slit area, A, is $L\lambda$, in which L = slit length, and λ = mean free path. Now $\lambda \propto 1/n$, and therefore $I_0 \propto vL/4$. The flux, I_0, is not a function of n because an increase in source pressure necessitates a corresponding decrease in slit width. The slit length, L, is fixed by the allowable beam cross section.

The source output is then the flux I_0 reduced by the solid angle at the final collimator. In this case, as shown in Fig. 3.11, the final collimator is the input tube of the ion gage. The calculated beam intensity is $\sim 10^{13}$ particles/sec, using λ calculated for large-angle scattering. The measured intensity is 10 times less because of the shorter λ for small-angle scattering events.[6]

The experimental arrangement of beam source and detector on the PTF appears also in Fig. 3.11. That portion of the beam which penetrates the plasma in the microwave cavity and enters the "beam catcher" ion gage is measured as a pressure increase in the gage chamber.

The differential pressure ΔP arising from the beam is obtained from the beam-catcher gage reading $(P + \Delta P)$ by subtracting the ambient pressure P, and an "ambient" pressure gage mounted perpendicular to the beam is enclosed in the detection chamber. Current from the two ion gages is fed into a differential amplifier (Fig. 3.12). Output of this is a signal proportional to ΔP, of proper voltage for driving a chart recorder. Under operating conditions $\Delta P/P$ is $\sim 1/100$. Therefore, the gage currents and differential amplifiers must be stable to about one part in 10^4 to permit measurement of

[5] Ronald Fraser, *Molecular Beams*, Methuen, London, 1936.

[6] H. S. W. Massey and E. H. S. Burhop, *Electronic and Ionic Impact Phenomena*, p 320, Oxford Press, London, 1952.

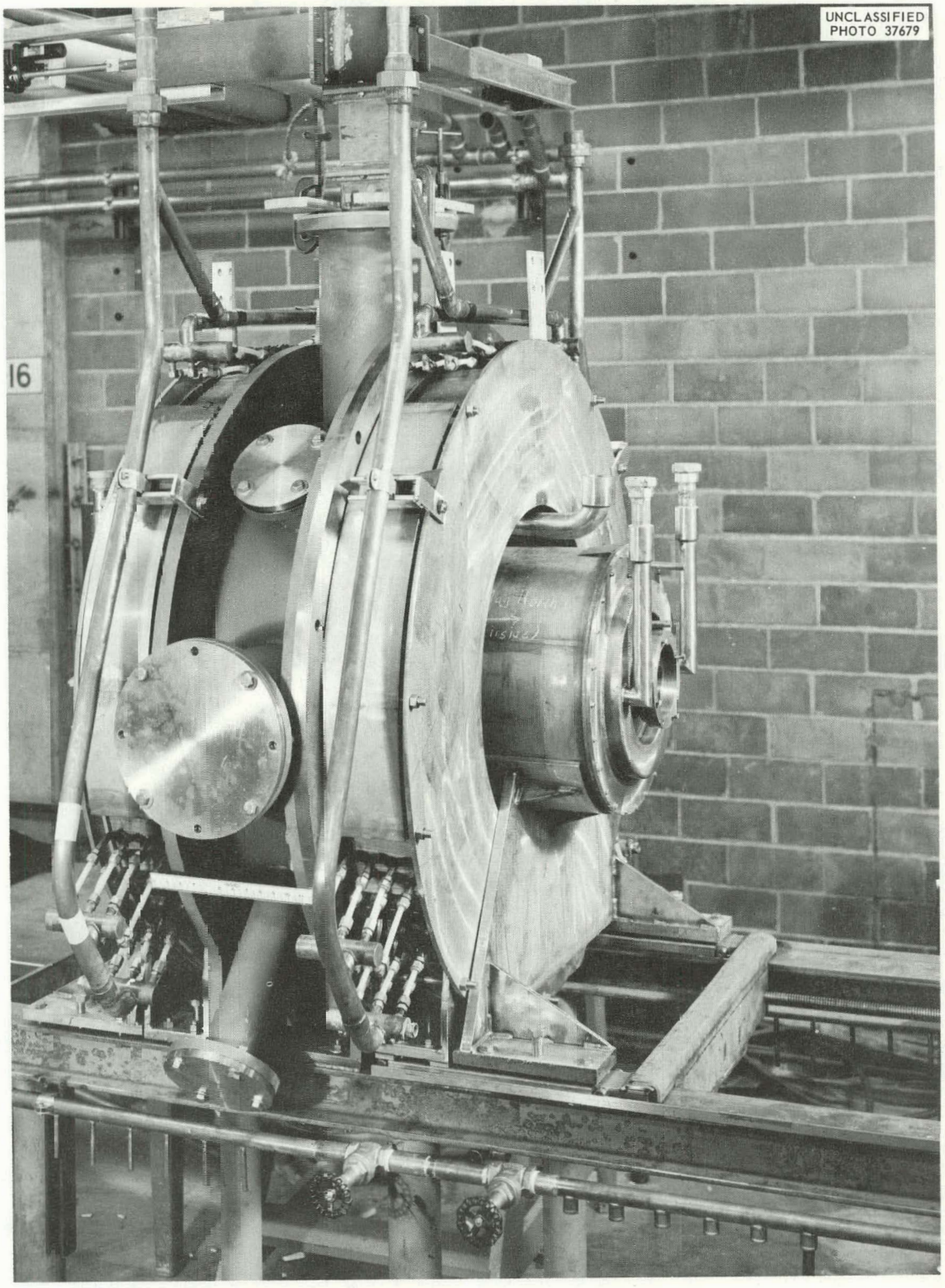

Fig. 3.10. Photo of "Elmo."

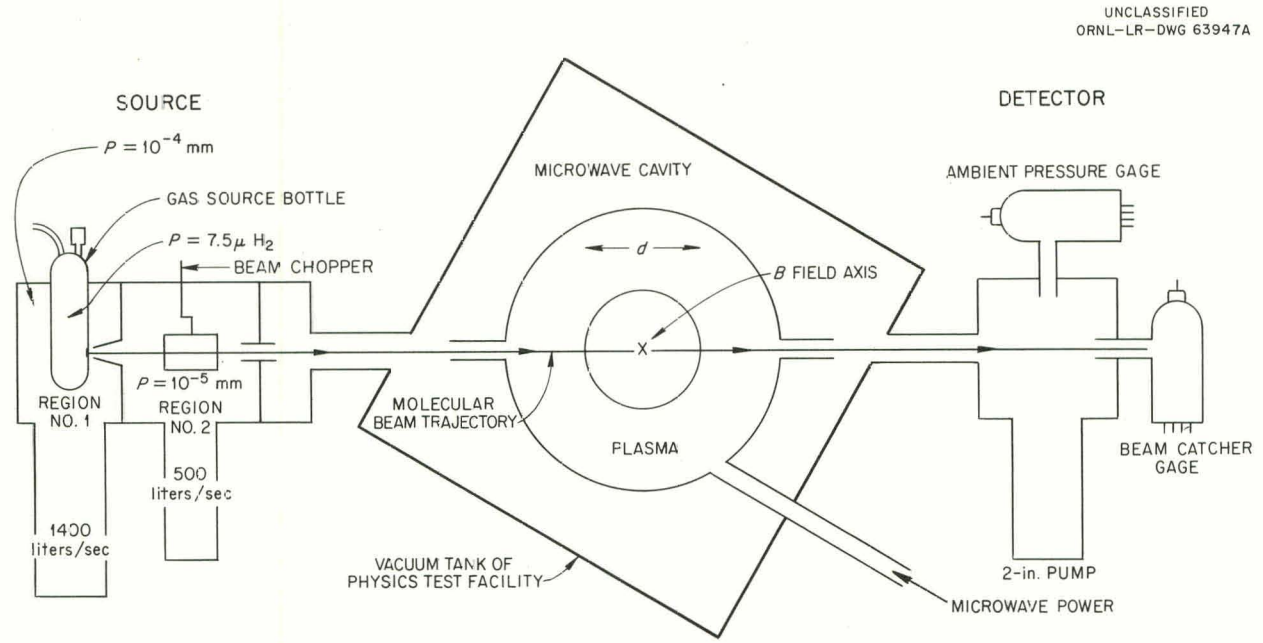

Fig. 3.11. Molecular-Beam Assembly on the Physics Test Facility.

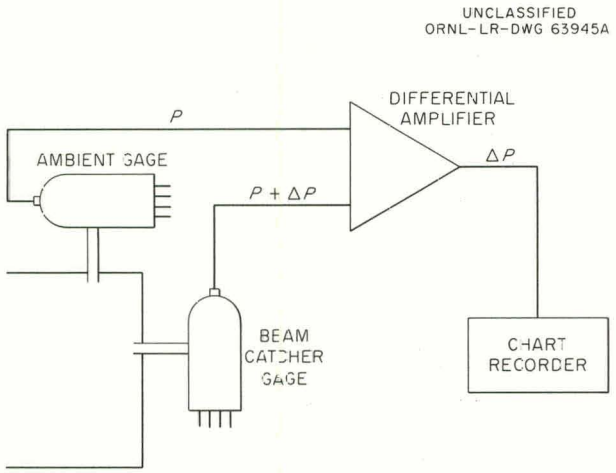

Fig. 3.12. Differential-Pressure Measuring Circuit.

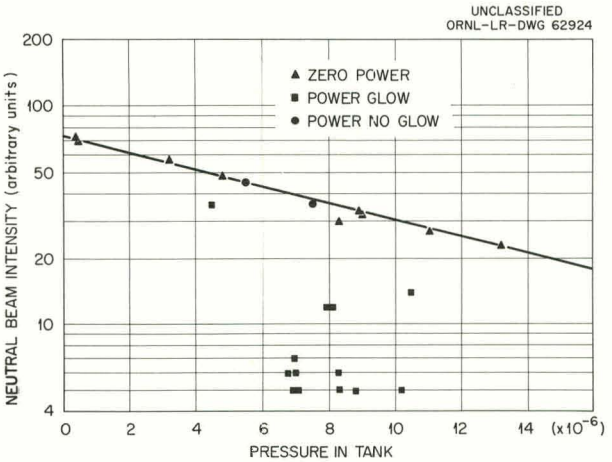

Fig. 3.13. Neutral-Beam Transmission as a Function of Pressure.

ΔP to within a few per cent. The beam is chopped mechanically every 10 sec as a check on stability.

The results of initicl measurements on the hot-electron plasma appear in Fig. 3.13. The beam is attenuated by elastic scattering in the background hydrogen gas, but this is a logarithmic function of pressure. Therefore, the resultant intensity appears conveniently as a straight line in the semi-logarithmic plot. Attenuation of the beam by the plasma may then be calculated as the ratio of transmitted beam intensity with plasma to intensity with no plasma at the corresponding pressure.

Figure 3.14 illustrates the beam attenuation as microwave power is increased. The logarithmic character of this curve indicates a linear dependence of plasma density on input power, as the following will make clear. The formula for beam attenuation is $I = I_0\, e^{-D/\lambda}$, where I_0 = incident

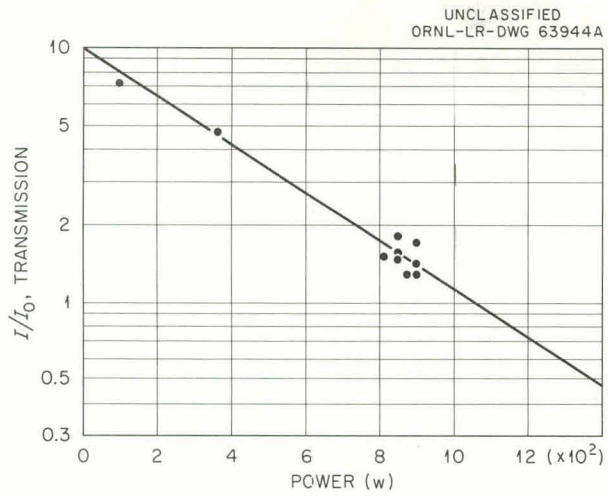

Fig. 3.14. Neutral-Beam Transmission as a Function of Microwave Power.

intensity, D = plasma diameter. For ionization by hot electrons,

$$\lambda = \frac{v}{n_e v_e \sigma} ,$$

in which

n_e = electron density per cubic centimeter,

σ = ionization cross section of plasma electrons,

v_e = velocity of plasma electrons,

v = velocity of neutral molecules.

Combining the above two equations gives

$$\log\left(\frac{I}{I_0}\right) = -\frac{Dnv_e\sigma}{v} .$$

We assume that v_e and v are slow functions of power in the glow mode. The product Dn must then depend linearly upon microwave power. But D is believed to be relatively constant; therefore n must increase linearly with power.

At maximum attenuation the average plasma density is calculated as $5 \times 10^{12}/\text{cm}^3$, making use of the previously measured D and v_e (see previous section). The determination is not too sensitive to electron energy. For example, the ionization rate σv_e varies approximately as $v^{-1/2}$ in this region. The value of D assumed may be in error by ±50%, and this is probably the greatest uncertainty in the measurement. Charge exchange with cold plasma ions can attenuate the beam an amount depending on ion energy. In the worst possible case this is a 30% correction and has already been made.[7]

The actual beam transmitted could be measured to within ±20%. The accuracy was limited by drift in the emission regulator for the ion-gage filaments. A transistorized gage-current regulator and differential amplifier have been designed to eliminate this difficulty. Figures 3.15 and 3.16 show the circuit diagram and photograph of this instrument. Differential drift of the ion-gage emission currents has been reduced to 1 part in 10^3 for 1 hr and to less than 1 part in 10^{-5} for 10 sec. Present sensitivity of this gage is $\leq 10^{-10}$ mm of differential pressure with the beam chopped every 10 sec. The common mode rejection is 500 to 1. Response time of the complete thermal neutral beam detector is ~30 msec and is determined by the gas conductance of the gage input tubes. The length of these gage tubes is a compromise between response time and sensitivity, a longer tube producing a higher pressure reading and longer response time.

The advantages of this detector over the Pirani gage lie in its greater sensivity and faster response time. Response times are a few milliseconds, compared with minutes for the Pirani.

The beam source and detector system should be a useful tool for density measurements of ionizing plasmas. It combines high sensitivity with ease of interpretation and minimum disturbance to the plasma. For example, in this experiment the neutral-beam feed was less than 10^{-5} of the cold plasma drift through the mirrors.

---

[7] J. B. Hasted, *Proc. Roy. Soc. (London)* **A227**, 476 (1954).

UNCLASSIFIED
ORNL-LR-DWG 63914

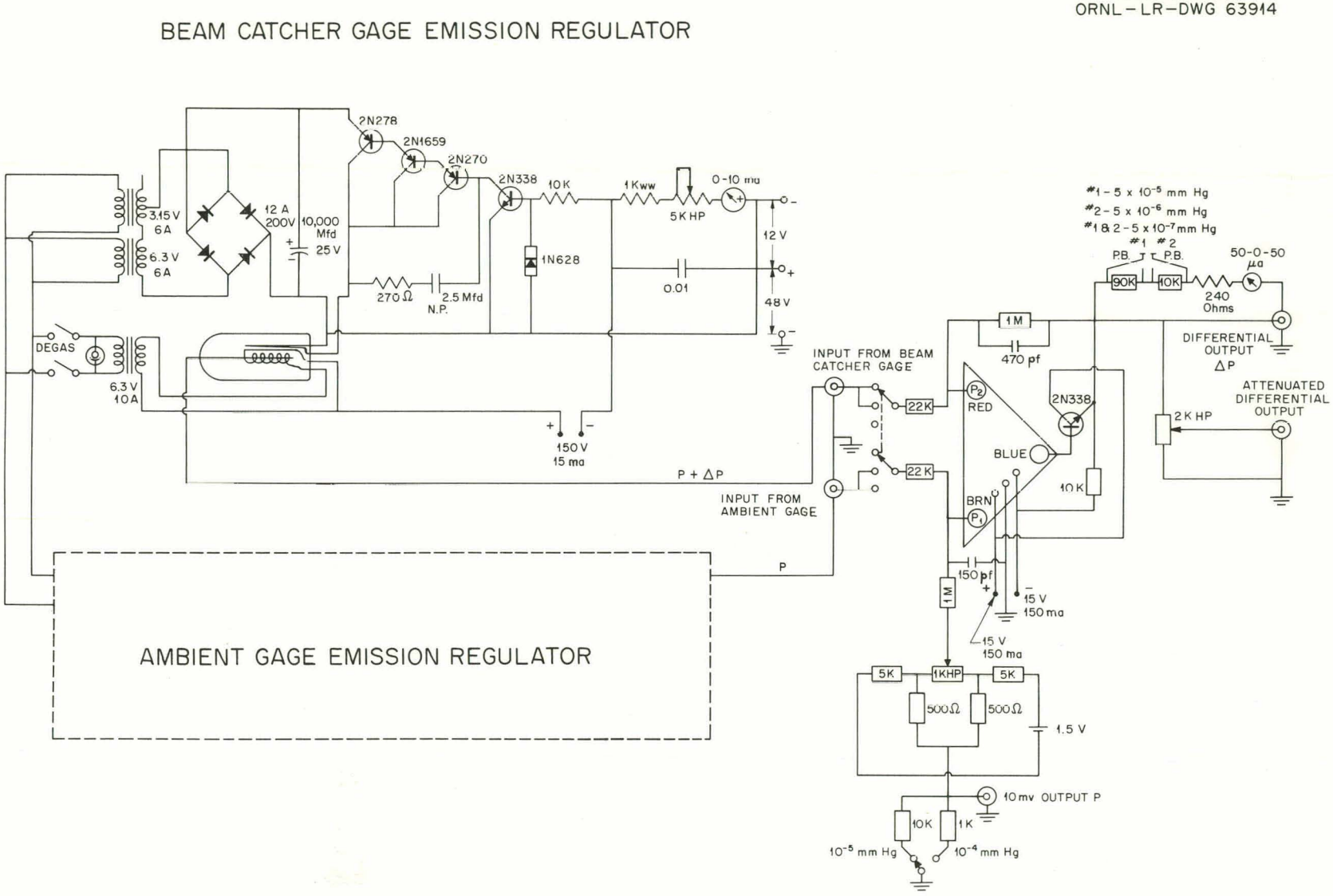

Fig. 3.15. Circuit Diagram of Ionization Gage Emission Current Regulator and Differential Amplifier.

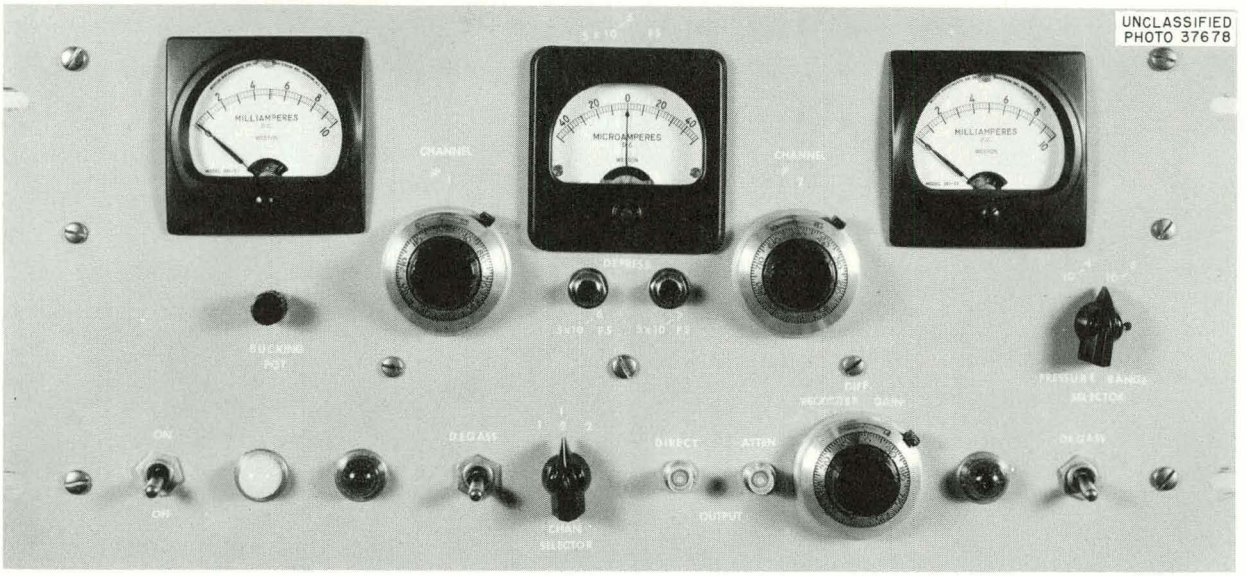

Fig. 3.16. Photograph of Ionization Gage Emission Current Regulator and Differential Amplifier.

3.2 IONIC SOUND WAVES

I. Alexeff R. V. Neidigh

3.2.1 Introduction

The study of ionic sound waves in plasmas is of importance to the thermonuclear program. Ionic sound waves may trigger or enhance an instability. When properly understood they may be used as a diagnostic tool. They may also provide a convenient mechanism for feeding energy into or extracting energy from a plasma.

In the last semiannual report,[8] observations apparently showed the existence of ionic sound waves. They were found in both the mode I and mode II magnetically supported vacuum arcs. The possibility that ionic sound waves might be the mechanism that drives the mode II blowup phenomena was suggested. In addition, data obtained by F. W. Crawford[9] on the rf noise spectrum emitted by cylindrical mercury-vapor discharge tubes were interpreted in terms of ionic sound waves.

This report contains subsequent experiments which support the original hypothesis of ionic sound waves. They are more completely investigated in mode I arcs. Resonance effects are observed between the ionic sound-wave frequency and the ion cyclotron frequency. An addition and correction to a recent work of F. W. Crawford[10] are discussed. Ionic sound waves are shown to occur in a three-dimensional system in a spherical discharge tube in the absence of a magnetic field. The Z-wise pressure exerted by a magnetically confined plasma may readily be measured and used to determine the electron temperature or density.

3.2.2 Ionic Sound Waves in Mode I Arcs

In the previous semiannual report (ORNL-3104, pp 31–40), the frequency f of an ionic sound wave in a plasma generated by the apparatus shown in Fig. 3.17 was shown to be related to the plasma column length L, the electron temperature T_e, and the ion mass m_i by:

$$f = \frac{1}{2L}\left(\frac{\gamma k T_e}{m_i}\right)^{1/2},$$

where k is Boltzmann's constant, and γ, the adiabatic compression coefficient, is assumed to be

[8] I. Alexeff and R. V. Neidigh, *Thermonuclear Div. Semiann. Rept. Jan. 31, 1961*, ORNL-3104, pp 31–45; *Bull. Am. Phys. Soc.* **6**, 309 (1961); *Phys. Rev. Letters* **7**, 223 (1961).

[9] F. W. Crawford, *Frequency Spectra of Low Frequency Fluctuations in a Plasma*, W. W. Hansen Laboratories of Physics, Stanford Univ. Microwave Laboratory, ML-762 (November 1960).

[10] F. W. Crawford, *Phys. Rev. Letters* **6**, 663 (1961).

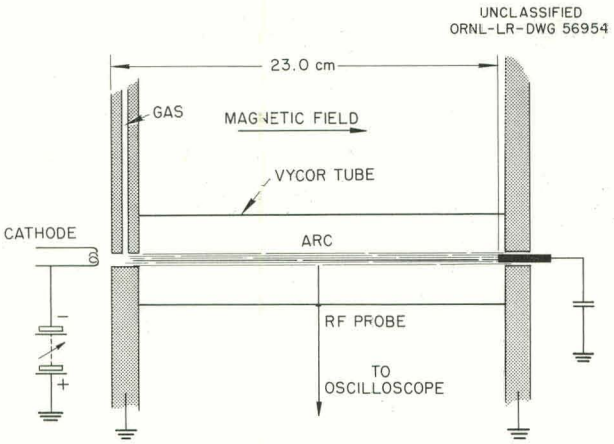

Fig. 3.17. Apparatus Used for Mode I Arc RF Studies.

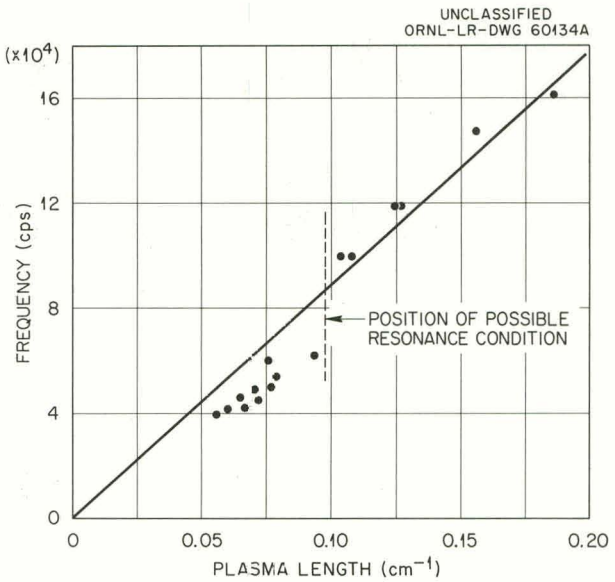

Fig. 3.18. Frequency Dependence on Length of Plasma Column in a Mode I Argon Arc.

equal to 3. The fundamental frequency of the standing waves formed was measured for two lengths of arc.

The frequency dependence on the length of the oscillating column of plasma has since been verified by an additional experiment. The apparatus, shown in Fig. 3.17, was modified, so that the length of the plasma column could be varied continuously while operating.

The dependence of frequency on column length for an argon plasma is shown in Fig. 3.18. The observed frequency is plotted against the reciprocal of the plasma column length. In general, the frequency appears to depend linearly on the reciprocal length of the plasma column. A discontinuity in the experimental points is observed where the ionic-sound-wave frequency equals the ion cyclotron frequency. An energy transfer to the secondary plasma was indicated at this point by an increase in the secondary plasma potential. A corresponding decrease in electron temperature in the arc is indicated by a sudden drop in the ionic-sound-wave frequency.

In the previous report the plasma electron temperatures were not measured. The temperature used to calculate the frequency of a standing ionic sound wave was 17 ev. The temperature of 17 ev is an average of the lowest excitation potentials of the un-ionized noble gases which were studied.

Measurements of the electron temperature have since been made in various columns of plasma by a Langmuir probe, by measurements of the plasma electron pressure, and, in the case of helium, by measuring the singlet-triplet intensity ratio for the spectral lines 4921 and 4713 A. In general, the first two methods show a nonsystematic scatter of about a factor of 2. However, on the average, the value for the electron temperature of a plasma yielded by these methods agrees with that obtained from the frequency of the ionic sound wave in the plasma. The spectroscopic method gave values that were systematically high. However, the spectroscopic method also gave anomalously high electron temperatures in control experiments with helium discharge tubes.

Temperatures measured by these methods are recorded in Table 3.1. Only measurements that were made during the same run are compared. The results are as good as can be expected in view of the present preliminary state of the art.

3.2.3 Ionic Sound Waves in Cylindrical Discharge Tubes

According to our interpretation of the data obtained by Crawford, there was evidence of ionic sound waves, and this was reported previously (ORNL-3104, pp 40–45). Recently, Crawford obtained more data[11] and interpreted them in terms of ionic sound waves.

[11] F. W. Crawford, *Phys. Rev. Letters* **6**, 663 (1961).

Table 3.1. Plasma Electron Temperatures (in Electron Volts) by Various Methods

Gas	Method				
	Ionic Sound Wave	Singlet / Triplet	Langmuir Probe	Plasma Pressure	Lowest Excitation Potential
Helium (9 runs)	21	58			20
Deuterium (1 run)	22		42	22	10
Argon (3 runs)	41		34	25	12

Although Crawford finds the frequencies corresponding to the radial modes in a cylindrical discharge that were predicted at ORNL, he finds an extra frequency. This frequency does not fit into his theoretical picture, and is interpreted by him as a second harmonic, caused by nonlinearities in the system.

A more possible reason for the extra frequency found by Crawford is that it corresponds to a quadrature mode that was accidentally omitted in the original ORNL report. Crawford makes the identical oversight that was made at ORNL. The original data, Crawford's new data, and the nodal lines for the various modes of oscillation are summarized in Fig. 3.19 and Tables 3.2 and 3.3.

In addition to the low-frequency modes of oscillation in Crawford's discharge tubes, the original ORNL report also interpreted the high-frequency cutoff that Crawford found in his noise spectrum. This high-frequency cutoff was interpreted as due to the fact that ionic sound waves occur in a discharge tube only for frequencies below the ion plasma frequency,

$$\left(\frac{Ne^2}{\pi m_i}\right)^{1/2} = f_c.$$

Here N is the number of ions/cm^3 in the plasma, e is the charge of an electron, m_i is the ion mass, and f_c is the ion plasma, or cutoff, frequency.

Further studies of the high-frequency cutoff in the noise spectrum of discharge tubes were attempted at ORNL because the cutoff frequency

Table 3.2. Correction to Previous Report

Previous ORNL Predicted Frequencies (cps)	Crawford's Observed Frequencies (cps)	Predicted ORNL Frequencies Corrected (cps)
$\times$ $^{\cdot}0^4$	$\times$ 10^4	$\times$ 10^4
7.0	7.0	7.0
11.2	11.5	11.2
16.1	14.5	14.9

UNCLASSIFIED
ORNL-LR-DWG 64321

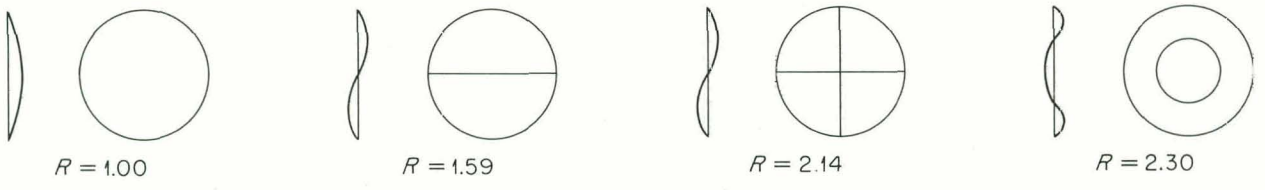

Fig. 3.19. Nodal Lines for the Four Lowest Radial Modes in an Oscillating Cylinder with a Pressure Node at the Wall. R is the ratio of the frequency of a given mode to the frequency of the fundamental mode.

Table 3.3. Correction to Crawford's Work[a]

The numbers refer to the ratio of the frequency of a given peak in the noise spectrum to the frequency of the lowest observed peak

Crawford's Observed Ratios	Crawford's Identification	Probable Identification by ORNL	Predicted Ratios by ORNL
1.00	Fundamental mode	Fundamental mode	1.00
1.68	Overtone	1st overtone	1.59
2.00	Result of nonlinearity in system	2d overtone	2.14
2.34	Overtone	3d overtone	2.30

[a]F. W. Crawford, *Phys. Rev. Letters* 6, 663 (1961).

might be used as a measure of N. Although results were suggestive, good data could not be obtained. The exact location of the high-frequency cutoff was generally obscured by the high electrical noise level at the laboratory site.

3.2.4 Ionic Sound Waves in Spherical Discharge Tubes[12]

I. Alexeff R. V. Neidigh

Introduction. – Previous work at Oak Ridge National Laboratory[13] appeared to demonstrate the existence of ionic sound waves in a magnetically supported column of plasma. This paper discusses similar standing ionic sound waves generated in glass spheres without any supporting magnetic field.[14] This work can be considered as an extension of the work of Revans,[15] who used mercury vapor in a sphere.

This paper first discusses general properties of ionic sound waves. Conditions are presented under which standing ionic sound waves may occur in spheres. Experimental results apparently confirming the predictions of the theory are presented. The paper concludes with a summary and an application.

General Properties of Ionic Sound Waves. – The existence of ionic sound waves was predicted in 1929 by Tonks and Langmuir.[16] For wavelengths long compared with the Debye shielding distance, the frequency of an ionic sound wave is given by the formula:

$$F = \frac{1}{\lambda}\left(\frac{\gamma k T_e}{m_i}\right)^{1/2},$$

where

F = frequency in cycles per second,
λ = wavelength in centimeters,
γ = adiabatic compression coefficient,
k = Boltzmann's constant in ergs per °K,
T_e = electron temperature in °K,
m_i = ion mass in grams.

The constant γ, referring to the adiabatic compression of the electron gas, was set equal to 1 in the paper of Tonks and Langmuir. This value corresponds to an isothermal ionic sound wave. If the electrons suffer scatterings but no energy losses during one cycle of the ionic sound wave, then γ is 5/3. This corresponds to the case of a conventional sound wave. Spitzer[17] shows that in a sufficiently rarefied plasma, γ may be 3.

[12]This paper was presented at the Fifth International Conference on Ionization Phenomena in Gases, Munich, Germany, August 1961.

[13]Igor Alexeff and Rodger Neidigh, *Bull. Am. Phys. Soc.* 6, 309 (1961); *Apparent Observations of Ionic Sound Waves in an Arc Plasma*, ORNL CF-61-2-57 (Feb. 13, 1961); *Thermonuclear Div. Semiann. Rept. Jan. 31, 1961*, ORNL-3104, pp 31–40.

[14]Igor Alexeff and Rodger Neidigh, *Observation of Ionic Sound Waves in Gaseous Discharge Tubes*, ORNL CF-61-6-66 (June 7, 1961).

[15]R. W. Revans, *Phys. Rev.* 44, 798 (1933).

[16]L. Tonks and I. Langmuir, *Phys. Rev.* 33, 195 (1929).

[17]L. Spitzer, Jr., *Physics of Fully Ionized Gases*, p 59, Interscience, New York, 1956.

Standing Ionic Sound Waves in a Sphere. – A spherical discharge tube was chosen in preference to a cylinder because the lowest mode of oscillation in a sphere may be less damped. In a sphere, the lowest mode involves no transport of matter parallel to the wall and therefore perhaps less damping due to friction.

In a spherical resonator, the wavelength λ must correspond to some dimension in the apparatus. For a plasma in a sphere, there are several possibilities. If the boundary of the plasma is a pressure antinode, $\lambda = 1.51\ D$, where D is the diameter of the sphere. This boundary condition corresponds to an ordinary sound wave in a gas. For the plasma, however, it is not determined that this boundary condition is correct. The plasma boundary could be a pressure node. In this case, $\lambda = 1.00\ D$. The fundamental frequency in the sphere is thus given by the formula:

$$F = \frac{1}{CD}\left(\frac{\gamma k T_e}{m_i}\right)^{1/2},$$

where D is the sphere diameter, and C is a constant that can be 1.51 or 1.00, depending on the plasma boundary conditions.

Higher-frequency modes of oscillation should occur in the sphere. These higher-frequency modes should have frequencies which are not integral multiples of the fundamental. If a pressure antinode at the boundary occurs, the next six higher frequencies will be 1.61, 2.16, 2.17, 2.71, 2.85, and 3.25 times the fundamental, respectively. If a pressure node at the boundary occurs, the ratios are 1.43, 1.84, 2.00, 2.22, 2.46, and 2.60, respectively.[18]

Predictions concerning the oscillation of the plasma in a spherical discharge tube can now be made. If the discussion is correct, the following regularities should be observed.

1. The wave form is sinusoidal.
2. Higher-frequency modes of oscillation can appear. The frequencies are not integral multiples of the fundamental. The second higher frequency is approximately 1.5 times the fundamental.
3. The frequency is proportional to $m_i^{-1/2}$.
4. The frequency is proportional to D^{-1}.
5. The frequency gives a value for the electron temperature T_e which agrees with those values obtained by other methods.

Experimental Results. – *Design of Apparatus.* – The discharge tube used is shown in Fig. 3.20. The tube was made of glass for the following reasons: first, ease of fabrication; second, transparency; third, no lead-in insulators are required. On one side of the sphere, a heated tungsten filament was used as a cathode. The anode was a flat disk opposite the cathode. Both electrodes were mounted flush with the wall.

The electron temperature at the center of the sphere was measured by a Langmuir probe. The probe was insulated except for its tip. To make the sphere a good resonator, the volume was kept as free as possible of obstructions and irregularities. The oscillations were detected by a capacitively coupled electrode attached to the outside of the glass sphere.

Oscillations were obtained at pressures in the vicinity of 20 μ. The discharge voltage was between 20 and 100 v. The discharge current was between a few milliamperes and a few amperes. Varying the discharge voltage, current, and pressure caused the oscillation to increase or decrease in amplitude and to become more or less free of noise. However, the frequency could not be changed continuously.

Verification of Theoretical Predictions. – 1. Sinusoidal Wave Form. Under optimum conditions, a fairly sinusoidal oscillation was obtained, as shown in Fig. 3.21. The maximum voltage observed was about 1.0 v rms. Thus prediction No. 1 appears to be verified. The wave form is sinusoidal.

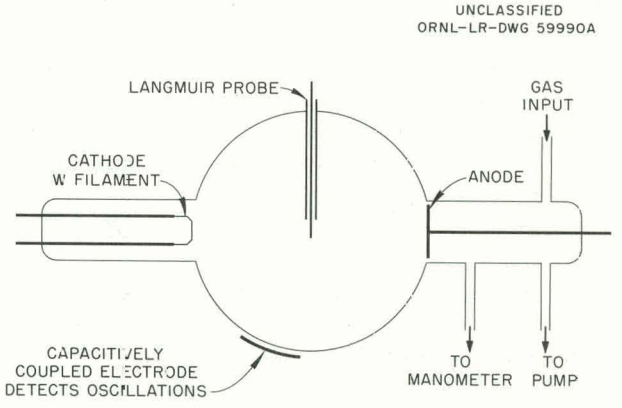

Fig. 3.20. Construction of Discharge Tube.

[18] J. W. S. Rayleigh, *The Theory of Sound*, sec 331, 332, Dover, New York, 1956.

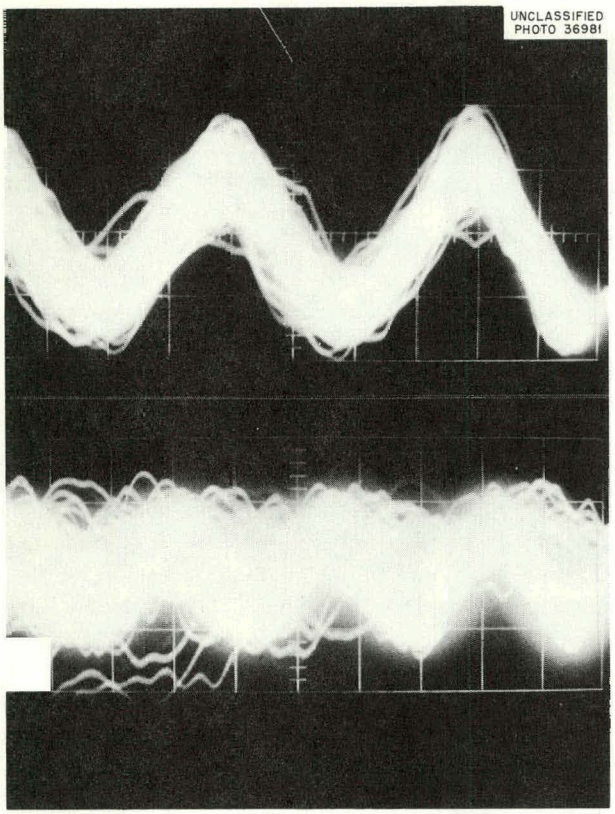

Fig. 3.21. Fundamental and Second Higher Frequency Oscillation in Helium. (1.0 μsec/square division, 0.5 v/square division, tube 10 cm in diameter.)

2. Higher-Frequency Modes of Oscillation. Next, harmonics were studied. At unpredictable values of discharge-tube voltage or current, the frequency would jump discontinuously to higher or lower values. At times, frequency changes were observed which corresponded closely to a series of overtones in a sphere. One measurement with xenon gave the ratios 1.00, 1.57, and 2.63. These ratios may correspond to the fundamental, first, and third overtone, if a pressure antinode occurs at the discharge-tube wall. In general, attempts to identify correctly the higher overtones proved to be quite difficult, and these overtones were not studied extensively.

In general, the second higher frequency that was observed appeared to be 1.5 times the fundamental frequency. Oscillations in a helium plasma are shown in the two multiple-sweep oscillograms in Fig. 3.21. One trace shows the lowest observed frequency, which may be the fundamental; the other is the second higher observed frequency. The two frequencies are related in the ratio of 1.43 to 1.

Thus prediction No. 2 seems to be verified. Higher frequency modes of oscillation can occur.

3. Frequency Proportional to $m_i^{-1/2}$. Next, the fundamental frequency as a function of ion mass was studied. The ion mass used varied from atomic mass 1 (hydrogen) to atomic mass 131 (xenon). Spheres 2.5, 10, and 25 cm in diameter were used. During each run, the electron temperature T_e was measured with the Langmuir probe. An observed frequency was then normalized to the value corresponding to T_e = 1 ev. The normalized frequency is given by the formula:

$$F_{\text{normalized}} = (T_e)^{-1/2} F_{\text{observed}}.$$

The values of $F_{\text{normalized}}$ should not show the effects of the electron-temperature variation from gas to gas. The results for one run in the sphere 10 cm in diameter are shown in Fig. 3.22. The values of $F_{\text{normalized}}$ are plotted against m_i on a log-log graph. If the above discussion is correct, the points should lie along a line of slope −1/2. The experimental points seem to fit this slope. In general, prediction No. 3 seems to be verified. The frequency is proportional to $m_i^{-1/2}$.

4. Frequency Proportional to D^{-1}. Next, the fundamental frequency as a function of sphere diameter was studied. Spheres 2.5, 10, and 25 cm in diameter were used. Some experimental results are shown in Fig. 3.23. The value of

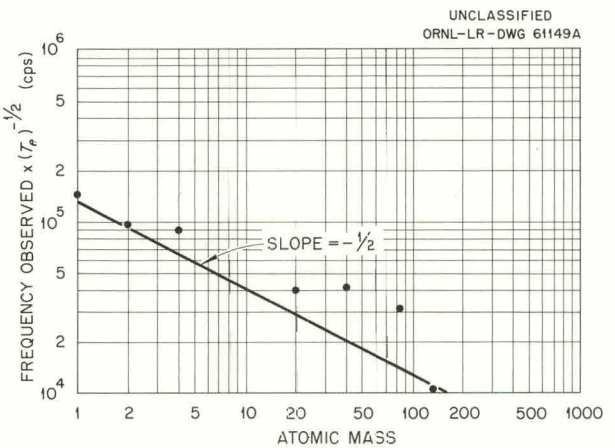

Fig. 3.22. Frequency as a Function of Atomic Mass. (A sphere 10 cm in diameter was used.)

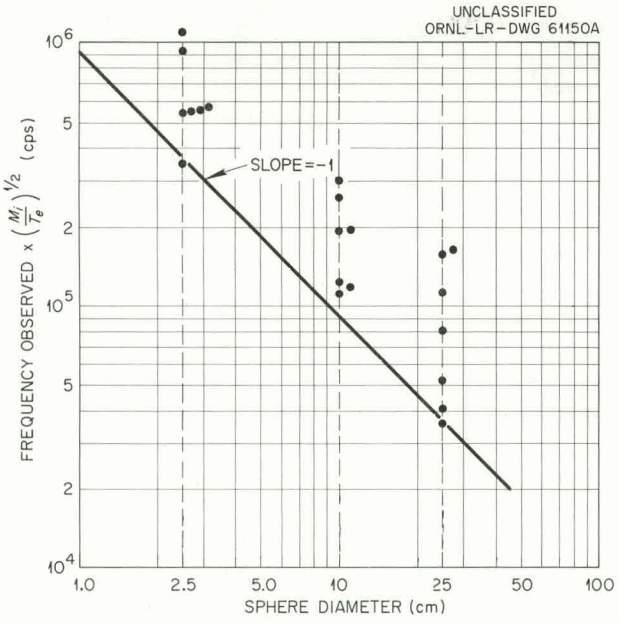

Fig. 3.23. Frequency as a Function of Sphere Diameter.

each observed frequency here is multiplied by $(m_i/T_e)^{1/2}$ so that only the frequency dependence on sphere diameter should be present. The points are plotted on a log-log graph. If the discussion is correct, the points should lie on a line of slope −1. Although the points show much scatter, they appear to follow a line of the correct slope. Thus prediction No. 4 seems to be verified. The frequency is proportional to D^{-1}.

5. Frequency Gives the Correct Electron Temperature T_e. Next, the electron temperatures T_e, as found from the oscillations, are compared with those found by use of a Langmuir probe. The values of T_e from the oscillations are, on the average, about 2 times higher than those from the Langmuir probe. This result assumes that $\gamma = 3$ and that the plasma boundary is a pressure node. Any other choice of γ and of the boundary condition makes the oscillation values of T_e higher and the disagreement greater. However, prediction No. 5 seems to be roughly verified. The frequency gives the correct order of magnitude of the electron temperature, T_e.

Additional Observations. – 1. Possible Problem of Overtones. One possible cause of the oscillation values of T_e being higher than the Langmuir probe values is the accidental use of the frequencies corresponding to overtones. In some cases, apparently, the lowest mode of oscillation of the sphere was not observed. Experience with the discharge tubes showed that often the higher frequency modes were more easily excited. The vertical spread of the points in Fig. 3.23 also suggests the presence of overtones.

There are two possible reasons why overtones might be preferentially excited in the spherical discharge tubes. First, any asymmetry in the discharge tube would tend to excite asymmetric modes of oscillation. These asymmetric modes produce overtones. Second, calculations indicate that the lower frequency modes of oscillation are damped by the high gas pressure in the discharge tube. This high gas pressure is required to maintain the discharge.

2. Observation of Ordinary Sound Waves. At still higher pressures in the discharge tube – at about 1000 μ – oscillations lower in frequency than those expected from the fundamental appear. These oscillations apparently do not correspond to plasma oscillations but to ordinary sound waves in the residual gas.

3. Possible Values for γ and for C. The proper values for the adiabatic compression coefficient γ and the boundary-condition constant C are next considered. First, the frequency observed for each run is reduced to the frequency that would be expected for a hydrogen plasma at a temperature of 1 ev in a sphere 10 cm in diameter. The formula for the reduced frequency is given below:

$$f_{\text{reduced}} = f_{\text{observed}} \left(\frac{m_i}{T_e}\right)^{1/2} \frac{D}{10} .$$

If in all cases the sphere were oscillating at the fundamental frequency, and if the values of γ and C were constant, then all the values of f_{reduced} would be equal.

The values of f_{reduced} are plotted in Fig. 3.24. There is a considerable spread in the frequencies, showing that possibly harmonics are present and that possibly γ and C vary. The expected values for the fundamental frequency for $\gamma = 1$, 5/3, and 3, and for $C = 1.00$ and 1.51, are plotted for comparison. The value of $\gamma = 3$ is improbable, because of electron scattering from the background gas atoms. Values of γ intermediate to those

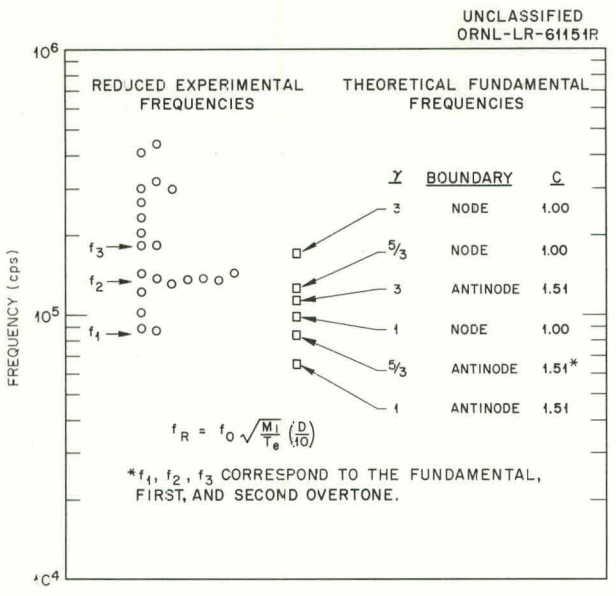

Fig. 3.24. Reduced Experimental Frequencies and Theoretical Fundamental Frequencies.

given can occur, but they are less probable, as the oscillations are strongly damped.[19]

The lowest values of $f_{reduced}$ may correspond to the fundamental frequency in the spheres. In this case, the best fitting theoretical point is that for $\gamma = 5/3$ and $C = 1.51$ (pressure antinode at boundary). The plasma is therefore behaving as an ordinary gas in a spherical resonator. A large number of the observed values of $f_{reduced}$ now correspond to the first overtone in a sphere, as shown in Fig. 3.24. The remaining values of $f_{reduced}$ can correspond to still higher overtones. Thus the values of $\gamma = 5/3$ and $C = 1.51$ appear to fit the data fairly well. However, it is possible that in some of the runs, different values of these constants occur.

Summary. – Apparently, plasma ionic sound waves have been successfully observed in a spherical discharge tube. Sinusoidal oscillations can be obtained. Higher-frequency modes of oscillation that have nonintegral frequency ratios are predicted. These modes occurred. The predicted dependence of the frequency on ion mass and on discharge-tube diameter is apparently verified. Finally, with the proper choice of discharge parameters, the electron temperatures found from the ionic-sound-wave formula agree fairly well with the values found by a Langmuir probe.

In general, our observations agree well with those of Revans.[15] Revans separately excited the fundamental, first, and second overtone in a spherical discharge tube filled with mercury vapor. Some added evidence for ionic sound waves was found by one of the authors,[20] and by Moore[21] in the work of Crawford.[22] Crawford measured the rf noise spectrum of various cylindrical discharge tubes filled with mercury vapor. He obtains peaks in the spectrum and shows that these peaks correspond to the predicted frequencies of various radial modes of oscillation.[23,24]

Many oscillations found in plasmas may be due to standing ionic sound waves. The analysis of these waves might be useful in determining the temperature of the electrons in a plasma.

3.2.5 Observation of Plasma Pressure

The existence of ionic sound waves implies the existence of a plasma pressure. The formula for the velocity of an ionic sound wave can be put into such a form as to exhibit a pressure term. The velocity v is given below, under well-known conditions of approximation,

$$v = \left(\frac{\gamma k T_e}{m_i}\right)^{1/2} .$$

Here γ is the adiabatic compression coefficient of the electron gas, k is Boltzmann's constant, T_e is the electron temperature, and m_i is the ion mass. Let both the numerator and denominator inside the parentheses be multiplied by the

[19] *Ibid.*, sec 247.

[20] Igor Alexeff and Rodger Neidigh, *Apparent Observations of Ionic Sound Waves in an Arc Plasma*, ORNL CF-61-2-57 (Feb. 13, 1961), Appendix; Igor Alexeff, *Thermonuclear Div. Semiann. Rept. Jan. 31, 1961*, ORNL-3104, pp 40–45.

[21] Acknowledged as private communication in refs 23 and 24.

[22] F. W. Crawford, *Frequency Spectra of Low Frequency Fluctuations in a Plasma*, W. W. Hansen Laboratories of Physics, Stanford Univ. Microwave Laboratory, ML-762 (November 1960).

[23] F. W. Crawford, *Low Frequency Fluctuations in Plasma; Generation Mechanisms and their Suppression*, W. W. Hansen Laboratories of Physics, Stanford Univ. Microwave Laboratory, ML-813 (May 1961).

[24] F. W. Crawford, *Phys. Rev. Letters* 6, 663 (1961).

number of electrons per cm^3, n_e. As the plasma has approximately equal numbers of electrons and ions, the number of ions per cm^3, n_i, may be substituted for n_e in the denominator. The formula for the velocity is now

$$v = \left(\frac{\gamma k n_e T_e}{n_i m_i} \right)^{1/2} .$$

Dimensionally, the formula now has the form of a pressure term, divided by a mass density term.

The formula is quite analogous to the formula for the velocity v of an ordinary sound wave in a gas,

$$v = \left(\frac{\gamma P}{\sigma} \right)^{1/2} .$$

Here σ is mass per unit volume, and P is pressure per unit area.

In the case of a plasma, the term $n_i m_i$ is mass per unit volume, σ_i. Therefore, the quantity $k n_e T_e$ might represent an actual physical pressure P_e due to the plasma electrons.

Observation of plasma electron pressure was considered possible in the mode I arc with refluxing primary electrons. Calculations show that under typical operating conditions, a thrust on the electrode at the anticathode end of about 100 dynes can be expected. Calculations show that the force of the plasma electron pressure should be considerably greater than that due to bombardment by the incident electron beam from the cathode. Forces due to ion and electron streaming might not be present, since the cathode and anode of the reflux discharge are both at the same end.

Measurements of the plasma electron pressure were made with a mechanical pendulum, as shown in Fig. 3.25. The pendulum is made of a small square of sheet tantalum supported by a tungsten wire. Both a frictionless support and electrical insulation are provided by a glass fiber, used as a torsion bearing. Not shown in Fig. 3.25 is an oscillation-damping ring, located at the pendulum pivot. The pendulum could be removed from the plasma column while the apparatus was operating.

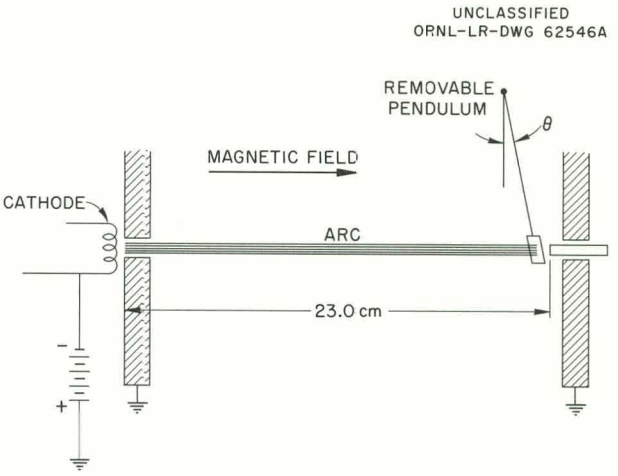

Fig. 3.25. Apparatus for the Measurement of Plasma Electron Pressure.

For a quantitative verification of the plasma electron pressure, the force measured by the pendulum must be compared with the force computed from theory. For computing the theoretical value for the plasma electron pressure, $P_e = k n_e T_e$, both the electron temperature T_e and the electron density n_e must be known. Measuring the electron temperature can be done by several methods – the Langmuir probe, ionic sound waves, and spectroscopic techniques. Measuring the electron density proved to be difficult. The Langmuir probe in the mode I arc could not be used, and microwave techniques were unavailable. A new method of measuring ion density in the mode I arc was developed. This method, called the plasma sweeper, is discussed later in this report.

Experimental measurements of the force exerted by the mode I arc on the recoil pendulum are compared with the theoretically predicted force in Table 3.4. The agreement between experimental and theoretical results seems to be within a factor of 2. These measurements are preliminary, and no further comment on the accuracy of the various quantities is justified.

Table 3.4. Electron Temperature (ev)

Gas	T_e			Electrons per Centimeter (electron density × plasma column cross section)	Theoretical Plasma Force (dynes)	Observed Plasma Force (dynes)
	According to Ionic Sound	According to Langmuir Probe	Average			
Argon (3 runs)	41	34	38	9.0×10^{11}	55	30
Deuterium (1 run)	22	42	32	1.7×10^{11}	8.7	6.0

3.3 THE PLASMA "SWEEPER," A DEVICE FOR MEASURING THE DENSITY AND OTHER PROPERTIES OF A PLASMA

I. Alexeff R. V. Neidigh

3.3.1 Measurement of Ion Density

Measuring plasma density in a magnetic field is difficult. The conventional Langmuir probe technique may not work, because the required electron current saturation often is obscured. Microwave methods are complex and have limited application. A simple plasma collection method has been developed, and its application to a mode I type of arc will be described. Measurements are made by turning off the source of plasma, then sweeping out and collecting the plasma from the column.

A schematic diagram of the mechanism is shown in Fig. 3.26. Instead of electrically insulating the anticathode, it is connected to ground through a resistor and a battery. However, the voltage of the battery is so chosen that the anticathode draws no net current; effectively, it is still floating. In practice, the correct battery voltage is a few volts greater than the cathode potential.

The ion density in the plasma column is measured by shorting the cathode to ground by a fast-closing switch. In our measurements a relay with mercury-wetted contacts was used. Since the anticathode bias remains, there is a flow of the plasma ions to the anticathode. The fall of cathode potential triggers the sweep on the monitoring oscilloscope. The current to the anticathode as a function of time is recorded as a voltage drop across the low resistance R_2 in the anticathode circuit. The total positive

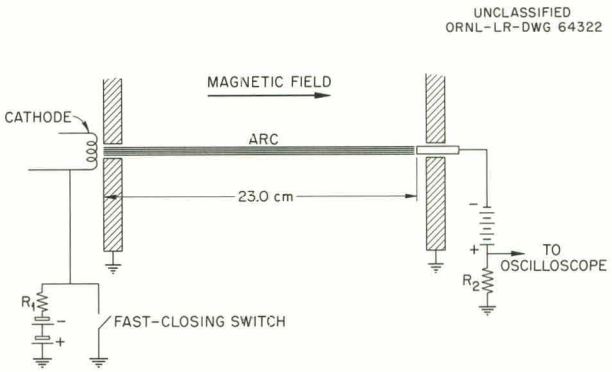

Fig. 3.26. Apparatus for the Measurement of Ion Density by the Method of Charge Separation and Collection.

charge contained in the plasma column is easily obtained by integrating the area under the current-vs-time-decay curve. Dividing the total positive charge by the volume of the plasma column yields an average value for the ion charge per unit volume.

The plasma sweeper technique of charge separation and collection seems to yield the correct ion density. The collection curves are of reasonable shape.[25] Recombination as an ion loss mechanism does not appear to be serious. The signal due to ion current is present much longer than light is emitted from the plasma, which suggests that ion recombination is not a significant loss mechanism. Finally, the values of ion density obtained by the plasma collection,

[25] Igor Alexeff, R. V. Neidigh, and E. D. Shipley, "Experimental Study of a Plasma Associated with an Electron Stream" (sec 3.3.3 this report).

when combined with the measurements of the plasma electron pressure, give the correct values for the electron temperature.[26]

3.3.2 Measurement of Ion Temperature and Other Properties

The experimental technique for studying the structure of a magnetically confined plasma by collecting the ions has been described.[27,28] It is possible that this technique for collecting the ions may reveal their density and velocity distributions, and give a value for their temperature. This report analyzes the collection of a plasma model, and compares it with an experimental collection given in ref 28.

A plot of ion current to the collector vs time can readily be calculated for a simple plasma. Assume a plasma column of uniform cross section and uniform ion density all along its length. The ions in the plasma are assumed to have initially a Maxwellian velocity distribution.

After the cathode is shorted to ground, as previously described,[27] the plasma undergoes charge separation and collection. The electrons will at all times distribute themselves so that charge neutrality in the plasma will be maintained. Thus the rate of plasma collection is governed by the rate of escape of the slowly moving ions.

A further assumption is that, during the collection, each ion preserves the velocity that it had when the cathode was shorted to ground. This assumption implicitly involves two parts: first, during collection, the interaction of an ion with the plasma is small; second, the sweeping voltage applied to the plasma column does not influence the ion drift appreciably. Another way of stating the second part is that the sweeping voltage applied to the plasma column appears only across short plasma sheaths at the ends of the column. Perhaps ions reaching the sheath at the positive end are reflected. In this case, the plasma column mathematically would be twice its physical length.

Under the above assumptions, the rate of collection of a plasma column is computed. Ions are assumed to escape from both ends of the column. Let L be the length of the plasma column and A be the cross-sectional area. At time t in the time interval dt, the number dQ_x of particles from the volume $A\ dx$ escape from the end at $x = 0$:

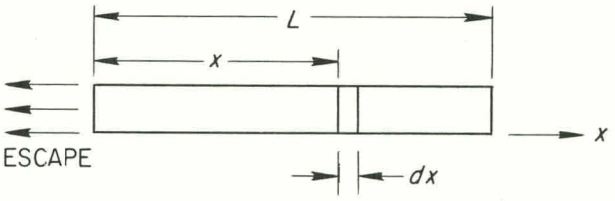

The particles escaping are those having a velocity $v_x = -x/t$. Hence, the particles escaping lie in the velocity interval, $dv_x = x/t^2\ dt$. Thus, the rate at which particles from the volume $A\ dx$ are escaping from the end of the plasma column at time t is

$$A\frac{dQ_x}{dt} = A\frac{(dN_0/dv_x)\,dv_x\,dx}{dt},$$

$$= A\frac{(dN_0/dv_x)(x/t^2)\,dt\,dx}{dt},$$

$$= A\frac{x}{t^2}\frac{dN_0}{dv_x}dx.$$

Here $A\,(dN_0/dv_x)\,dv_x\,dx$ is the number of ions in the volume $A\ dx$ having a velocity in the range $v_x\ dv_x$ at time $t = 0$. The Maxwellian velocity distribution of the ions at point x is[29]

$$\frac{dN_0}{dv_x} = \frac{1}{(\pi)^{1/2}}\left(\frac{m}{2kT_i}\right)^{1/2} N_0 \exp\left(-\frac{mv_x^2}{2kT_i}\right).$$

Here m is the ion mass, k is Boltzmann's constant, T_i is the ion temperature, N_0 is the number of ions/cm^3, and v_x is the velocity in the x direction. This distribution may be substituted

[26] Igor Alexeff and R. V. Neidigh, "Ionic Sound Waves in Mode I Arcs" (sec 3.2.2 this report).

[27] Igor Alexeff and R. V. Neidigh, "Measurement of Ion Density," this report, sec 3.3.1.

[28] Igor Alexeff, R. V. Neidigh, and E. D. Shipley, "Experimental Study of the Plasma Associated with an Electron Stream," this report, sec 3.3.3.

[29] J. D. Cobine, *Gaseous Conductors*, p 18, Dover, New York, 1958.

into the equation for the rate of particle escape:

$$A\frac{dQ_x}{dt} = A\frac{x}{t^2}\frac{1}{(\pi)^{1/2}}\left(\frac{m}{2kT_i}\right)^{1/2} N_0 \times \exp\left[-\frac{m}{2kT_i}\left(\frac{x}{t}\right)^2\right] dx .$$

Let dQ/dt be the ion flux out of the whole column at time t. This quantity is easily found by integration:

$$A\frac{dQ}{dt} = A\int_0^L \frac{dQ_x}{dt}\,dx = AN_0\frac{1}{(\pi)^{1/2}}\left(\frac{m}{2kT_i}\right)^{1/2}\frac{1}{t^2} \times \int_0^L \exp\left[-\frac{m}{2kT_i}\left(\frac{x}{t}\right)^2\right] x\,dx .$$

The integration can be easily performed if the following substitution is made:

$$u = \left(\frac{m}{2kT_i}\right)^{1/2}\frac{x}{t} .$$

The result is:

$$A\frac{dQ}{dt} = AN_0\frac{1}{2(\pi)^{1/2}}\left(\frac{2kT_i}{m}\right)^{1/2} \times \left[1 - \exp\left(-\frac{m}{2kT_i}\frac{L^2}{t^2}\right)\right].$$

If the equation is multiplied by the charge on an ion, e, the value for the positive ion current i_+ is obtained:

$$i_+ = eA\frac{dQ}{dt} .$$

Unless some sort of an electric field is present at the end of the plasma column, the ion current is not observed because an equal electron current i_- flows out with the ion current.

The structure of the plasma collection equation is best seen when it is exhibited in reduced form. Let the reduced time

$$t_{\text{reduced}} = t\left[\frac{1}{L}\left(\frac{2kT_i}{m}\right)^{1/2}\right],$$

and let the reduced current

$$i_{+\text{ reduced}} = i_+\left[\frac{2(\pi)^{1/2}}{eAN_0}\left(\frac{m}{2kT_i}\right)^{1/2}\right].$$

Then the reduced equation is

$$i_{+\text{ reduced}} = 1 - \exp\left[-\frac{1}{(t_{\text{reduced}})^2}\right].$$

The theoretical collection curve is shown in Fig. 3.27. Two characteristic features are evident: a flat initial portion and a subsequent decay of t^{-2}. The flat portion indicates approximately constant current for a time in which an ion of average energy could travel the length of the plasma column.

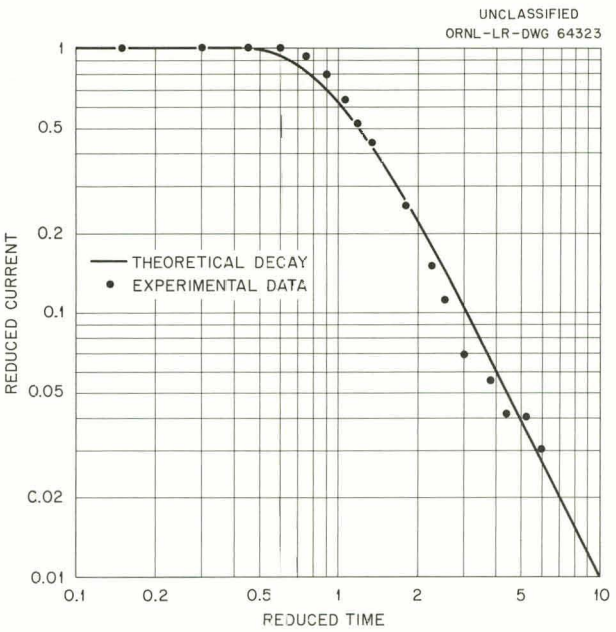

Fig. 3.27. Comparison of a Theoretical Ion Current Collection Curve with That of an Actual Plasma Formed by an Electron Stream. The theory assumes a plasma column of uniform central density, uniform cross section, and a Maxwellian distribution in ion velocity.

Experimental data, taken from Fig. 3.28 (lower left trace) of this report, are compared with the theoretical curve as shown in Fig. 3.27. The experimental points fit the theoretical curve quite well. If the length of the plasma column L is assumed to be equal to its geometrical length, then the ion temperature, T_i, is 12 ev. This is a reasonable ion temperature for the experimental apparatus. However, if ions are reflected by a sheath at the positive electrode, this assumption on the plasma column length may be low by a factor of 2. This means that the previously mentioned ion temperature of 12 ev may be low. A second conclusion, which is independent of the adjustable constants in the equation, is that the experimental points correspond to a Maxwellian velocity distribution.

The method of plasma collection thus appears to be a useful tool in studying a plasma restricted by a magnetic field. The method certainly gives ion temperatures that are correct in order of magnitude, and it may be quite accurate. Checks by other methods are needed. A relative indication of the density distribution and velocity distribution is certainly obtained by this technique.

3.3.3 Experimental Study of a Plasma Associated with an Electron Stream

I. Alexeff R. V. Neidigh E. D. Shipley

The motivation for the experiment described here is twofold. First, a detailed investigation of the high-pressure region of a mode II arc might give a clue to the mechanism for producing the energetic ions which have been observed in its secondary plasma.[30] Second, a volume of plasma not bounded by the chamber walls is useful for the study of its confinement by the magnetic field. Experiments directed toward this latter objective are described in this section.

The volume of plasma was produced at the intersection of an electron stream along magnetic field lines from a negatively biased incandescent tantalum filament and a neutral gas jet perpendicular to the electron stream, as shown in Fig. 3.28. Cold-trapped diffusion pumps removed the un-ionized gas from the region and reduced the neutral density outside the stream to 10^{11} neutrals/cm^3 or less. The filament bias supply was shorted and the negative potential of the filament raised to ground potential in about 2 μsec, as shown on the lower left inset photo of Fig. 3.28. The plasma ions were then removed by the negatively biased collector at the anticathode end, and the potential developed across a 5000-ohm resistor was observed on an oscilloscope.

The collection curve for a uniformly filled column of plasma, for example, one with a Maxwellian distribution of ion energies,[31] can be calculated. Some confidence that the collector receives the plasma ions without greatly distorting its density distribution is obtained by noting some features of the observed collection curve for a uniformly filled column of plasma. The curve is shown in the lower right inset of Fig. 3.28. The flat portion indicates constant current during the time required for an ion of about 25 ev to travel the length of the arc. This is a reasonable value for the average ion energy in an arc of this kind. The subsequent decrease in current appears to yield a reasonable energy distribution.

The collection of the small volume of plasma generated, as indicated in Fig. 3.28, is depicted as a function of magnetic field strength in Fig. 3.29. Each photo is a multiple (5 or 6) exposure of the decay pattern. Notice that for argon at 300 gauss the collection curves fall upon one another, but as the field increases this becomes less true. In the case of nitrogen this lack of reproducibility is in evidence even at 500 gauss. At 3000 gauss the plasma is so turbulent that one of the collection patterns has two maxima. This also appears in the argon plasma, but it is not as pronounced as in the nitrogen plasma for a given field strength. In general the turbulence appears to increase with magnetic field strength and to decrease with increased ion mass.

The effect that magnetic mirrors placed at either end of the plasma volume (Fig. 3.28) had on the

[30] R. V. Neidigh, *The ORNL Thermonuclear Program*, ORNL-2457, pp 55, 164–65 (Jan. 15, 1958); R. V. Neidigh, *The Effect of a Pressure Gradient on a Magnetically Collimated Arc*, ORNL-2288 (May 27, 1957); R. V. Neidigh and C. H. Weaver, *Proc. U.N. Intern. Conf. Peaceful Uses Atomic Energy 2d, Geneva, 1958*, 31, 315 (1958).

[31] Igor Alexeff and R. V. Neidigh, "Measurement of Ion Temperature and Other Properties," this report, sec 3.3.2.

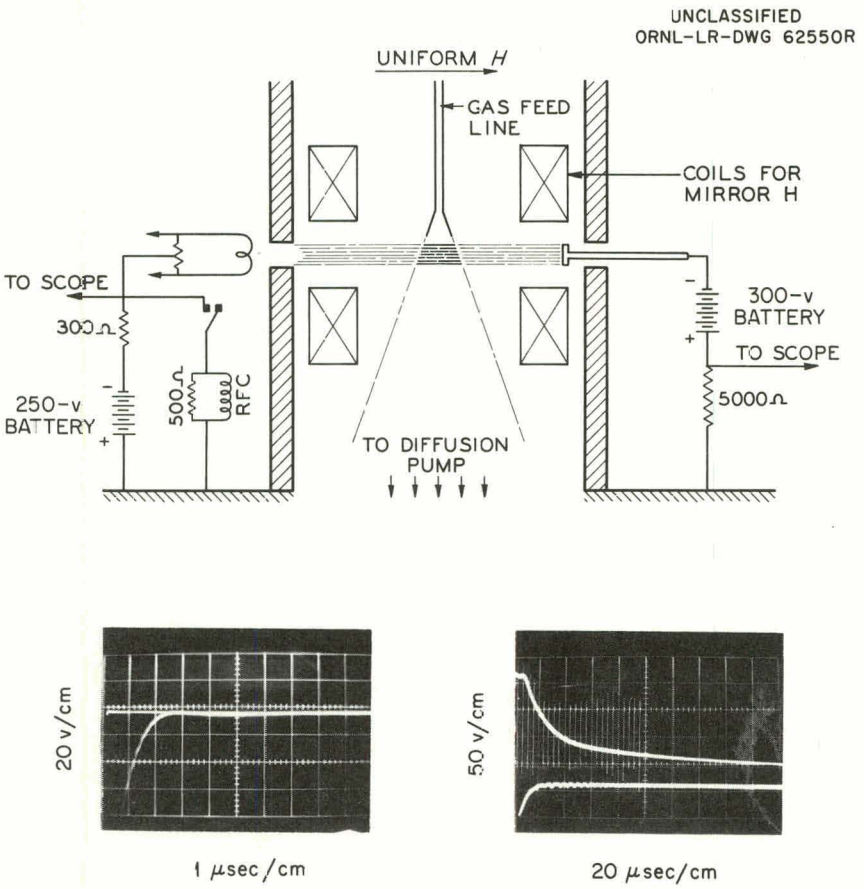

Fig. 3.28. Schematic Diagram of the Apparatus for Producing the Plasma Volume. Shown are the bias shorting circuit and the ion collecting circuit at the opposite end. The oscilloscope traces show the rapid turnoff of the bias voltage and the slow collector current decay for a uniformly filled column of plasma.

density of the plasma volume is shown in Fig. 3.30. The plasma density can be estimated from the area under the collection curves if a plasma volume is assumed. (One cubic centimeter was used to calculate densities given in the photos.) Plasma density is minimal in the upper photos and increases toward the bottom. Notice the decrease in vertical sensitivity necessary to accommodate the increased amplitude. In the upper photo the area under the curve for the uniform field is slightly less than for the corresponding curve in the mirror geometry. This was expected because of the additional containment provided along the Z axis by the mirror coils. But the collection in the mirror geometry appears more rapid. The ion density is about 10^{11} ions/cm^3. In the center photos only the magnetic field has been raised. The ion density is approximately doubled and appears to be as dense in the uniform geometry as in the mirror geometry. The density is up to about 10^{12} ions/cm^3 in the lower photos. Here the plasma appears to be less dense and to be collected more rapidly in the mirror geometry than in the uniform magnetic field.

The anomalous behavior of the plasma may be due to the additional turbulence observed in the plasma confined by the mirror geometry (Fig. 3.31). Compare the noise amplitude in the steady-state collector voltage (horizontal traces) for the two geometries. Notice that the noise amplitude is doubled in the mirror geometry. In these photos the ion density was raised to the values indicated by increasing the neutral gas feed. The collection curves on the same photos indicate that the plasma density is lower in the mirror geometry

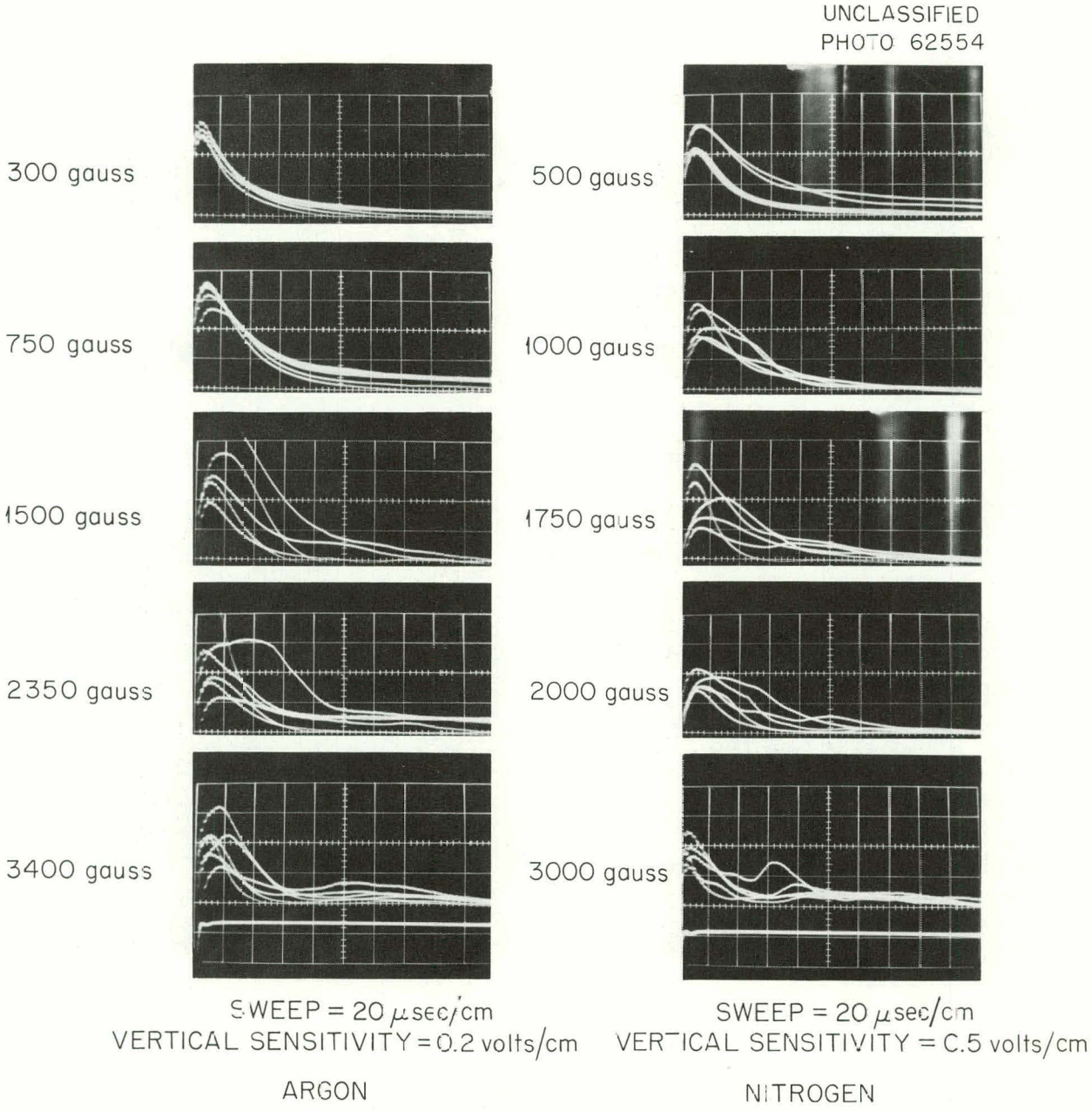

Fig. 3.29. Ion Collection Current vs Time for Argon and Nitrogen Plasmas. Note that increasing magnetic field increases the turbulence as indicated by lack of repetition of the collector current trace.

UNCLASSIFIED
PHOTO 62552

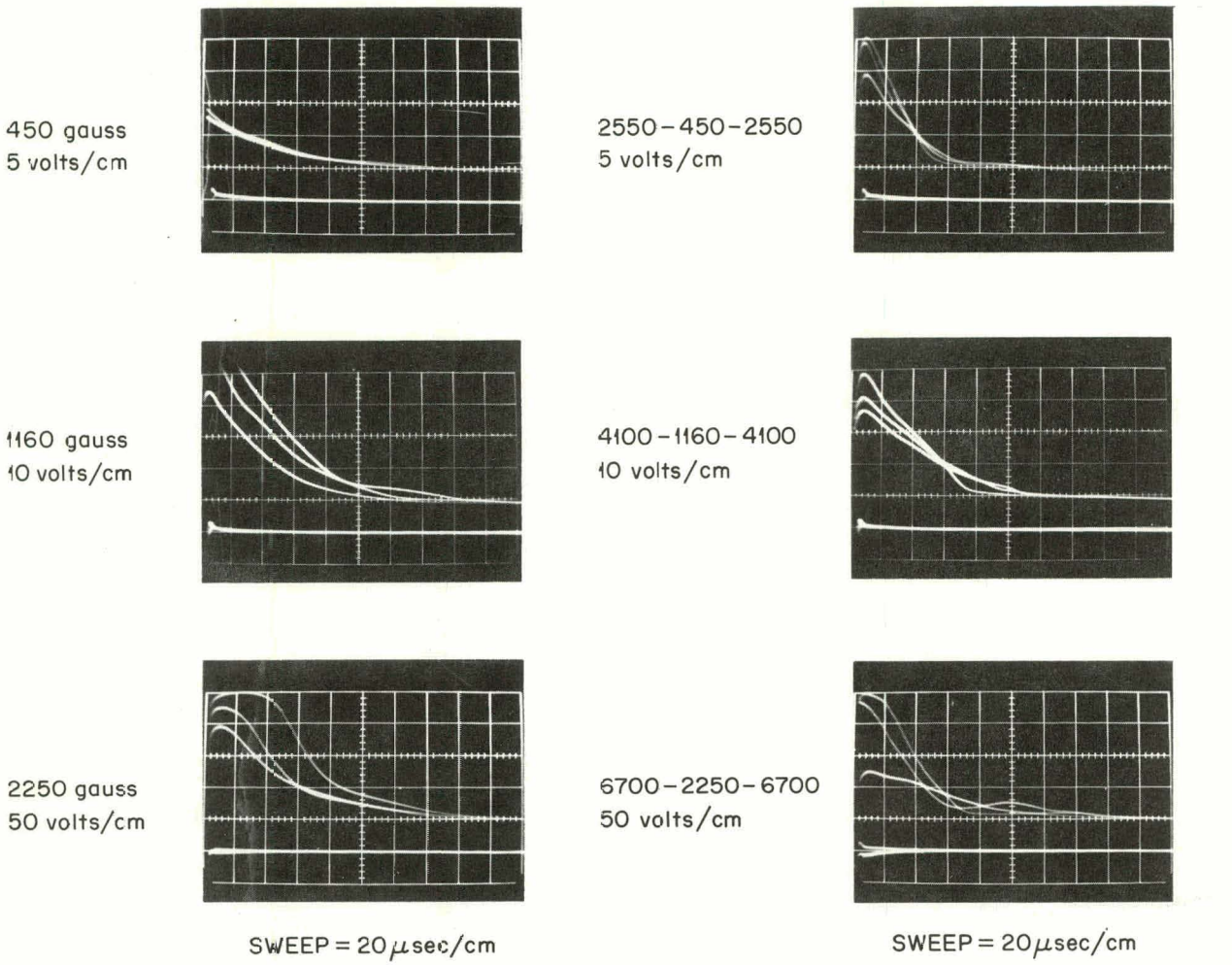

Fig. 3.30. Effect of Magnetic Mirrors on the Plasma.

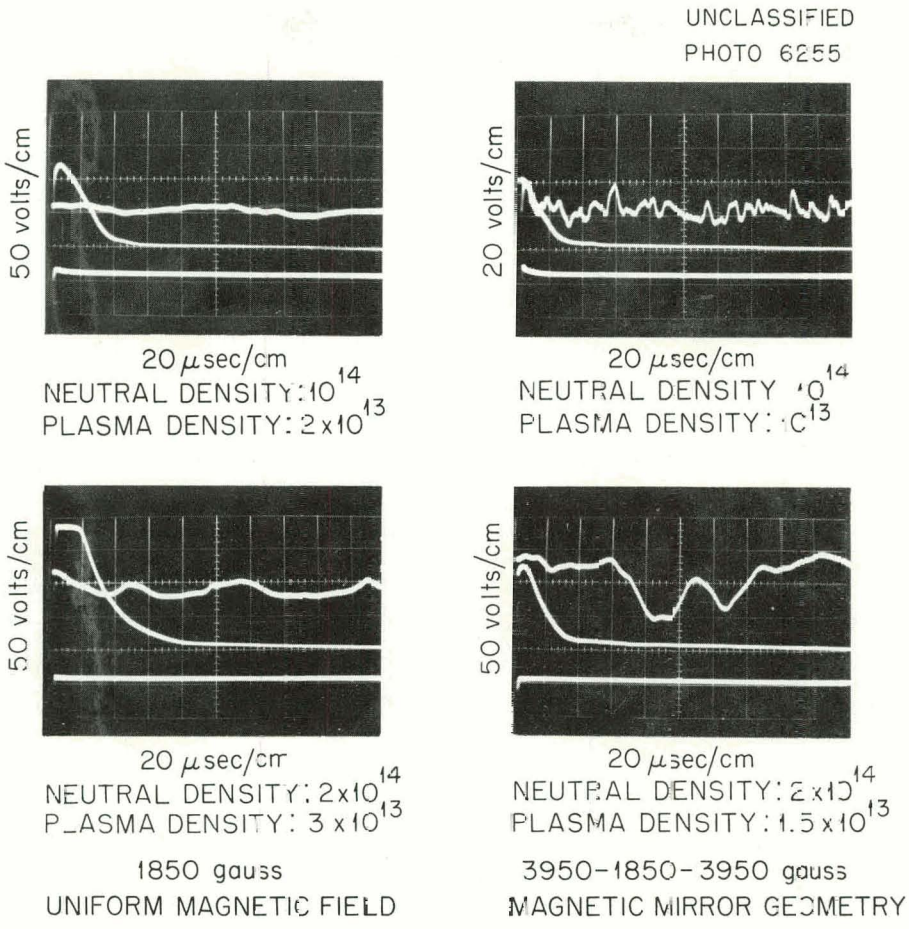

Fig. 3.31. Effect of Magnetic Mirrors vs Uniform Field at Increased Neutral Density. The horizontal traces with the variable ordinates are the steady-state voltage on the collector before turnoff of the bias voltage.

by a factor of about 2. This may not be real since in the uniform geometry the plasma volume may be larger. The greater turbulence in the mirror geometry may, according to current theories, be due to the lack of the short-circuiting and therefore stabilizing effect on the plasma by the conducting end walls.

There is apparently some transport of ions across the magnetic field due to the plasma turbulence which sets in at about 500 gauss for argon. The ion current to the collector at the anticathode end is compared with the ion current to a collector ring around the edge of the center collector also at the anticathode end in Fig. 3.32. The area under the curves of plasma-collector current (total charge) to the center collector increases with increased magnetic field, but not as fast as the area under the curves of plasma-collector current to the edge collector. Notice that the area under the edge-collector curve has more than doubled in the magnetic field step from 250 to 500 gauss, while the total current to the center collector is about the same. (The ion density is about 10^{11} ions/cm^3.) Ion transport across the magnetic field is even more pronounced in the 1500-gauss range, but at this field strength the ion cyclotron frequency is in resonance with the ionic sound wave,[32] and an energy transfer was expected.

These experiments give only a qualitative picture of turbulence in a plasma generated by a refluxing electron stream and removed by an electric field. However, the data indicate a real

[32] Igor Alexeff and R. V. Neidigh, "Ionic Sound Waves in Model Arcs," this report, sec 3.2.2.

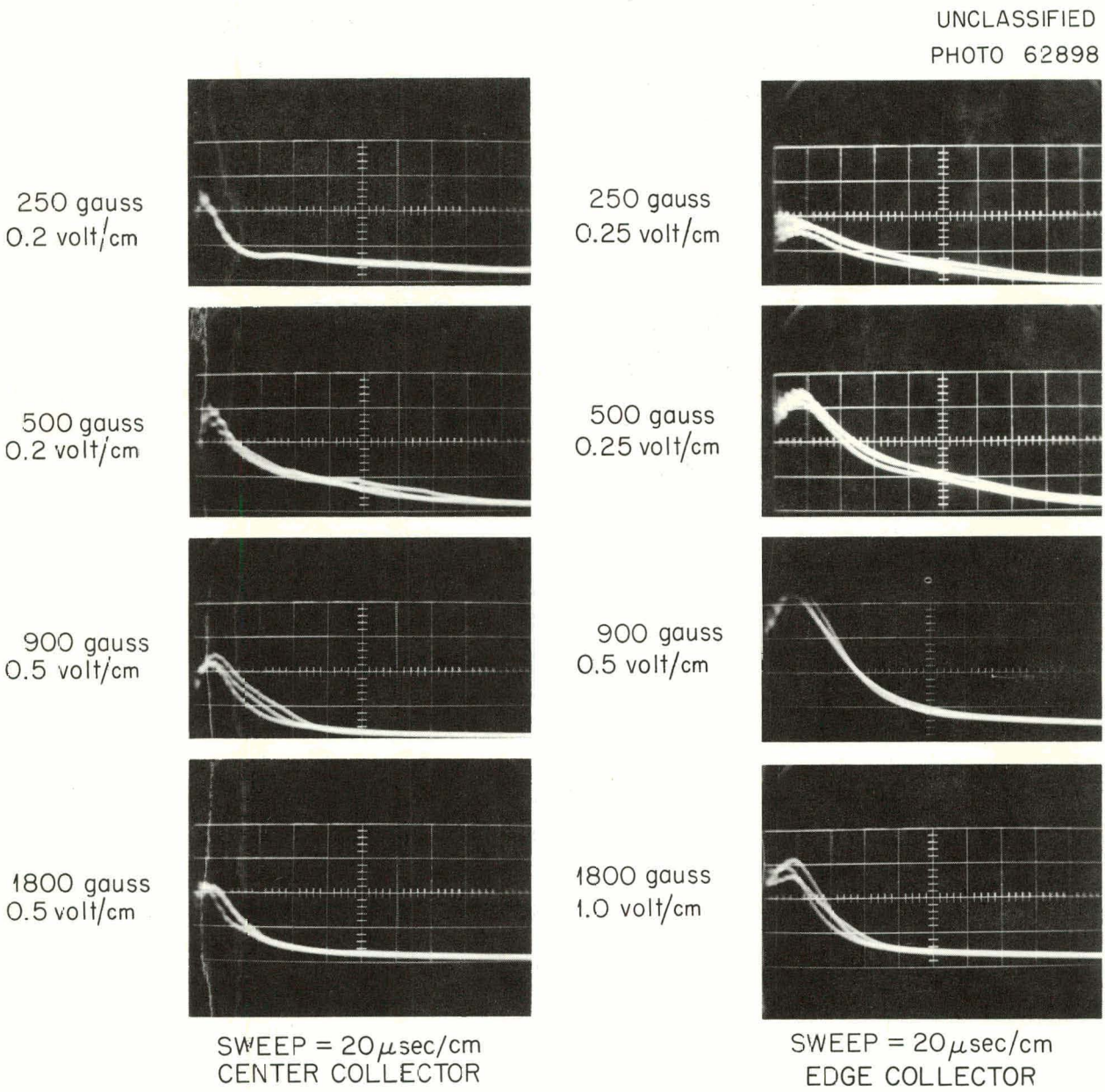

Fig. 3.32. Evidence of Ion Transport Across the Magnetic Field. The total ion current to the edge collector increases faster than the total current to the center collector as the magnetic field is increased.

increase in turbulence with increasing magnetic field, and increasing turbulence with decreasing ion mass for a given magnetic field. The data also indicate a transport of ions across the magnetic field as a result of this turbulence, and the effect is enhanced by the mirror geometry.

3.4 PRELIMINARY STUDIES OF THE INTERACTION BETWEEN AN ION BEAM AND ITS SECONDARY PLASMA

O. C. Yonts[33] E. D. Shipley
A. M. Veach R. N. Goslin[34]

The purpose of this program is to study an ion beam in a magnetic field in somewhat simpler surroundings than in a DCX apparatus. Detailed studies of alteration of beam trajectories by space charge or by density variation (ion and neutral particle) were undertaken. Secondary plasma associated with the beam was studied by sampling the charged particles streaming out along the magnetic flux lines.

The equipment used in the work uses the vacuum-magnetic field of an experimental beta tank and is shown in Fig. 3.33. It consists of an ion source (*A*), a collector (*B*) at the 180° focus, and a movable slide carrying a Faraday cup (*C*). The ion beam is approximately 10 cm wide and is centrally located between the side plates (*D*). Gas pressure in the beam region can be changed by admitting gas or by throttling the diffusion pumps. A stream of neutral gas particles can also be directed across the ion beam through the nozzle (*E*).

Charged particles streaming out of the plasma along the magnetic field are detected by the Faraday cup (schematic drawing of the Faraday cup is shown in Fig. 3.34). In this form it is used to observe slow ions streaming from the beam region. A typical curve showing variation of slow-ion current with pressure is shown in Fig. 3.35. The region *A* corresponds to change of current due to increased charge exchange and ionization by the primary beam. Region *B* contains more ionizing events than can be accounted for by charge exchange and direct ionization by the beam. This means that there are either supplementary ionizing events or that ions are arriving at the collector after crossing the magnetic field and the collector is in effect drawing current from a larger volume.

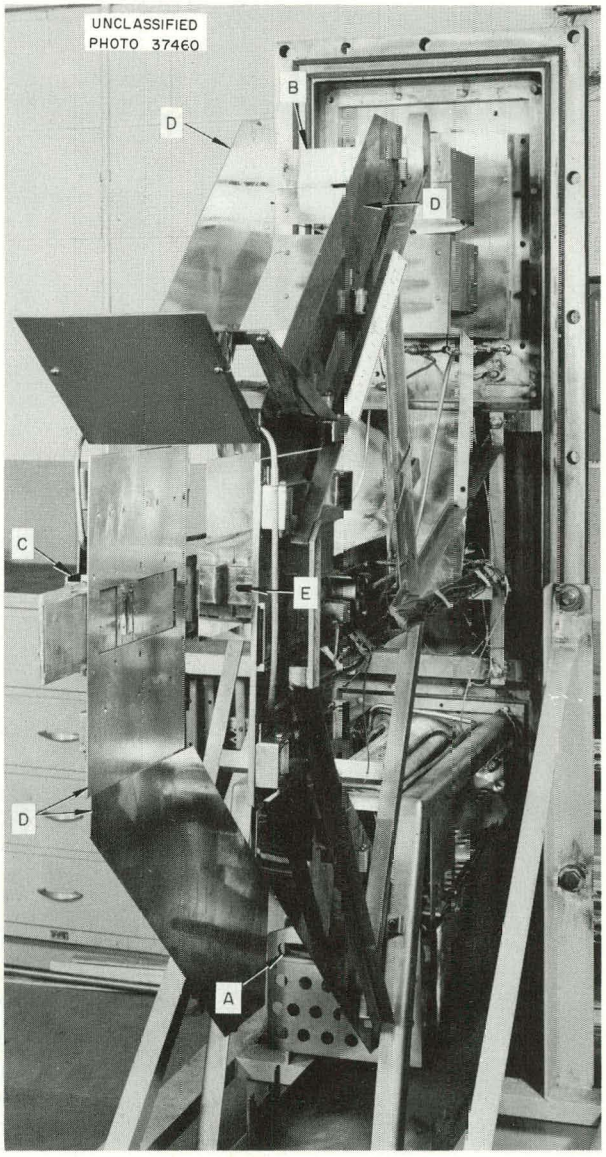

Fig. 3.33. Photograph of Equipment Showing Location of Parts.

If the Faraday cup is now arranged as shown in Fig. 3.36, values of the current arriving at the collector for different values of collector voltage can be obtained. Values obtained for the *A* and *B* region of Fig. 3.35 are shown in Fig. 3.37.

[33] Isotopes Division.

[34] Consultant, Oglethorpe University, Atlanta, Ga.

The maximum energy of the ions should not be interpreted as giving the maximum space potential since there is some preliminary indication that the energy is a function of time.

The authors wish to thank J. P. Wood and H. L. Huff for their assistance in operation and construction of the equipment.

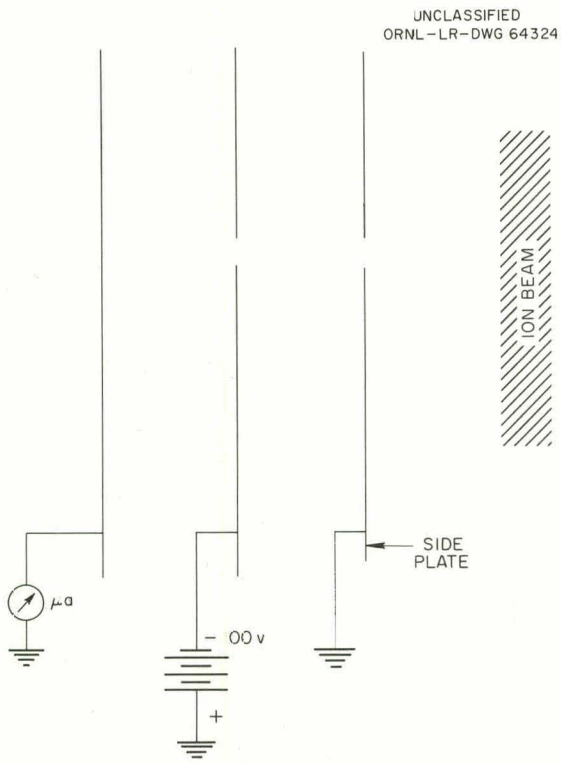

Fig. 3.34. Faraday Cup Schematic Biased to Receive Ions.

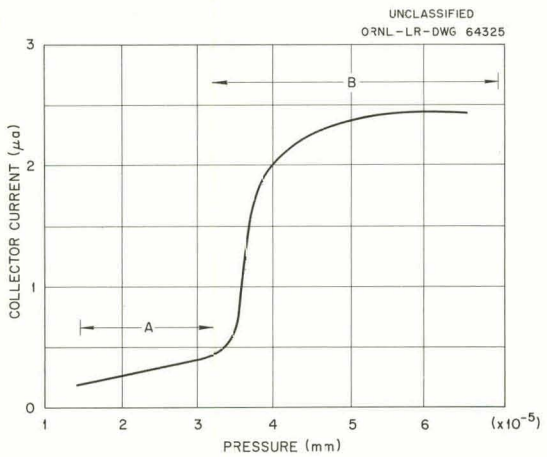

Fig. 3.35. Faraday Cup Collector Current vs Pressure for a 50-ma Ar^+ Ion Beam.

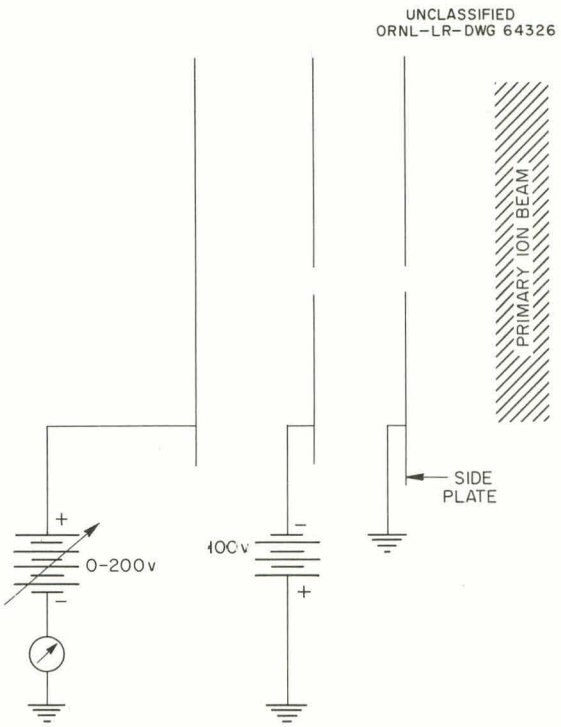

Fig. 3.36. Faraday Cup with Biased Collector.

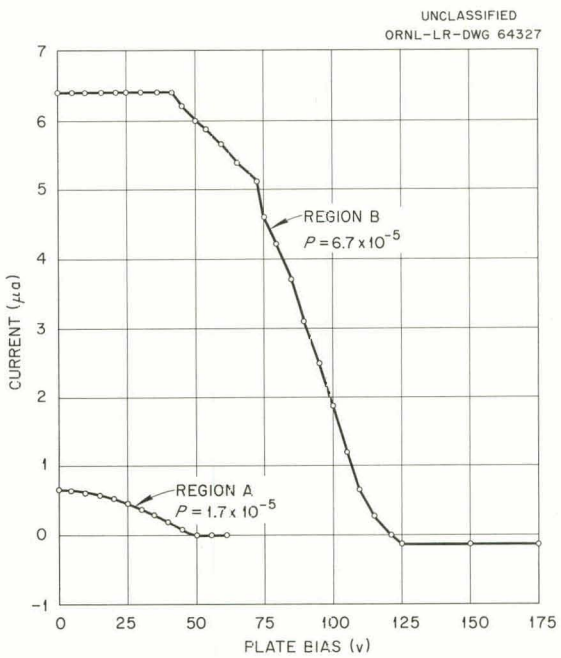

Fig. 3.37. Retarding Potential Curves for Slow Ions.

4. Vacuum Arc Research

4.1 THE CARBON ARC

4.1.1 High Ion Temperatures in the Magnetically Confined Carbon Arc

M. R. Skidmore J. R. McNally, Jr.

Previously, it was observed that the spectral half-width of the C^{2+} 4647-A triplet group increased linearly with the distance of the point of observation from the anode in a magnetically confined carbon arc.[1] The ion temperature, which is proportional to the square of the line half-width, increased approximately quadratically with this distance. The highest temperature was found to be 900,000°K for C^{2+} ions at a point 49 in. from the anode in a 54-in.-long arc.

A brief study has been made with a Jarrel-Ash–Ebert 8200 spectrometer of a long (84 in.) carbon arc in the 120-in. solenoid. The first experiment involved the use of a 4-in.-OD carbon anode and $\frac{1}{2}$-in. tapered tungsten cathode at fields of 7.5 to 9 kilogauss. Arc current was 115 amp and the arc voltage varied from 220 to 240 v. Outgassing was serious and the lowest pressure was 7×10^{-5} mm Hg. Without polarization separation the line width at half intensity as observed at a point 72 in. from the anode was only 0.52 A. A second run (using a 2-in.-OD carbon anode and a $\frac{5}{8}$-in. tapered tungsten cathode, no polarizer, and a short 10-μ-wide slit which reduced the instrument half-width from 0.27 to 0.17 A) gave half-widths ranging from about 0.4 to about 0.5 A with an average of 0.43 A. The half-width, corrected for instrumental broadening, was 0.37 A and corresponds to a C^{2+} ion temperature of about 150,000°K. Pressure was still high (4×10^{-5} mm Hg at the midpoint of the solenoid) and may account for this relatively low ion temperature.

The use of carbon for both electrodes gave much higher ion temperatures although this effect may be due to improvement in the operating pressure. Results of the first run are given in Fig. 4.1, and show a time-dependent effect of both the half-width, $\Delta\lambda$, of the 4647 C^{2+} line and the mid-solenoid pressure. A carbon cathode with a $\frac{1}{16}$-in. hole for starting with argon gas feed was used. The highest ion temperature attained was about 1,400,000°K. A π-transmitting optical polarizer was used and hence temperature corrections due to Zeeman contributions are about 3%; the slit correction is estimated to be about 3%.

The increase in spectral line width with distance from the anode is illustrated in Fig. 4.2. A slight line slant effect (due to Doppler shifts introduced by precession motion of ions about the arc axis) is discernible in the figure (compare 12th order 4650 line with 22nd order 2537 of Hg in bottom spectrum). The hollowness of the arc, as regards C^{2+} radiation, also appears to increase with distance from the anode. This may be due in part to the radial distribution of C^{2+} ions shifting outward as this ion class moves down the arc column or to the improved definition of the electron streams leaving the outer edges of the cathode. The Larmor diameter of C^{2+} ions having a mean energy of 120 ev and in a field of 8265 gauss is 0.63 cm, a figure comparable to the radius of the carbon arc. This suggests that the hollowness may be due mostly to a hollow spatial distribution of the electron stream from the cathode.

The Gaussian nature of the 4647 line profile was checked in two ways. The first method consisted in plotting the observed relative intensity vs $\Delta\lambda/\Delta\lambda_{1/2}$, normalizing to a maximum intensity of unity (see Fig. 4.3). The Doppler half-width $\Delta\lambda_{1/2}$ was evaluated at the half-intensity point and the theoretical Doppler curve (solid curve)

$$I = I_0 \exp[-\ln 2(\Delta\lambda/\Delta\lambda_{1/2})^2]$$

[1] P. M. Griffin *et al.*, *Thermonuclear Project Semiann. Rept. Jan. 31, 1960*, ORNL-2926, p 36, Fig. 2.13.

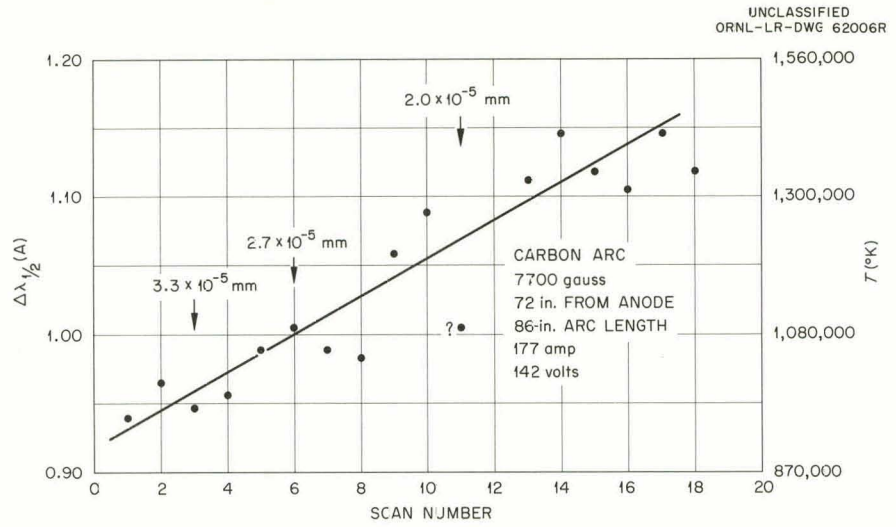

Fig. 4.1. Time Dependence of Doppler Half-Width and Ion Temperature.

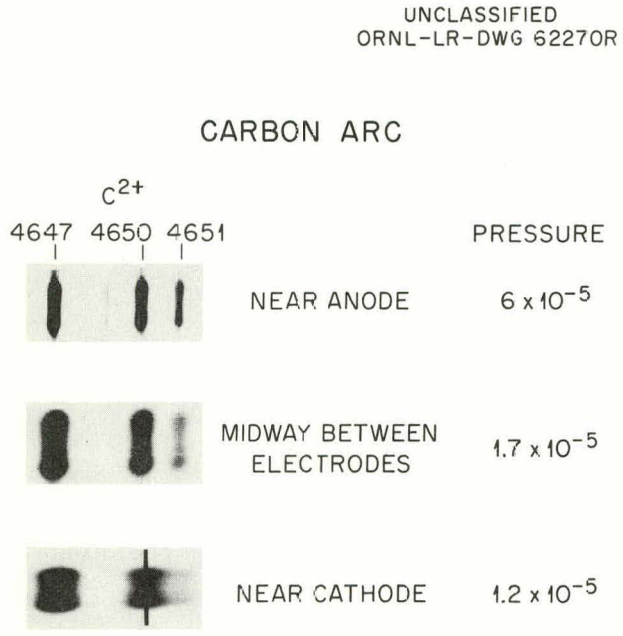

Fig. 4.2. Variation of Doppler Line Width with Distance from Anode in a 7-ft Carbon Arc (Transverse Observations).

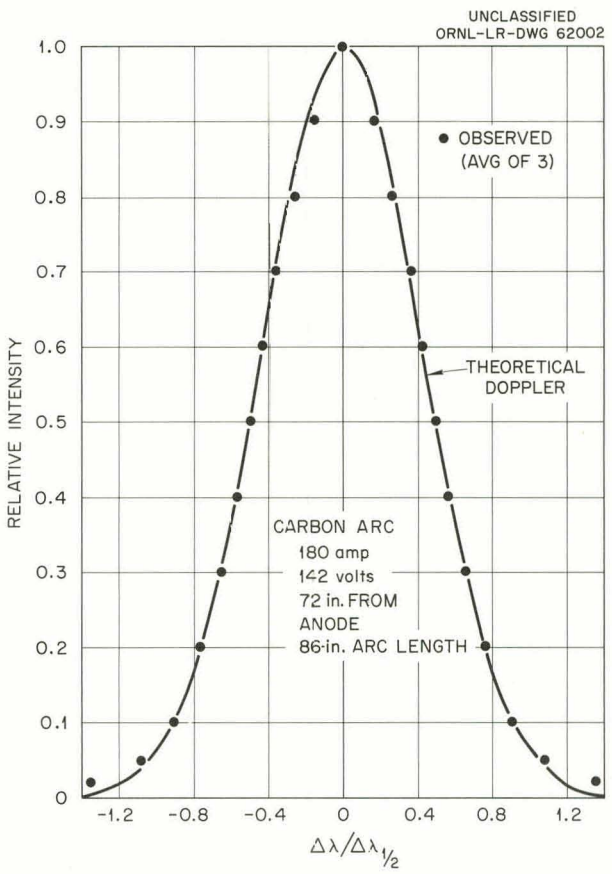

Fig. 4.3. Observed Line Profile vs Doppler Profile.

drawn for comparison. For this case $\Delta\lambda_{1/2} = 1.10$ A ($T = 1{,}300{,}000°K$) and $I_0 = 1.0$ define the Gaussian. This method utilizes only three points of the observed profile and is very sensitive to the choice of I_0.

A second method of verifying the Gaussian nature of these line profiles was used in which the log of the relative intensity is plotted against $(\Delta\lambda)^2$ (see Fig. 4.4). The intercept of this line for $(\Delta\lambda)^2 = 0$ is log I_0 and the slope of the line determined $\Delta\lambda_{1/2}$ to be 1.155 A ($T = 1{,}430{,}000°K$) for this case. The straightness of this plot demonstrates that the profile is Gaussian down to about 5% of the peak intensity.

Figure 4.5 shows the dependence on magnetic field of the half-width and the ion temperature. Arc voltage increased monotonically with magnetic field increase. For 5500 gauss and for 15,100 gauss there was considerable arc flutter; precision, as shown, is much worse than for intermediate fields. The ion temperature of about 1,400,000°K is the highest that has been observed to date in these magnetically confined, high-current, vacuum carbon arcs. The β for this case is estimated to be of the order 0.1%.

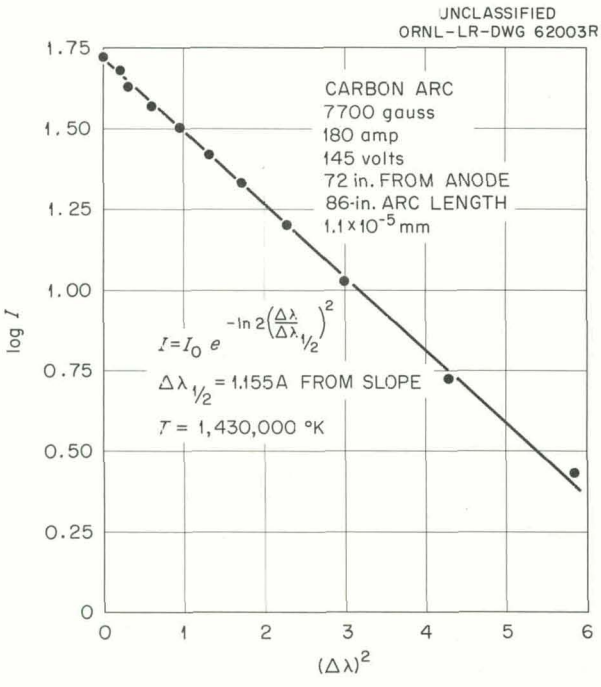

Fig. 4.4. Evaluation of Half-Width and Temperature from Best-Fitting Gaussian.

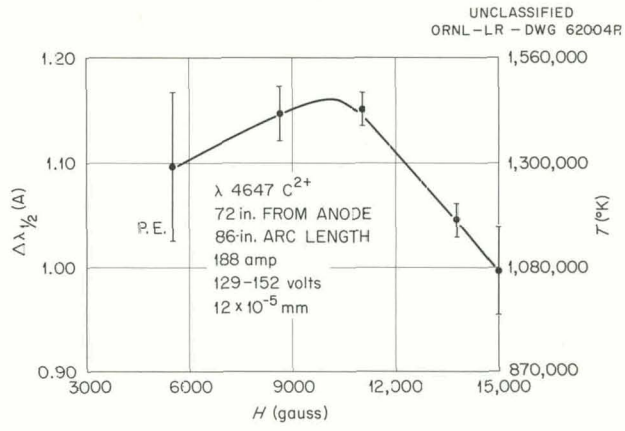

Fig. 4.5. Doppler Half-Width and Ion Temperature Dependence on Magnetic Field.

A rough check of the C^+ line at λ4267 A gave the same line half-width within 10% of the C^{2+} 4647-A line. It is hoped to evaluate later the question of equilibrium of the different ion species in more detail.

4.2 THE LITHIUM ARC

4.2.1 The Ion Current and Probe Measurements of the "Backstream"

J. E. Francis
C. L. Rogers[2]
P. M. Jenkins
P. R. Bell

Operating characteristics of the split anode shown in Fig. 4.6 for lithium arcs have been investigated. The relative distribution of power to the two sections of the anode was determined by measuring the heat input to the water cooling coils. For an arc of 95 amp and 140 v, the power to the backstop was 5680 w and the power to the front section was 605 w. This corresponds to 42.7% of the input power delivered to the backstop and 3.4% of the input power delivered to the stainless steel front section.

Several experiments were performed in order to determine the amount of lithium transported along the arc as ions. A cathode and baffle arrangement was used as shown in Fig. 4.7. In operation, lithium is condensed on the floating water-cooled

[2]Research participant.

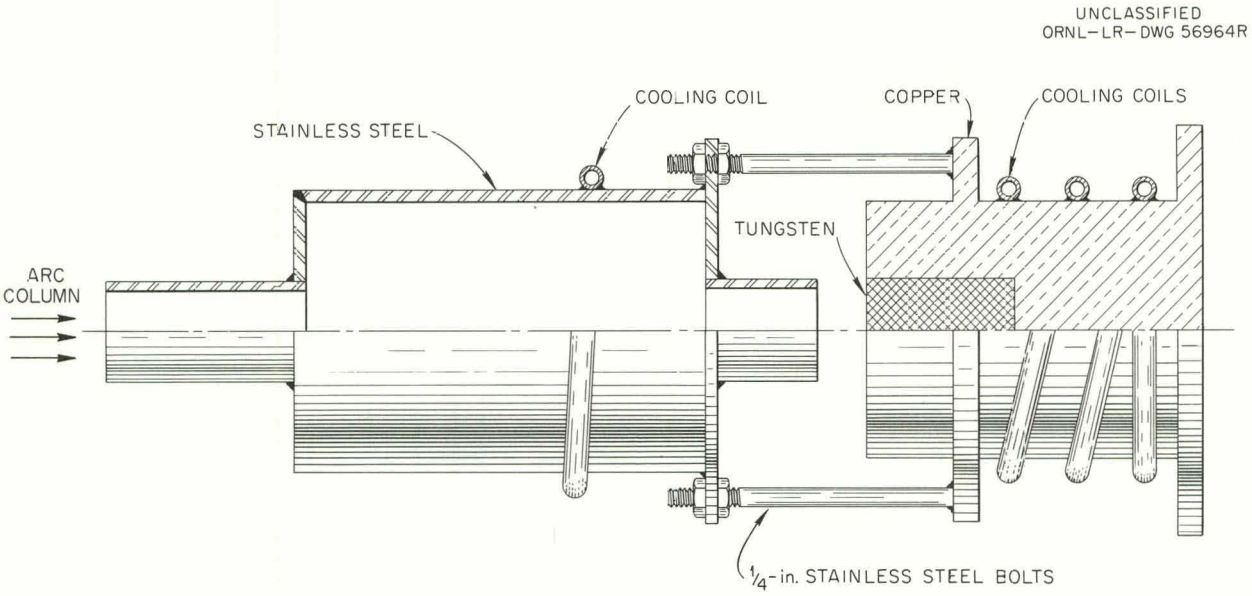

Fig. 4.6. Split-Anode Assembly.

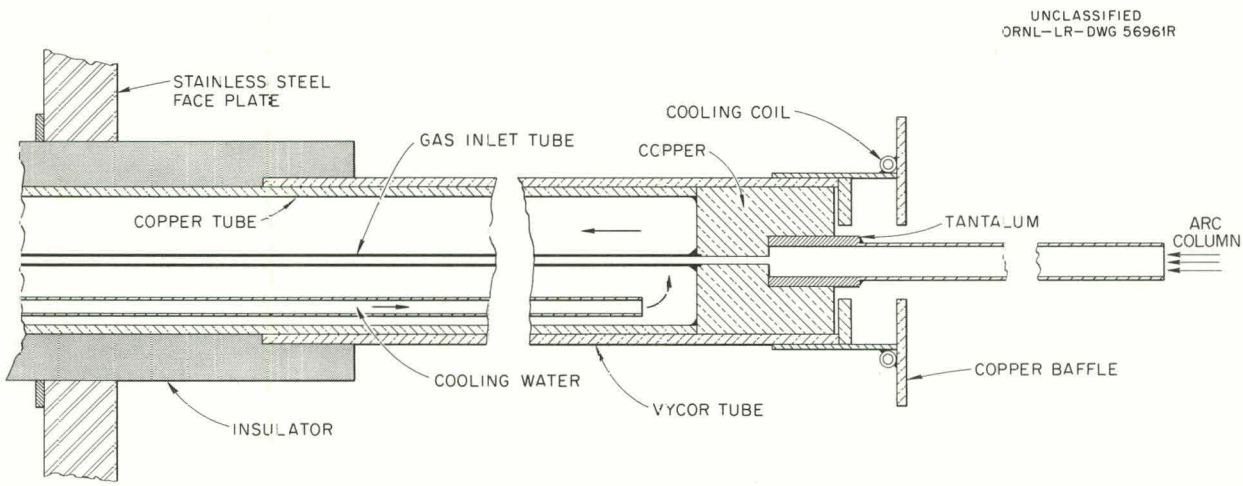

Fig. 4.7. Cathode Assembly for 120-in. Solenoid.

baffle and on the cool end of the cathode. The arc was operated for a time and a record kept of the arc current. At the end of the run the amount of lithium collected was washed off and the resulting solution was titrated. Using the assumption that the ion current was transported as Li^+, the coulomb equivalent of the lithium was found to be 0.062 or 6.2% of the arc current. Mass analyzer data indicated that the arc contained both Li^+ and Li^{++} as shown in Fig. 4.8 so that the percentage of arc current carried by ions is greater than 6.2% given by the coulomb equivalent. Previous results[3] indicate that the fraction of current carried by ions for an arc containing primarily Li^+ is at least 19%.

In order to measure the amount of lithium transported by the backstream, a right-angle cathode, shown in Fig. 4.9, was used. This cathode was

[3] J. E. Francis *et al.*, *Thermonuclear Div. Semiann. Progr. Rept. Jan. 31, 1961*, ORNL-3104, pp 53–54.

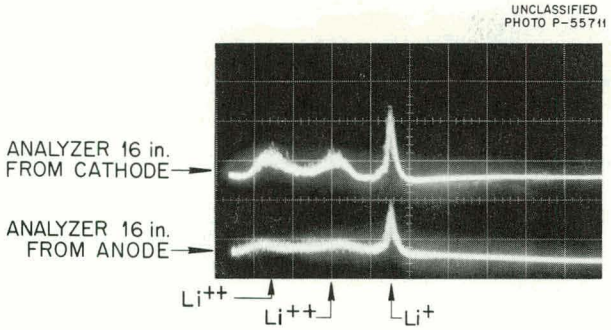

Fig. 4.8. Response of Neidigh Analyzers to Lithium Arc.

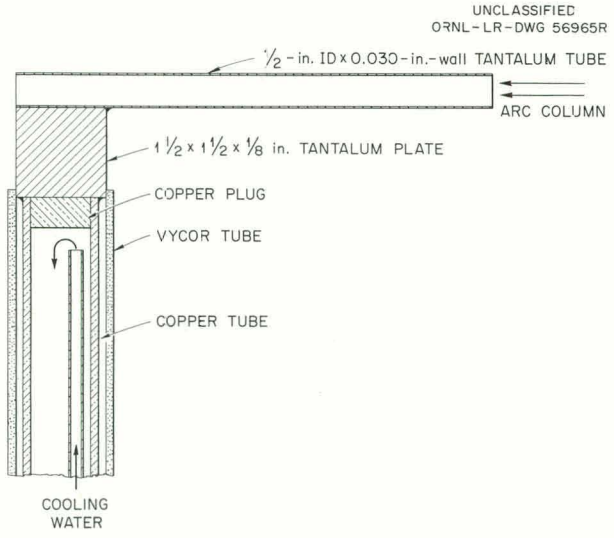

Fig. 4.9. Right-Angle Cathode.

then mounted in a side window of the tank to give an arc 52 in. long. The green sheath of the backstream continued past the cathode until it struck an insulated water-cooled baffle. The baffle was 32 in. back of the cathode. When the anode was operated without cooling water on the front stainless steel section the arc contained only Li^+ as indicated by the mass analyzer. Under these conditions a value corresponding to 9.6% of the arc current was obtained as the amount of lithium transported by the backstream. The same measurements were made with cooling water on the front section of the anode. The mass analyzer indicated approximately equal amounts of Li^{++} and Li^+. Under these conditions the coulomb equivalent of the lithium deposited on the baffle by the backstream dropped to 2.7% of the arc current.

The backstream contains Li^{++} when the main arc contains Li^{++}. This is demonstrated by Fig. 4.10. The upper trace shows the response of a mass analyzer to the backstream. The lower trace is the response of a mass analyzer to the main arc. It was also demonstrated that if a floating baffle containing a $\frac{1}{2}$-in.-diam hole is placed in the backstream a large portion of that which strikes the hole goes on through. Li^{++} is observed on the far side of the baffle when Li^{++} is present in the backstream.

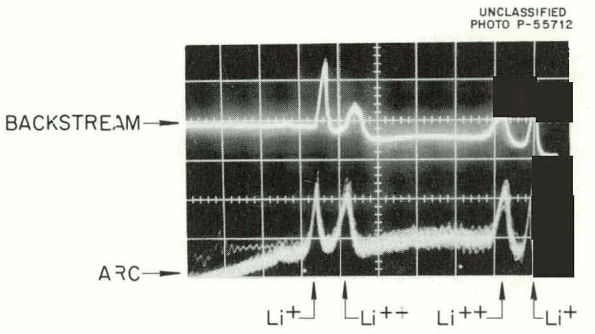

Fig. 4.10 Response of Neidigh Analyzers to Lithium Arc.

Langmuir probe measurements of the backstream were made in the elongated configuration shown in Fig. 4.11. Two probes were located on the axis of the arc respectively 64 and 112 in. back of the cathode. The field was 10^4 gauss at probe No. 1 and 210 gauss at probe No. 2. A diagram of the probe dimensions is shown in Fig. 4.12.

The measurements were of two types: floating potentials and dynamic probe characteristics. The floating potentials were made with the probe open-circuited using a dc voltmeter. The dynamic characteristics were obtained by use of the circuit shown in Fig. 4.13. Although the dc voltmeter was subject to error due to the effect of the field, the floating potentials measured with the meter compared favorably with those observed on the characteristics.

Floating potential measurements were made in an effort to determine the relative width of the backstream at the two probes. Measurements made at probe No. 1 have indicated a width of about 0.2 in.

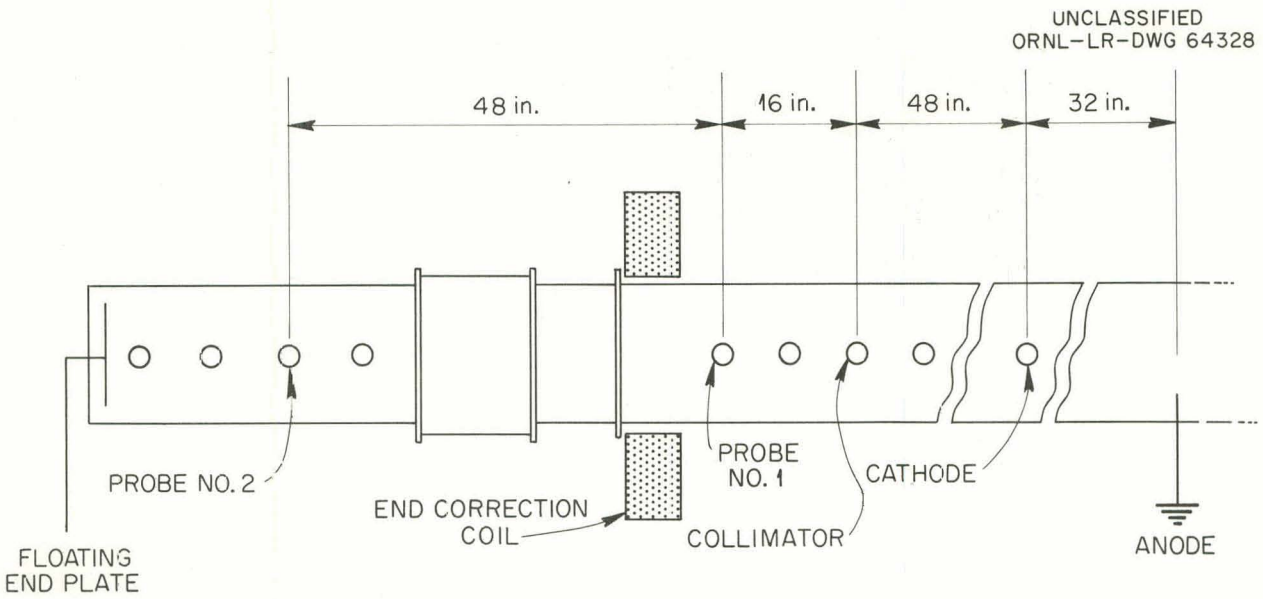

Fig. 4.11. Probe Locations.

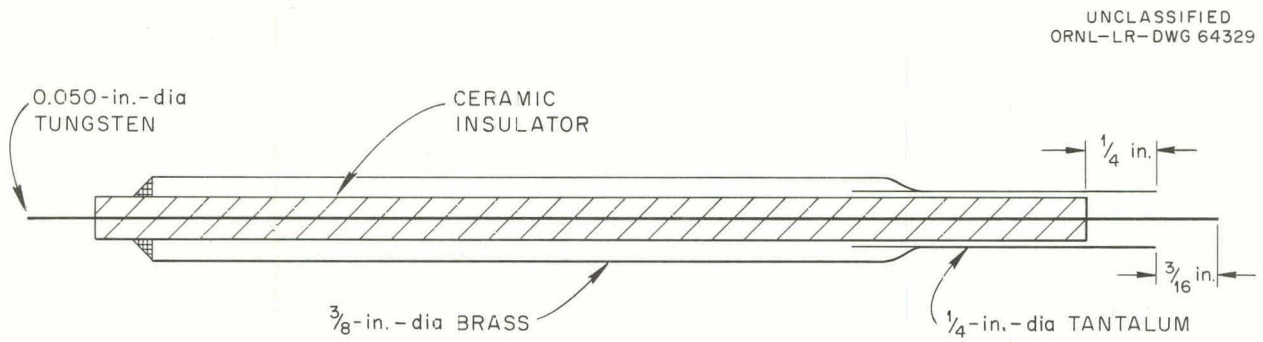

Fig. 4.12. Probe Construction.

at the point where the potential is reduced 30%. No consistent width has been determined at probe No. 2. The values vary from 0.6 to 5 in. Much of the difficulty encountered in measuring at probe No. 2 has been caused by the slight off-axis location of the arc which resulted in a curved backstream in the extension. As a consequence the stream was frequently out of reach of the probe. To alleviate this problem the probe was offset about $2\frac{1}{2}$ in. and inserted from the top of the extension (probe No. 1 was inserted from the side). Since the backstream is not symmetrical, this introduces errors in comparing the measurements of the two positions.

The potential measurements have indicated that the backstream at position 1 is frequently composed of three distinct regions: a central negative region of high negative potential, a positive potential region surrounding the central region, and another negative region surrounding the positive region. The outer negative region did not always appear; however, when detected, the potentials were usually of the order of a few tenths of a volt. The positive region was always present and had maximum potentials of about 2 v. Neither of these two outer regions have been observed in the extension. This absence is probably accounted for by the fact that the regions had dispersed to

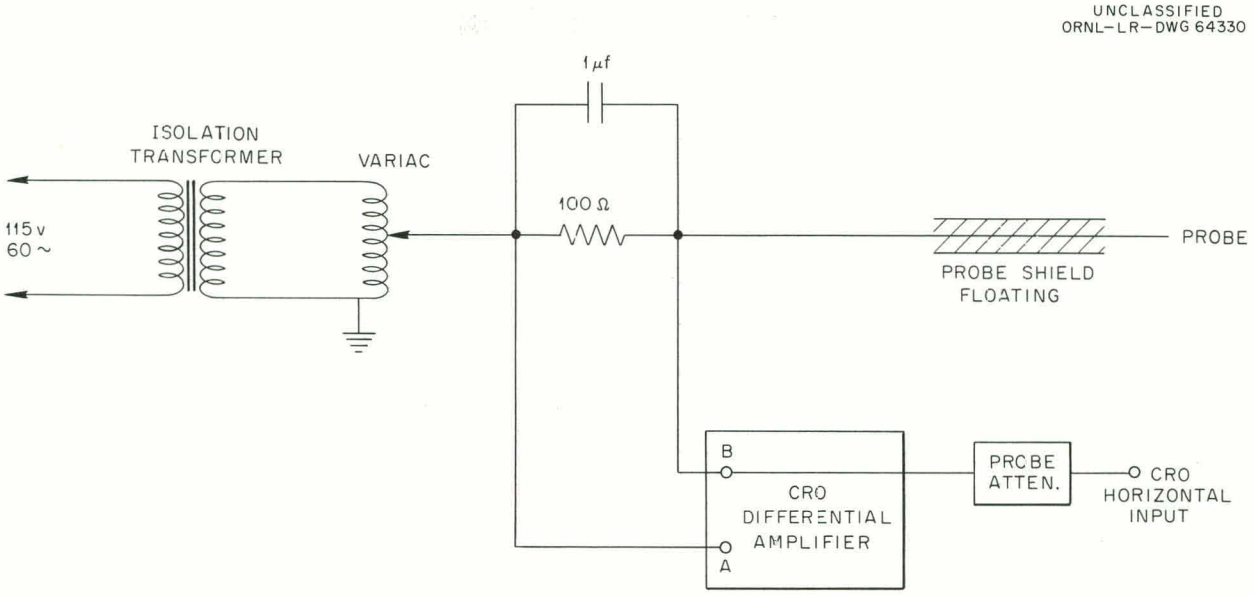

Fig. 4.13. Circuit Used to Obtain Probe Characteristics.

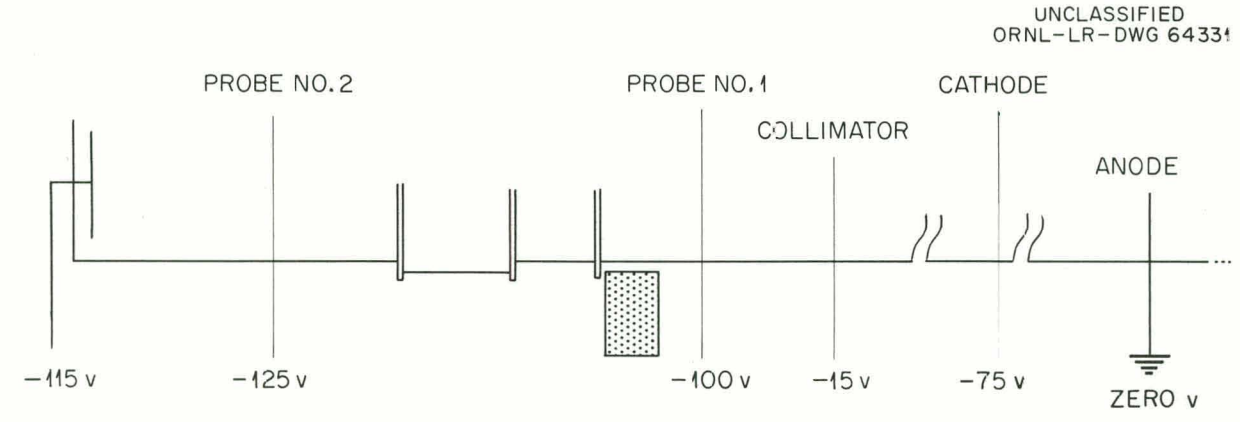

Fig. 4.14. Floating Potentials Measured Along a Collimated Backstream.

the tank walls as a result of the decreased field strength.

The majority of the measurements have been made in the central negative region, where, on occasion, floating potentials as much as 50% greater than cathode potential have been observed. These high values can usually be found with both probes if the backstream is collimated, and sometimes can be found at probe No. 1 without collimation. Figure 4.14 illustrates one set of potentials measured along a collimated backstream. Floating potential profiles taken at the two probes during this same run are shown in Fig. 4.15. When collimated, this high negative region appears as a pale blue stream, apparently emanating from the cathode.

When translated to a semilog plot the probe characteristics generally yield good linear regions, indicating a Maxwellian distribution of the electron thermal velocities. Peak electron temperatures of 10 to 12 v are common at probe No. 1, with occasional extremes of 20 to 24 v. These extremes are often found when the backstream is collimated. The electron temperatures at probe No. 2 are

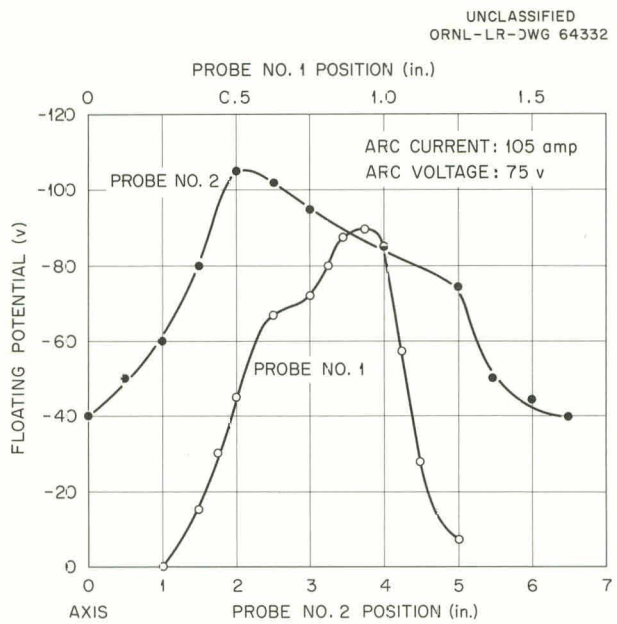

Fig. 4.15. Floating-Potential Profiles in a Collimated Backstream (Relative Position Not Significant).

usually from 1 to 3 v lower than those at probe No. 1.

Maximum electron densities measured at either probe vary by as much as a factor of 2 from one run to the next, or during the same run if the arc changes. The peak densities at probe No. 1 are usually of the order of from 1 to 2×10^{11}. At probe No. 2 they are about 1 to 2×10^{10}.

The electron densities were calculated using the equation

$$n_e = \frac{I}{eA}\sqrt{\frac{m_e}{2eV}},$$

where I is the apparent electron saturation current, A is the effective area of the probe (taken as the length $\times$ diameter), and V is the electron temperature in volts.

Probe characteristics typical of those taken at the two probes are shown in Fig. 4.16. The arc currents and voltages given on the figures indicate the average values over the period of the measurements.

Several attempts were made to obtain measurements in the arc between the cathode and anode. In each case either the probe was melted or the arc was sufficiently disturbed to cause low-frequency

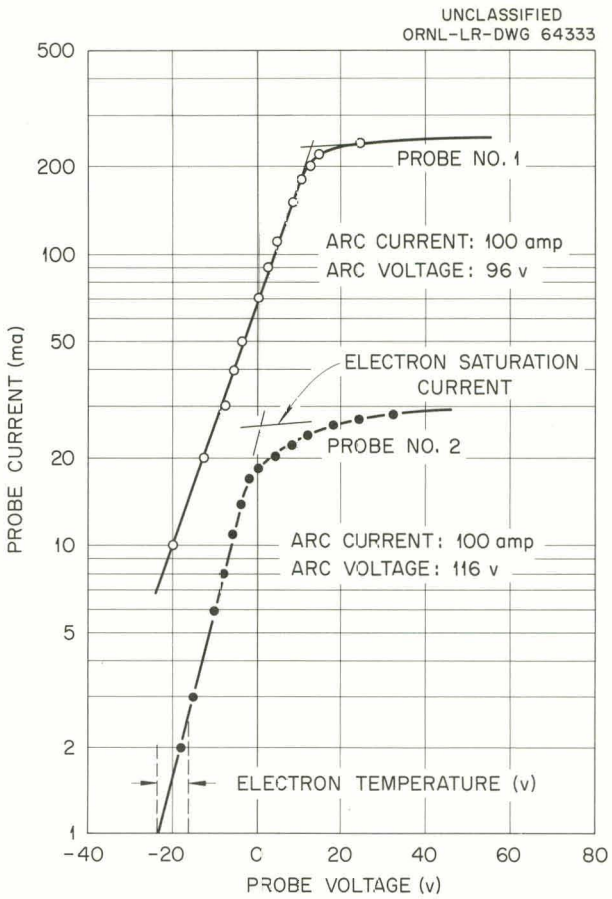

Fig. 4.16. Typical Probe Characteristics.

oscillations in the arc current and voltage. No significant data were obtained.

A new type of cathode construction has been adopted. This construction consists of depositing 0.040 in. of tungsten with a plasma jet over 0.015-in. tantalum tubing of the desired diameter. Cathodes made this way have a more uniform erosion and increased life.

4.2.2 Spectroscopic Studies of the Magnetically Confined Lithium Arc[4]

M. R. Skidmore J. R. McNally, Jr.

Spectroscopic studies have been made of the magnetically confined, high-current, vacuum lithium

[4]We are indebted to J. E. Francis and P. M. Jenkins who were responsible for the operation of the Solenoid Facility in which these studies were made.

arc in the 120-in. solenoid.[5] Numerous impurity lines of carbon, oxygen, and especially nitrogen have been positively identified in the vacuum, ultraviolet, and visible spectrum. Although the Li^+ spectra are more intense than the impurity lines in the visible and ultraviolet, the converse is generally true in the vacuum ultraviolet where the resonance lines of the impurities (~10–20-ev excitation) are much more readily detected than the Li^+ lines involving high-excitation states (~70 ev). The resonance line of Li^+ at λ199 (E.P. = 62 ev) is not detected because our Seya vacuum spectrometer[6] has never revealed any sensitivity below 300 A. Spectral lines of electrode materials are also observed.

The relative degree of ionization of these impurity lines appears somewhat lower than in the carbon arcs previously studied[7] when lines of O^{5+} and N^{4+} were observed frequently. Lines of singly, doubly, and triply ionized (and, infrequently, quadruply ionized nitrogen) impurity species are generally observed in the lithium arc, with doubly or triply ionized nitrogen usually being the most prominent impurity. This relatively lower degree of ionization suggests that the mean electron energy in the lithium arc may be somewhat lower than that previously determined for the carbon arc (3–6 ev). The theoretical expectations for lithium ion abundances at various assumed temperatures and for an assumed electron density of 10^{14} are given in Table 4.1. The Li^{2+}/Li^+ ratios observed mass spectrometrically are frequently about 1:1, suggesting the mean electron energy may be about 3.5 ev on a model based on thermodynamic equilibrium. The mass spectrometric observation on occasion of some Li^{3+} could be due to runaway electrons since 122.4 ev is required for ionization of Li^{2+} and the arc drop is usually about 100 to 150 v. An electron temperature of about 6 ev would permit a sufficiently high population of Li^{3+} to be observed mass spectrometrically if true thermodynamic equilibrium existed.

No Li^{2+} spectral lines have been observed except possibly λ729 (E.P. = 109 ev) which may have been detected on one occasion. The Li^{2+} line group at 4499 A (E.P. = 117.5 ev) has definitely not been observed. It is probable that the blue color of the arc (sometimes ascribed to this 4499-A group) is due to impurity effects.

Table 4.1. Theoretical (Saha Abundance) Ratios of Lithium Ions in a Lithium Arc at $n_e = 10^{14}$ cm^{-3} for Various Electron Temperatures

T_e (ev)	$n_{Li^{2+}}/n_{Li^+}$	$n_{Li^{3+}}/n_{Li^{2+}}$
3	7×10^{-3}	3×10^{-10}
3.5	0.3	1×10^{-7}
4	6	1×10^{-5}
6	6×10^{2}	0.6
10	2×10^{6}	5×10^{3}

Oscillator strengths for numerous lines of Li^+, N^+, and N^{2+} were calculated by the method of Bates and Damgaard.[8] Excitation temperature measurements in the main lithium arc column were then evaluated assuming a Boltzmann distribution and theoretical oscillator strengths using the relation

$$I = \frac{\text{const } fg}{\lambda^3} \exp(-E_i/KT) .$$

The data are plotted in the usual manner, log $(I\lambda^3/fg)$ vs E_i, and the slope of the best straight line characterizes an excitation temperature for the electrons (see Fig. 4.17). The excitation temperature so determined from Li^+ lines was 16,000°K and usually repeated within ±1000°K from day to day. The excitation temperature in the backstreaming region past the cathode ranged from 11,000 to 15,000°K. Impurities in the backstream were found to be mainly W^+, Ta^+, Cu^+, Cu^0, and Ca^+. Nitrogen gas which leaked in through the anode assembly gave values of 50,000°K from lines of N^+ and 23,000°K from lines of N^{2+}, but large uncertainties enter into these two evaluations because of the point spread due to the small range

[5] J. E. Francis *et al.*, *Thermonuclear Div. Semiann. Progr. Rept. Jan. 31, 1961*, ORNL-3104, p 49.

[6] G. K. Werner *et al.*, *Thermonuclear Project Semiann. Rept. Jan. 31, 1959*, ORNL-2693, p 94.

[7] M. R. Skidmore, J. R. McNally, and G. K. Werner, *Thermonuclear Project Semiann. Rept. Jan. 31, 1960*, ORNL-2926, p 38.

[8] D. R. Bates and A. Damgaard, *Phil. Trans.* **242**, 101 (1949).

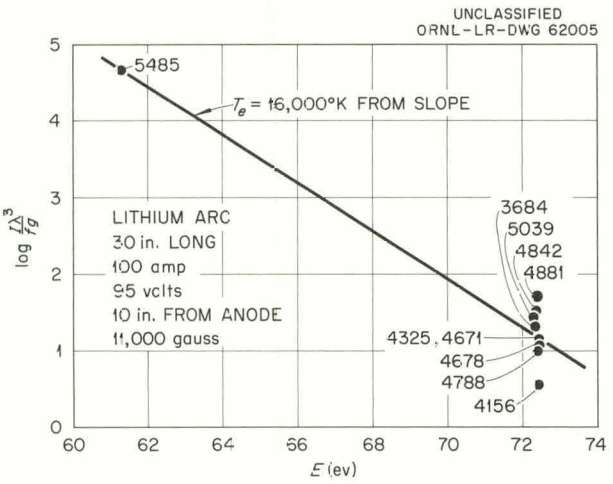

Fig. 4.17. Evaluation of Excitation Temperature of Lithium Arc.

of E_i for these lines. These excitation temperatures, which presumably are a measure of the mean electron energy, disagree with Langmuir probe measurements which give about 150,000°K for the main arc column of a 100-amp, 36-in.-long arc.[9]

It seems likely that true thermodynamic equilibrium of the electrons does not exist in these arcs. Electrons of at least 59 ev are required to populate the lower metastable $1s2s(^3S)$ level of Li^+ (see Fig. 4.18), following which electrons of about 2 ev can readily excite the $1s2s(^3P)$ level with intense radiation of the green line, λ5485 A. The precipitous change in relative population, as measured by $I\lambda^3/fg$, of the $1s4l$ states at about 72 ev compared to $1s2p(^3P)$ at 61 ev, suggests either that single-collision excitation of Li^+ involves 1000 times as many electrons in the energy range 59–71 as in the range above 72 ev or that, more likely, there is a low-density, high-energy class of electrons (primary electrons) and a high-density, low-energy electron class (secondary electrons). Additional support for this latter possibility appears in the observation that the impurity lines in the vacuum ultraviolet are more intense than the Li^+ lines involving transitions between $1s3l$ states and $1s2l$ states. The impurity lines require 10–20 ev for excitation. Collisional depopulation of the metastable ^3S state in collisions between two Li^+ metastables can lead to replenishment of electrons at about 42-ev energy, that is, $2\,Li^{+*} \rightarrow Li^+$ (ground state) $+ Li^{2+} + e$. Thus, it is quite probable that the mean electron energy is quite low (1½ to 5 ev) but that there are sufficient high-energy electrons to keep the metastable ^3P level well populated. The $1s2s(^1S_0)$ Li^+ level is quasi-metastable inasmuch as excitation to $1s2p(^1P_1)$ permits a ready means of depopulating the $^1S^*$ level by de-excitation of $^1P_1$ to the ground state $1s^2(^1S_0)$. The transition probability of λ199 is about 4×10^{10} sec^{-1} (see Table 4.2).

Drifts of Li^+ ions in the arc have been studied with a large (3.3 m) Ebert spectrograph (see Fig. 4.19). Comparisons of anode-to-cathode and cathode-to-anode observations with transverse views of the arc give significant axial ion drifts but much less than previously reported.[5] The first measured Doppler shifts for the λ4671 A of Li^+ were found to be 0.14 A to the blue for the cathode-to-anode view and 0.19-A shift to the red for the anode-to-cathode view. Subsequent, more accurate, measurements on the anode-to-cathode view gave $\Delta\lambda$ = 0.153, 0.160, and 0.154 A red shift for the lines 4671, 4678, and 4326, respectively (one run with no cooling on the anode gave only 0.042-A shift). These correspond to axial ionic drift velocities of approximately 10^6 cm/sec toward the cathode for Li^+ ions in the main arc column. Li^+ ions have also been observed to backstream past the cathode with drift velocities ranging from 0.95×10^6 to 1.7×10^6 cm/sec.

Li^+ spectrum line broadenings were observed at the midpoint of a 72-in.-long lithium arc using a 3.3-m plane grating Ebert spectrograph. The dispersion of this instrument was 0.4 A/mm in the twelfth order. Ion "temperatures" were quite low (94,000°K from λ4325 A, 96,000°K from λ4671, and 144,000°K from λ4678 A). No corrections for Zeeman, hyperfine, or isotope broadening were introduced (λ4678 A showed a definite tail on the long wavelength side) and hence these temperatures represent upper limits for this particular arc run. The strong 5485-A Li^+ line is too broad (~2.5-A width from fine, hyperfine, and isotope structure) to be used for line profile studies. Operating conditions for the arc were 70 amp and 175 v at approximately 2×10^{-6} mm Hg midtank pressure and 8000-gauss field.

The slant effect (see transverse view, Fig. 4.19) in λ4671 A gave 0.17 A for the total shift (top to

[9] P. J. Dickerman, Laboratories for Applied Science, University of Chicago, *Progr. Rept.* LAS-L-P181-17 (June 1961).

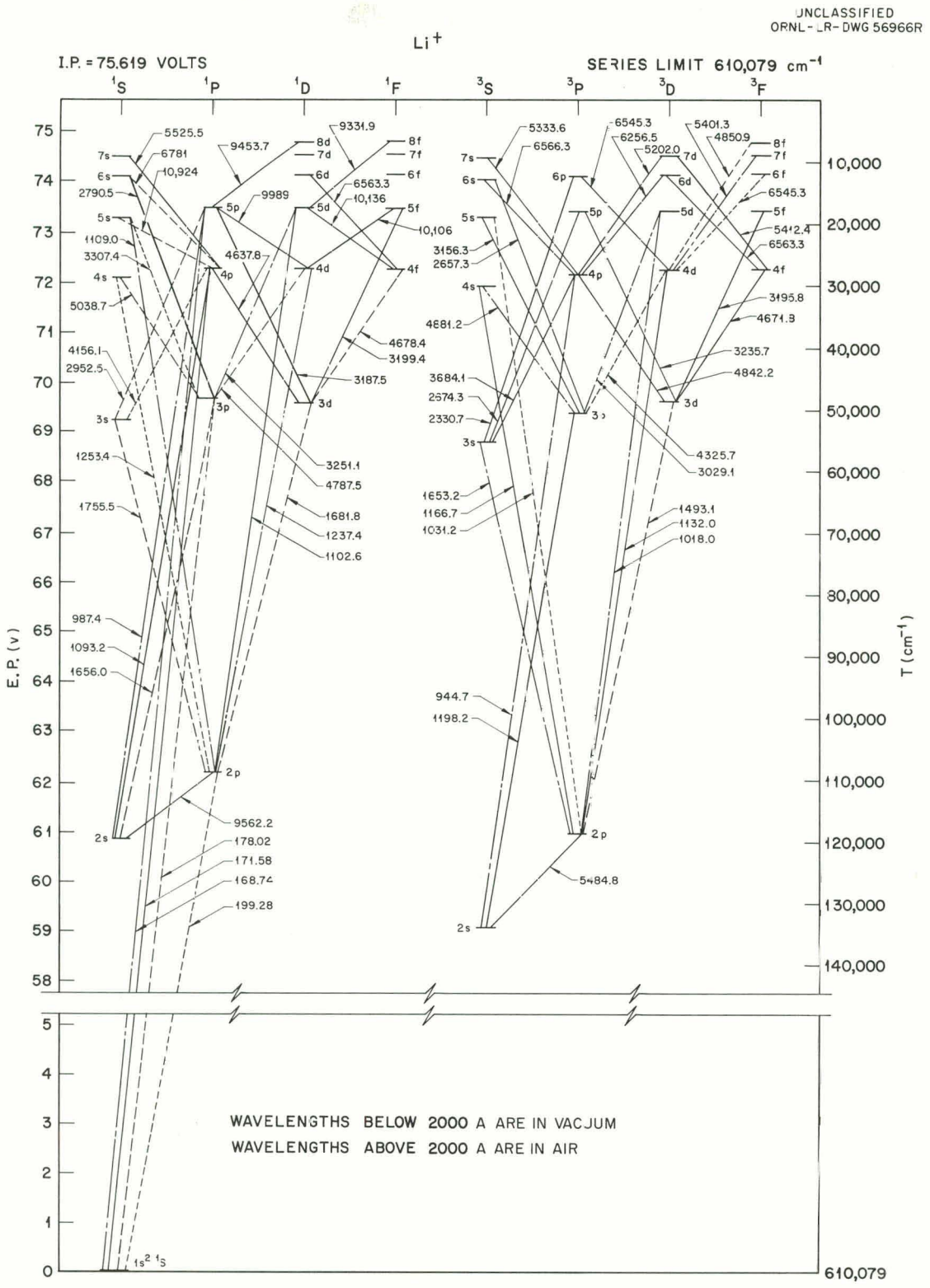

Fig. 4.18. Grotrian Diagram for Li^{+}.

Table 4.2. Transition Probabilities and fg Values for Li^+ Lines

λ (A)	Transition	A (sec^{-1})	fg	E_{upper} (ev)
199	$1s^2(^1S) - 1s2p(^1P^0)$	3.9×10^{10}	0.70	62.20
5485	$1s2s(^3S) - 1s2p(^3P^0)$	2.3×10^{7}	0.92	61.27
4881	$1s3p(^3P^0) - 1s4s(^3S)$	7.2×10^{7}	0.77	71.89
4842	$1s3d(^3D) - 1s4p(^3P^0)$	9.4×10^{6}	0.30	72.13
5039	$1s3p(^1P^0) - 1s4s(^1S)$	5.4×10^{7}	0.21	72.09
3684	$1s3s(^3S) - 1s4p(^3P^0)$	3.1×10^{7}	0.57	72.13
4325	$1s3p(^3P^0) - 1s4d(^3D)$	10.9×10^{7}	4.6	72.22
4671	$1s3d(^3D) - 1s4f(^3F^0)$	2.2×10^{8}	15	72.22
4678	$1s3d(^1D) - 1s4f(^1F^0)$	2.2×10^{8}	5.1	72.22
4788	$1s3p(^1P^0) - 1s4d(^1D)$	11.4×10^{7}	2.0	72.22
4156	$1s3s(^1S) - 1s4p(^1P^0)$	3.3×10^{7}	0.26	72.24

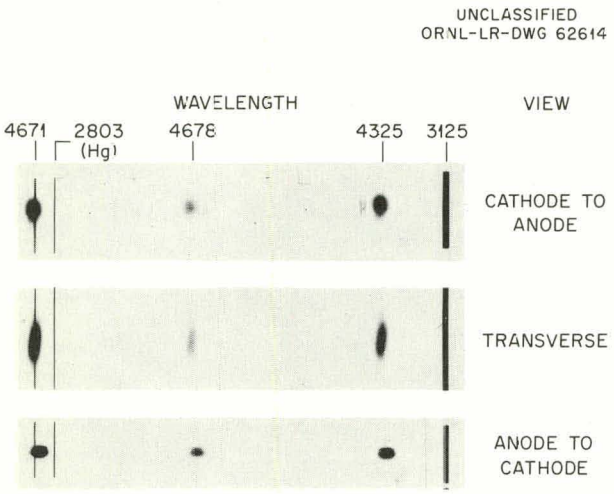

Fig. 4.19. Doppler Broadening, Shifts, and Slants for Cathode-to-Anode, Transverse, and Anode-to-Cathode Views in Long Lithium Arc in 120-in. Solenoid.

bottom of spectral line) or 0.085 A for the Doppler shift corresponding to a Doppler precessional velocity drift of 5.5×10^5 cm/sec approximately 1 cm from the arc center (rotation frequency of 100 kc).

4.3 THE DEUTERIUM ARC

C. L. Cocke, Jr.[10]
R. A. Gibbons
R. J. Mackin, Jr.
W. F. Peed
T. F. Rayburn
W. S. Risk[10]

4.3.1 Introduction

Investigation of the high-vacuum deuterium arc plasma has been oriented toward the measurement of basic properties, intercomparison of measuring techniques, and effects of parameter changes on the properties. The measurements have been predominantly spectroscopic but have been supplemented by Langmuir probes and microwaves. The properties investigated include ion and electron densities and temperatures, current oscillations, and cyclotron radiation. It is concluded that the plasma column is relatively quiescent and stable.

Previous reports[11,12] have included descriptions of the facility used for gas arc work and the details

[10] Summer employee.

[11] J. S. Culver *et al.*, *Thermonuclear Project Semiann. Progr. Rept. July 31, 1960*, ORNL-3011, pp 50–53.

[12] R. A. Gibbons *et al.*, *Thermonuclear Div. Semiann. Progr. Rept. Jan. 31, 1961*, ORNL-3104, pp 58–70.

of arc operation. The majority of the measurements have been made at the center of a 1-m arc in a magnetic field of 7000 gauss with a pressure around the plasma column of 5×10^{-5} mm Hg. The high-density plasma column is a cylindrical shell about 16 mm in diameter and 3 mm thick. In standard arc operation about 120 amp of electrons and 30 amp of ions drifting in opposite directions constitute the plasma.

4.3.2 Density

In the high-density "core" of the plasma, microwave transmission gave a maximum density of about 2×10^{14} electrons/cm^3. This has been verified by spectroscopic measurement of the ion drift velocity (Doppler shift) along the arc (10^6 cm/sec $\rightarrow 1.5 \times 10^{14}$ ions/cm^3) and ion saturation current to a Langmuir probe (15 amp $\rightarrow \sim 3 \times 10^{14}$ ions/cm^3). The core density as inferred from the drift velocity was proportional to the gas input to the anode and was independent of both the arc current (in contrast to the microwave data[12]) and the magnetic field in the normal range of operation.

The density as inferred from drift velocity was approximately constant along the arc though the magnetic field changed by a factor of 2. Figure 4.20 shows the variation of drift velocity and magnetic field along the arc. It was verified that He II ions and C III showed the same drift velocity, and this was taken to be characteristic of all ions.

The density according to probe data dropped off radially from the core approximately as r^{-2} out to the point at which the plasma intercepted the pressure baffles. The radial decrease was roughly exponential over 3 orders of magnitude, with an e-folding distance of 0.25 in.

4.3.3 Ion Temperature

Earlier measurements of the ion temperature have been checked and extended to include effects of variations in several parameters. Doppler broadening of impurity-ion spectral lines was determined using both the 0.5-m Jarrel-Ash 82000 scanning spectrometer and the 2-m Bausch and Lomb echelle spectrograph. Under "standard operating conditions" (I = 150 amp, Q = 4 cm^3 D_2 per sec) the indicated temperatures of C III agreed to better than 10% with the published value,[12] 16 ev. The ion temperature was verified as being independent of mass and charge, and unaffected by the normal impurity level.

A contradiction was found in data bearing on the effects of varying arc current. Between 100 and 220 amp, the echelle indicated no detectable temperature variation. However, the data obtained with the Jarrel-Ash instrument showed a linear dependence on current over a range from 11 to 22 ev. Plotted against electron current (i.e., total current minus the deuteron current corresponding to the input gas flow) the apparent temperature is independent of gas flow and varies as

$$T_e = 7 + 0.08\, I_e \text{ (amp, ev)}.$$

The source of the discrepancy is not known.

Ion temperature measurements at ion drift distances of 60 and 110 cm (60- and 110-μsec heating times) in the GAF (Gas Arc Facility) indicated no change in the temperature. Later measurements in the 3-m Solenoid Facility over a drift distance of 40 to 220 cm indicated appreciable ion heating from 14 to 25 ev, and gave the same temperature at 60 cm as the GAF measurements. The high pressure (5×10^{-4}) at the 110-cm point in the GAF and the proximity of the cathode ($\sim$5 cm) may explain the disagreement.

Impurities were introduced into the arc to check the ion temperature dependence on impurity concentration. Three atomic per cent of carbon reduced the ion temperature 25% and the reduction was proportional to impurity concentration. At the background impurity level previously reported,[12] that is, 0.1%, the ion temperature would be reduced about 1%.

4.3.4 Electron Temperature

Electron temperatures have been estimated from the relative intensities of two neutral helium lines and reported previously.[12] Langmuir probe measurements of the high-energy tail of the electron energy distribution indicate the distribution is exponential there as expected from calculations which predicted a Maxwellian distribution. The electron temperature of the core was 40 $\pm$ 10 ev as compared to 60–70 ev estimated from the helium lines. The probe measurements of electron temperature as a function of radius indicated a very marked drop at the edge of the core to 5–10 ev in the "halo" region just outside the core, dropping more slowly to 2–3 ev several centimeters away. The probe visibly perturbed the plasma but the ion density measurement was in good agreement with independent values. The radial dependence of the

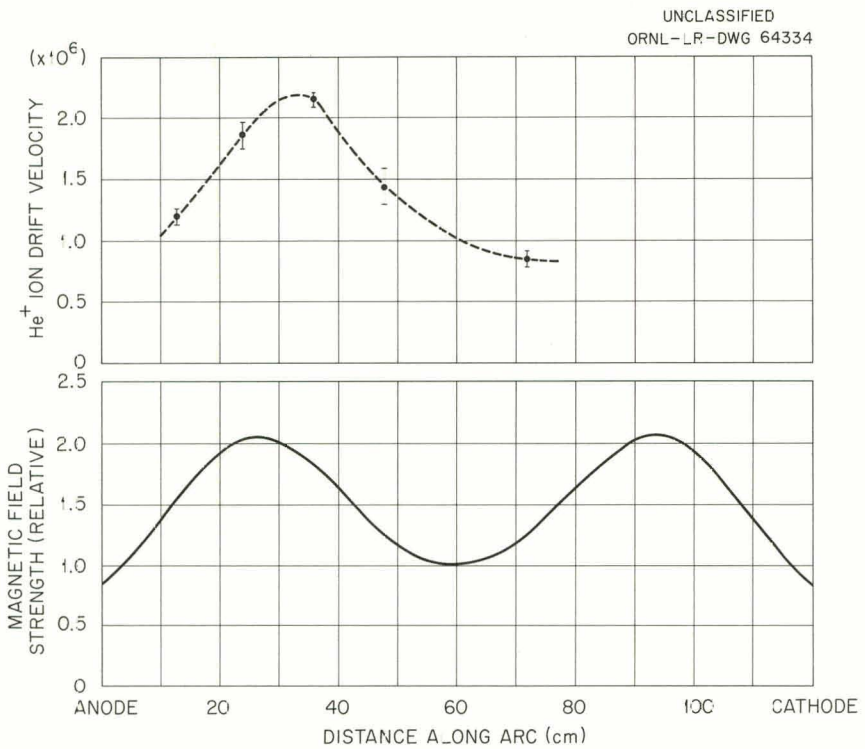

Fig. 4.20. Helium Ion Drift Velocity Calculated from Doppler Shift.

helium ratio was much more gradual, indicating the existence of a substantial density effect and (at low densities) a large overestimate of T_e.

4.3.5 Noise

No thorough study of noise and oscillations has been made. Several scattered observations are presented because of their implications regarding plasma turbulence. Noise has been observed with the Neidigh mass analyzer, an rf loop-antenna probe, and a resistance in the arc current lead. The mass analyzer (displayed on an oscilloscope) revealed pulses with a frequency of 370 kc ± 20% and an exponential damping time constant of 4.3 μsec (1.6 cycles ± 10%). The rf probe and a frequency analyzer revealed a peak at 320 kc. The arc current had pulses similar to those of the mass analyzer but with a time constant of 13 μsec and a repetition rate of 1 pulse per 5 sec. The peak-to-peak noise level of the current was less than 2% (measured across 0.0015 ohm).

4.3.6 Cyclotron Radiation

The rf probe and frequency analyzer were used to search for fields varying at the deuteron cyclotron frequency, f_{ic}. The probe was located in the midplane of the GAF, and a signal was found which was strongest for the plane of the loop lying parallel to the arc. The resonant peak observed, however, was not the f_{ic} of the central magnetic field but $2f_{ic}$. It had the same field and mass (D_2 vs H_2) dependence as a cyclotron frequency. This signal could have been a second harmonic of f_{ic} from the center field or f_{ic} from the field at the mirror.

A deuterium arc was run in the 120-in. Solenoid Facility to check this point. Neither f_{ic} nor $2f_{ic}$ were observed as peaks. However, dips in the noise spectrum were observed at both f_{ic} and $2f_{ic}$. At present no explanation is offered for the observations.

Radiated microwave noise at two electron cyclotron frequencies, f_{ec} = 11.7 and 23.4 kMc (in the appropriate magnetic fields), was used to estimate

the plasma electron temperature, on the assumption that the plasma radiates as a black body at f_{ec}. The measured "antenna temperature" varied from a fraction of an ev to 5 ev. Because of plasma self-absorption, the radiation must come from regions where $f_{ec} \geq f_{plasma}$, corresponding to a density of 7×10^{12} cm^{-3} for the 23.4-kMc case. This corresponds to an arc surface at a radius of 1.9 cm, which would give a free-space antenna factor close to 1. The results are then in reasonable agreement with the Langmuir probe results, which indicate a temperature of only a few electron volts in this region.

We are indebted to Herman Postma for motivating and participating in the radio-frequency measurements and to W. B. Ard for the microwave measurements.

4.3.7 Plasma Rotation

The echelle spectrograph was used to measure the line "slant" produced by rotation of the plasma column. Lines of the Balmer series indicated no slant ($v_\theta < 4 \times 10^4$ cm/sec), in keeping with the previous explanation[12] of their source, that is, excitation of the background gas. Lines of the 4650 group of C III had a slant corresponding to a velocity of 1×10^5 cm/sec at 1 cm or a rotational rate of 1.6×10^4 rps. This rotation was in a direction corresponding to an E field of 7 v/cm directed radially inward. Such a field is expected to exist at a plasma boundary in a magnetic field as a result of the Larmor radius of the deuteron being larger than that of the electron at a comparable energy. The field strength is an order of magnitude less than usually reported for carbon arcs, consistent with the relative weakness of noise generation by the D-arc and the corresponding implication that it is a quiescent plasma.

4.3.8 Gas Accountability Experiments

The high pressure in the central region of the GAF during operation with gas arcs has been a continuing obstacle to its employment in a DCX device. Earlier results indicated that between 30 and 40% of the pressure could be accounted for by leakage from the cathode and anode ends of the facility. The source of the remaining pressure is still unaccounted for. The present experiment was undertaken in order to determine whether recombination of D_2^+ molecular ions was contributing to this pressure. The central idea was to compare measurements of the fractional inleakage from the ends for hydrogen and deuterium arcs with that for a helium arc, for which no molecular ions would be expected. If molecular ions were the dominant gas source for the H_2 and D_2 arcs, the experiments should show about 100% accountability in terms of inleakage for the helium arc.

The experiment consisted of raising the end pressures separately by about 20%. The rise in pressure of the central region was noted and a linear extrapolation applied to determine what increase would occur in the central region if the anode or cathode end pressure were increased 100%. This amount was taken to be equal to the present influx.

The above procedure was applied to D_2, H_2, and He arcs for normal positions of anode and cathode. In addition, data were taken with the cathode retracted 2.5 and 5 cm and the anode retracted 5 and 10 cm. In the analysis, allowance was made for the effect of raising one end-region pressure on the pressure of the other end region.

The results showed no significant systematic variation with the gas used, its rate of flow, or the electrode position. The end-leakage contribution to central pressure ranged between 30 and 50% for all three gases, the variations not discernibly correlated with any particular parameter. Since He molecular ions are expected to be many times less frequently formed than those of H_2 or D_2, it is concluded that molecular ions do not contribute a significant fraction of the observed central-region pressure. Since diffusion to the walls is contraindicated by the weakness of the dependence of pressure upon magnetic field, the number of remaining possibilities is somewhat limited.

4.4 LOW-DENSITY ARC EXPERIMENT

C. W. Blue
H. C. Hoy
R. L. Knight
O. D. Matlock
V. J. Meece
W. L. Stirling

The plasma stream from the electron gun shown in Fig. 4.21 is being investigated for use as a breakup mechanism for DCX. An arc is established between the tantalum filament and hollow carbon anode. The arc plasma thus formed is confined to move axially along the magnetic field (not shown).

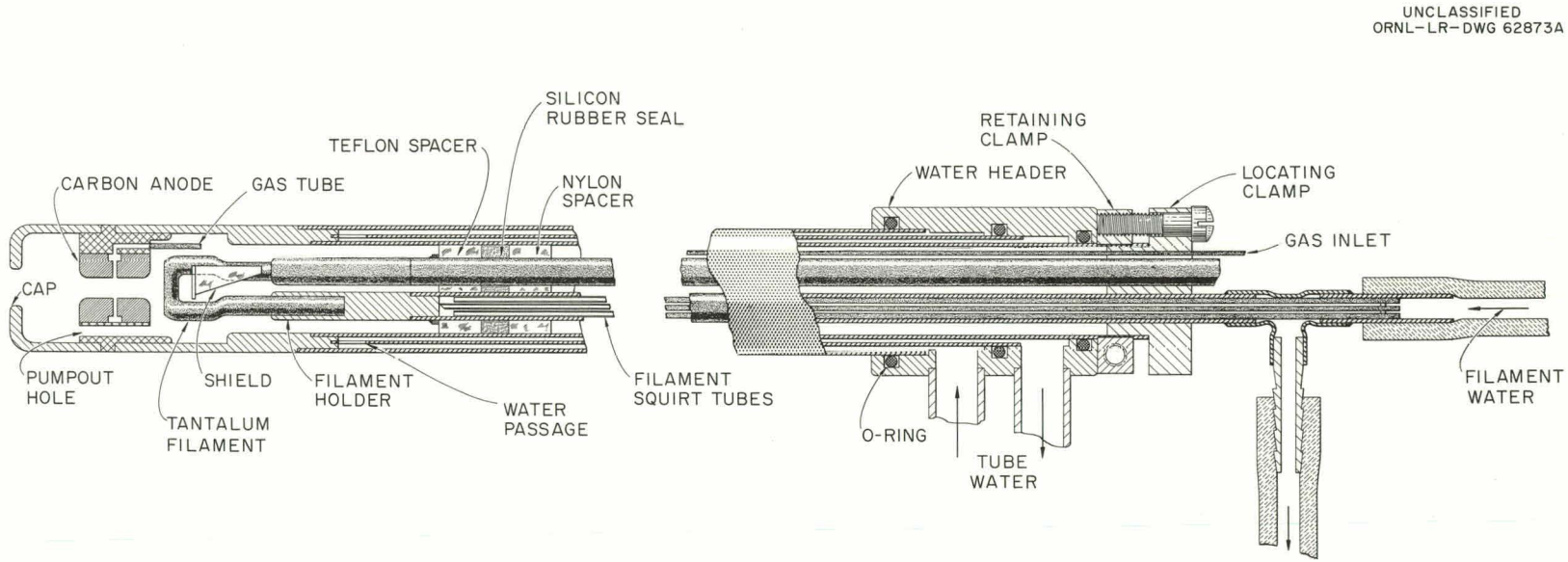

Fig. 4.21. Electron Gun for Low-Density Vacuum Arc.

Figure 4.22 shows schematically the components being assembled in DCX-EPA to measure (1) the plasma density and (2) the effect on the pressure in a high-vacuum inner liner caused by the presence of the plasma stream.

Density measurements of hydrogen plasma have been made with probe No. 1 without the inner liner installed; measurements have been made on argon gas with both probes Nos. 1 and 2 without the inner liner installed. The density was measured by shorting the electron arc voltage and simultaneously sweeping the ions out to the negatively biased probe. The decaying ion current produced a similar voltage signal across the probe load resistor. An oscilloscope was used to record the signal trace; the latter was integrated to determine the total number of ions in the column. The argon ions were assumed to be singly ionized.

Densities for both the argon and hydrogen plasmas were measured to be between 1×10^{11} ions/cm^3 and 3×10^{11} ions/cm^3. The background neutral density also lies within this same range. The background pressure was increased by a factor of 65 to see if the plasma column was being fed peripherally from the neutral gas rather than longitudinally from the arc as assumed. The plasma density increased only by a factor of 4.

A background pressure between 5×10^{-9} mm Hg and 1×10^{-8} mm Hg in the inner liner of Fig. 4.22 should be obtainable. The neutral density will then be a factor of 100 less than the measured plasma densities. Measurements of the inner liner pressure variations with and without the plasma stream will determine the usefulness of the plasma for the dissociation of molecular ions in the DCX experiments.

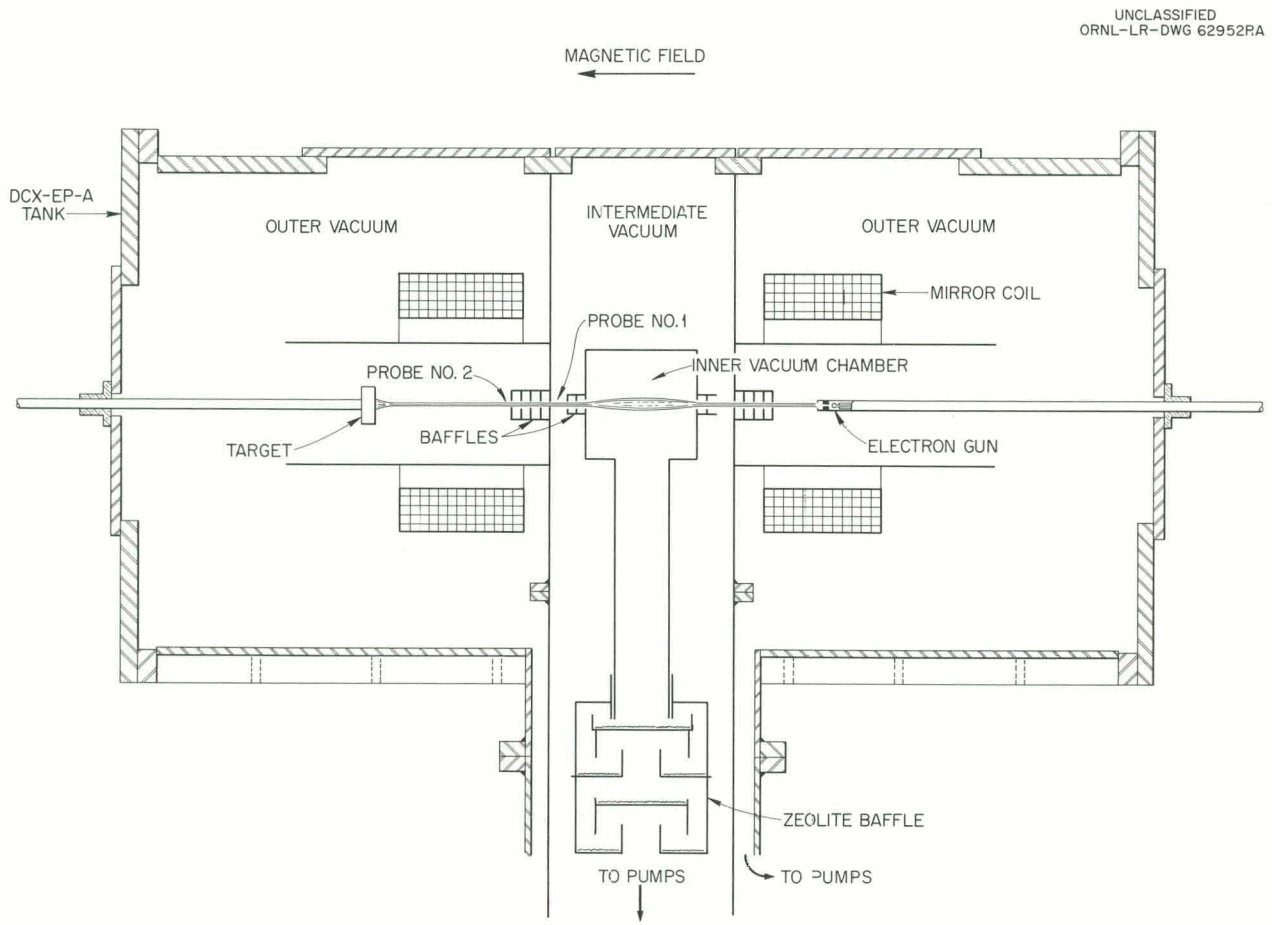

Fig. 4.22. Low-Density Arc Experiment.

5. Ion Production, Acceleration, and Injection

5.1 HIGH-CURRENT ACCELERATOR AND NEUTRALIZED BEAM FOR DCX-2

R. C. Davis
R. R. Hall
G. G. Kelley
E. C. Moore
O. B. Morgan
R. F. Stratton

The work previously reported[1] on the injector system for DCX-2 has been continued. The accelerator tube support has been raised and the cylindrical tank installed as planned. See Fig. 5.1.

It is still not possible to operate the tube in air at full voltage. An atmosphere of Freon and nitrogen is provided, contained by a plastic bag surrounding the tube. This system is not as convenient as would be desirable. Occasional external breakdowns punch holes in the bag. These must be patched promptly. Several ideas for improvement are being explored. To test one possible approach a section is being built with deep radial fins. Such an arrangement is used successfully at Argonne National Laboratory.

Total beam path length from lens to target is about 120 in. Probes may be swept through the beam at distances of 47, 66, and 85 in. below the center of the lens. The beam profile can be determined from oscillograph pictures of current vs probe position.

In this apparatus the accelerator tube has held up to 700 kv with no current, 100 ma at 650 kv, and 215 ma at 600 kv. The upper current limit is reached when the increasing x-ray production finally is sufficient to cause external breakdown.

With the original electrodes voltage cleanup was a long, slow process. Recently, the importance of minimizing the amount of electrode surface at high field has become apparent and, in addition, it has been found that the shielding of insulator walls from the beam can be less thorough than had been thought. On the basis of these considerations new electrodes have been designed. These electrodes can be cleaned up to 600 kv in less than 10 min after reassembly and pumpdown. They also have eliminated difficulty due to electron trapping and incipient breakdown from the magnetic field of the solenoid lens. See Fig. 5.2.

Very recently these new electrodes have been modified to include lead shielding to reduce the external x-ray field. The tube has not been run at high current since this modification. Still to be tried is a low-Z target for returning electrons.

Beam profile measurements with the old electrodes were extrapolated to the center of the lens and showed there a beam diameter of 3.7 in. at 180 ma and 600 kv. The variation of diameter as a function of current appeared to be even less than with the square root of the current. If this behavior continues to higher current it should be possible to pass at least 400 ma through the lens. Since the new electrodes accelerate the beam more rapidly the performance now should be even more favorable.

The beam in the field-free region below the lens is self-space-charge-neutralized even at the lowest pressure attainable, which with the beam on is about 3×10^{-6} mm Hg. An accurate measurement of beam quality has not been made because of difficulty in interpreting the probe signals. Visual observation of a crossover in the vacuum 5 to 6 ft below the lens indicates that the minimum beam diameter of any component is at least as small as 0.5 in. at 180 ma total current. There is an uncertainty, however, which could work either way due to the fact that the beam is scattered violently just below what appears to be the crossover. The reason for this scattering has not been determined.

[1] *Thermonuclear Div. Semiann. Progr. Rept. Jan. 31, 1961*, ORNL-3104, p 19.

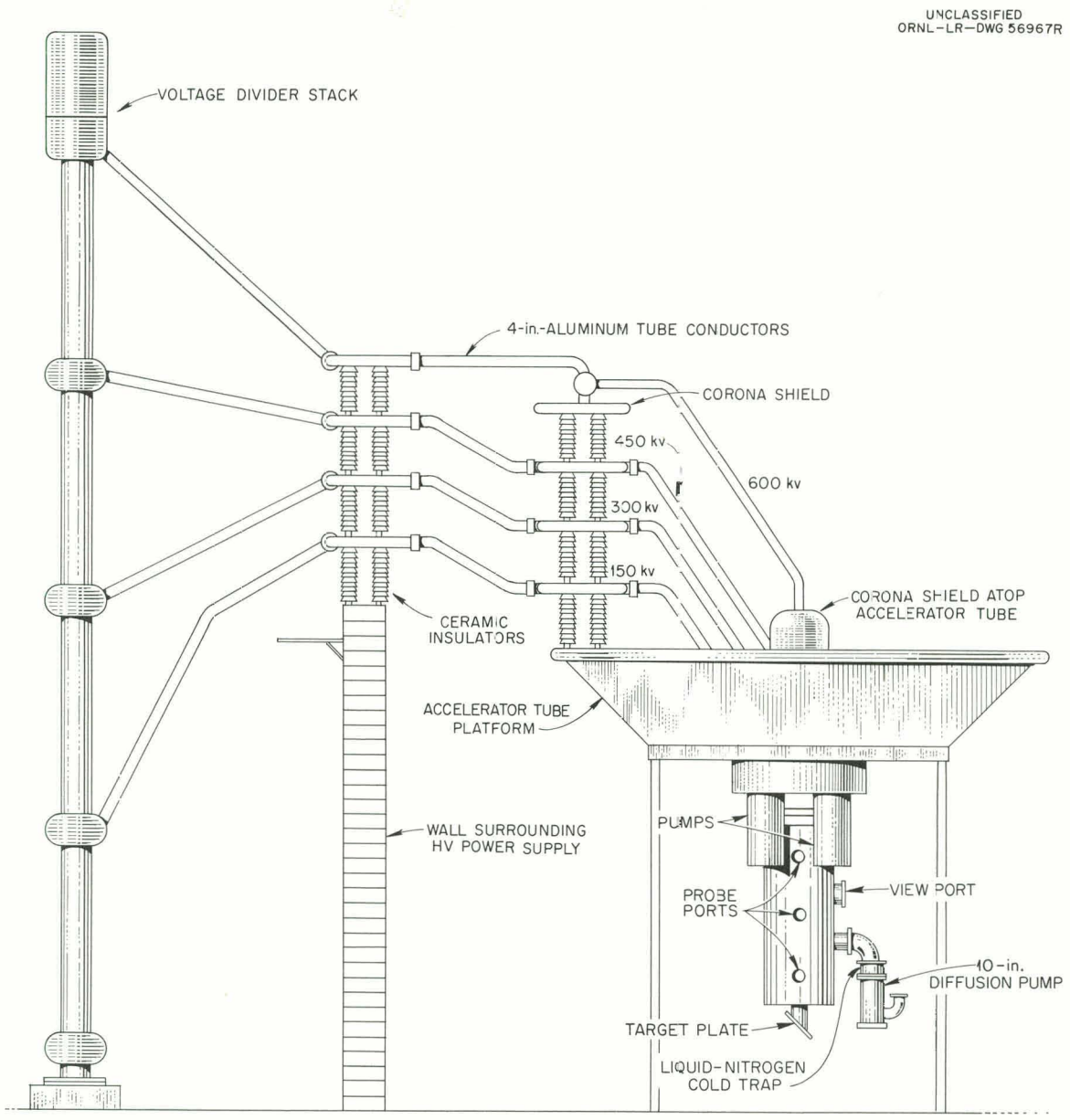

Fig. 5.1. Injector System for DCX-2.

Automatic space-charge neutralization was noticed first in the apparatus used for beam analysis at 100 ma and up to 100 kv. This work was described in a previous report.[2] It was hoped that analysis could be carried out at considerably higher current by the use of a magnetic solenoid lens. The intention was to focus in succession the three mass components on an aperture small enough to exclude most of the other components. This method has not been successful because of the effect of the strong lens field on source performance. The proton component predominates even at low currents.

Measurements made in this apparatus showed that the beam profile was consistent with the expected ion optical paths in the absence of space charge. Current density at a target 50 in. below

[2] O. B. Morgan *et al.*, *Thermonuclear Project Semiann. Progr. Rept. July 31, 1960*, ORNL-3011, pp 57–64.

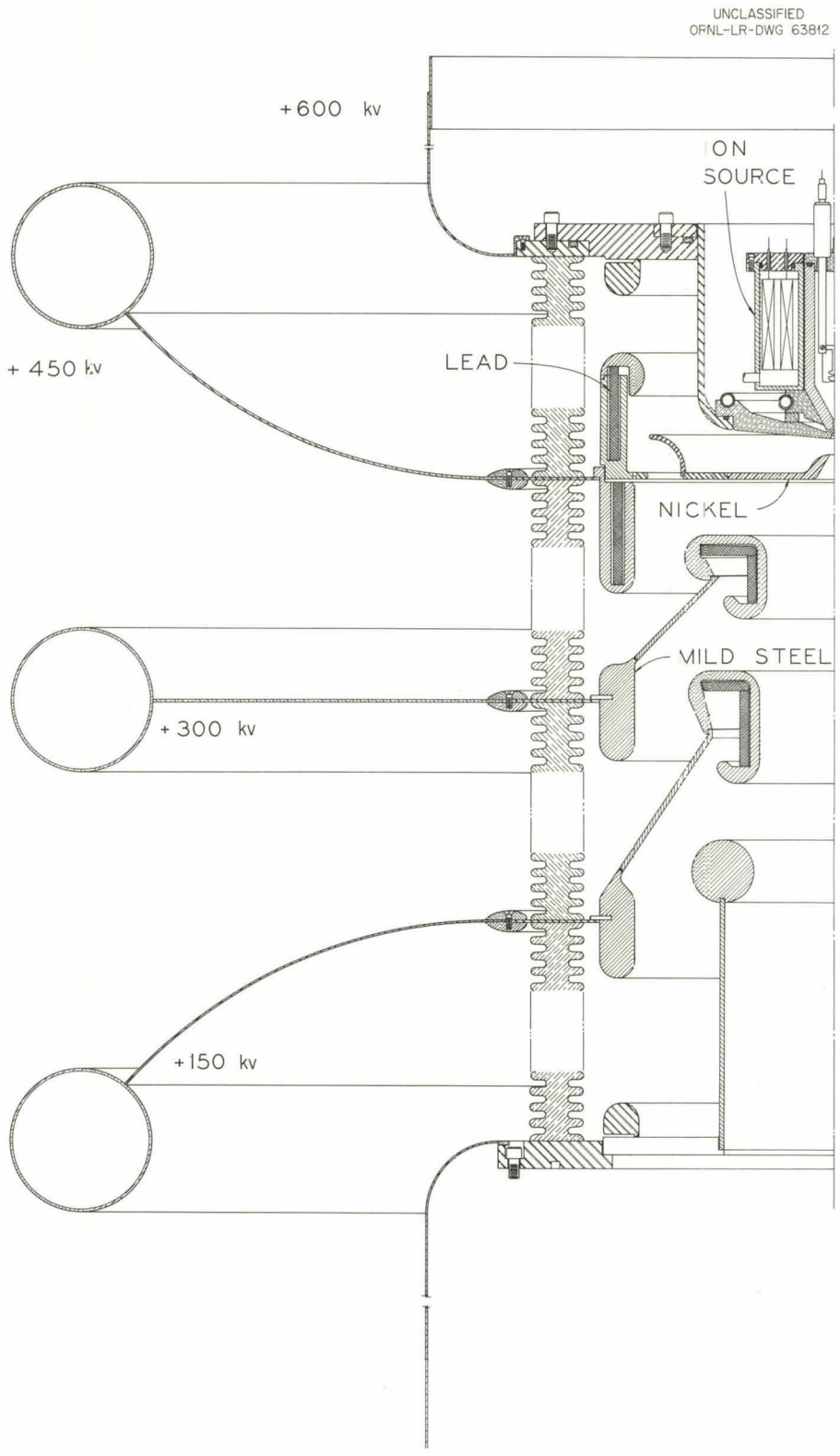

Fig. 5.2. 600-kv Accelerator Tube Mark III.

the lens was 10 times as great as could have been obtained without neutralization. A positive bias on the target destroyed neutralization but it could be restored by a transverse magnetic field near the target. Pressure in the chamber was $(2–3) \times 10^{-6}$ mm Hg.

5.2 COAXIAL INJECTION OF ELECTRONS INTO ION BEAM

C. W. Blue R. L. Knight V. J. Meece
H. C. Hoy O. D. Matlock W. L. Stirling

The experimental model of the neutralized beam injector has been operated with partial success at low acceleration voltages. A schematic view of the assembly is shown in Fig. 5.3.

Further study of the monoenergetic electron stream has been carried out under conditions of improved alignment of the components in the magnetic field. Figure 5.4 shows a typical set of low acceleration voltage (M) curves of target current vs J_2 booster voltage at a tank pressure of 6.5×10^{-6} mm Hg. The decrease of current at all M values below some J_2 value corresponds to an energy loss mechanism, the total loss being equal to the electron-gun arc voltage $J_1 = 260$ v $+ J_2$. The energy loss decreases with increasing electron energy of M voltage.

Figure 5.5 shows two curves at $M = 1$ kv and $M = 7$ kv similar to those of Fig. 5.4 but at a tank pressure equal to 6.6×10^{-5} mm Hg, the same pressure as that existing when the ion source is on. Variations of electron energy as shown in these two figures are consistent with what would be expected from a two-stream or coherent interaction.

Table 5.1 is a tabulation of data taken of the ion source performance (argon ions) with and without electron injection. The last column indicates whether or not the electron gun was on. The column J_2 indicates the amount of extra energy given to the electrons to compensate for energy losses experienced while traversing the high density of secondary plasma in the ion source.

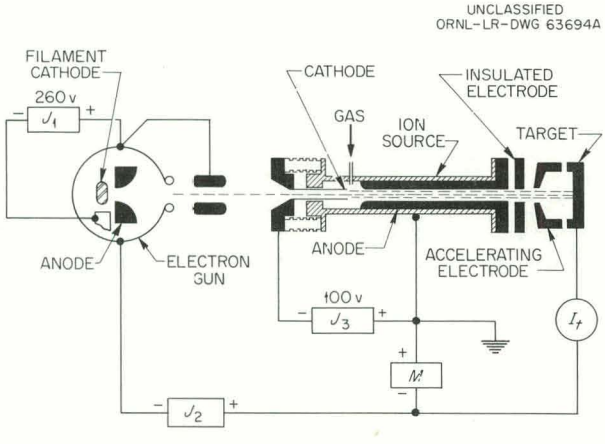

Fig. 5.3. Neutralized Electron-Ion Source.

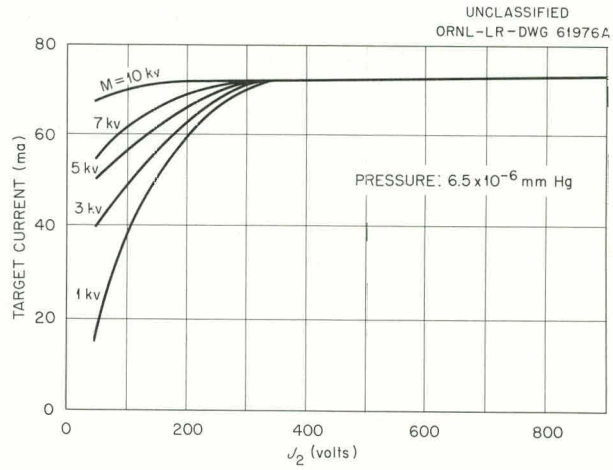

Fig. 5.4. Variation of Electron Current on Target with Accelerating Voltage.

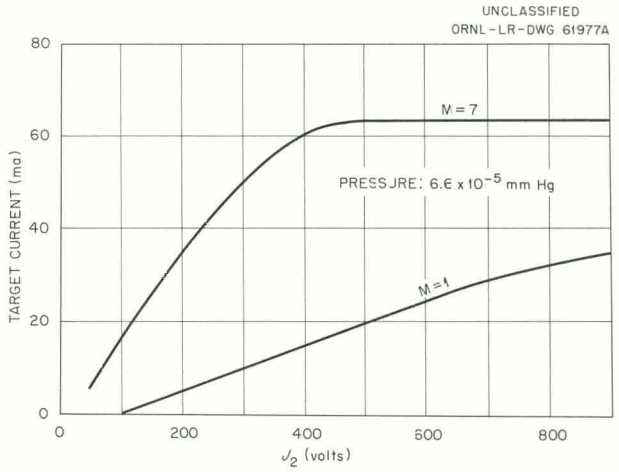

Fig. 5.5. Variation of Electron Current on Target with Accelerating Voltage.

Table 5.1. Effects of Injecting Electrons in the Configuration of Fig. 5.3

Ion-source arc, 18 amp at 100 v; electron-gun arc, 0.3 amp at 260 v; pressure, 6.6×10^{-5} mm Hg

Accelerating Voltage M (kv)	Booster Voltage J_2 (v)	Target		Accelerating Electrode		Electron-Gun Arc Voltage
		Current (ma)	Thermal Power (w)	Current (ma)	Thermal Power (w)	
8	300	10	160	220	1150	Off
1	300	325	360	140	300	On
7	300	400	1790	960	2990	On
8	500	10	30	50	440	Off
1	500	225	250	100	160	On
7	500	650	2320	1200	3200	On

Power measurements on target and accelerating electrode were obtained calorimetrically. The best indication of the effect of the electrons is obtained by comparing the power dissipated at $M = 8$ kv with that at $M = 7$ kv at constant J_2 voltage. For $J_2 =$ 300 v, the power on target is approximately 10 times larger with the electrons ($M = 7$ kv) than without ($M = 8$ kv). The accelerating electrode power went up by a factor of about 2.5. At $J_2 = 500$ v, the power ratios are even higher. It should be pointed out that no attempts have been made yet to utilize the ion optics of the system to best advantage.

The results show that oscillating electrons have been produced and that the effect is to increase ion beam output. It is believed that little neutralization of the ion beam beyond the accelerating region has been achieved as yet.

Assembly of the 100-kev high-energy plasma accelerator[3] on DCX-EP-A is complete. Vacuum checks on the accelerator assembly are completed; electrical and water connections are about 50% completed.

[3] *Thermonuclear Div Semiann. Progr. Rept. Jan. 31, 1961*, ORNL-3104, p 80.

6. Theory and Computation

6.1 FOKKER-PLANCK COEFFICIENTS FOR A PLASMA, INCLUDING CYCLOTRON RADIATION[1]

Albert Simon[2] Norman Rostoker[2]

Kinetic equations for a plasma have previously been obtained by starting with the Liouville equation and making an expansion in powers of the discreteness parameters.[3] To the lowest order in this expansion the Vlasov equations are obtained. In first order a Fokker-Planck equation is obtained where the coefficients come from the time-asymptotic solutions of integro-differential equations for the pair correlation functions.

Solutions have been published previously for an infinite plasma with Coulomb forces,[4] for a plasma with Coulomb forces and a constant magnetic field,[5] and for a plasma with the complete electromagnetic field and no constant magnetic field.[6] The problem has now been treated with both the complete electromagnetic field and a constant magnetic field. The new feature of this problem is the inclusion of the electromagnetic radiation which was absent in all the cases previously treated.

At the outset the system consists of a large number of "bare" particles that interact with each other and a denumerably infinite number of vacuum oscillators. The present statistical treatment leads to a kinetic equation for the one-body function that has a physical interpretation in terms of "dressed" particles and renormalized oscillators. A shield cloud of charge and current density envelopes a particle, and the radiation takes place in terms of oscillators that satisfy the plasma dispersion relation instead of the vacuum dispersion relation.

In the low-density limit, or when $k \gg \omega_p/c$, the result agrees with the vacuum radiation formula employed by Trubnikov.[7] If terms of order $(\omega_p/kc)^2$ are retained, the principal effect is the renormalization of the oscillators. In the exact radiation formula longitudinal and transverse waves are coupled; that is, the normal modes do not have a simple polarization. The virtue of the present treatment is that it indicates the terms that represent electromagnetic radiation and the proper particle dressing under these circumstances.

6.2 A RECALCULATION OF THE TRITIUM BREEDING RATIO IN A FUSION REACTOR BLANKET

W. E. Kinney[8]

6.2.1 Introduction

A means of producing H^3 must be found if the (d,t) reaction is to be the basis of practical thermonuclear power. Spitzer *et al.*[9] have concluded that H^3 breeding is possible by the

---

[1] Abstract of paper submitted to Conference on Plasma Physics and Controlled Nuclear Fusion Research, Salzburg, Austria, September 4–8, 1961.

[2] General Atomic Div., General Dynamics Corp., San Diego, Calif.

[3] N. Rostoker and M. N. Rosenbluth, *Phys. Fluids* 3, 1 (1960); A. Simon and E. G. Harris, *Phys. Fluids* 3, 245 (1960).

[4] A. Lenard, *Ann. Phys.* (*N.Y.*) 10, 390 (1960); R. Balescu, *Phys. Fluids* 3, 52 (1960).

[5] N. Rostoker, *Phys. Fluids* 3, 922 (1960).

[6] A. Simon, *Phys. Fluids* 4, 586 (1961).

[7] B. Trubnikov and V. Kudryavtsev, *Proc. U.N. Intern. Conf. Peaceful Uses Atomic Energy 2d, Geneva, 1958*, 31, p 93.

[8] Neutron Physics Division. This report was issued June 19, 1961, as ORNL CF-61-6-63.

[9] L. Spitzer, Jr., *et al.*, *Problems of the Stellerator as a Useful Power Source*, NYO-6047 (August 1954).

introduction of the (d,t) neutrons into a fusion reactor blanket which will multiply them by $Be(n,2n)$ reactions, moderate, and finally capture them through the $Li^6(n,\alpha)H^3$ reaction. Recent cross-section data were used to re-evaluate the blanket and to evaluate two variations of it: a homogeneous blanket with increased beryllium content and a heterogeneous blanket. Tritium breeding ratios for the two variations were 1.228 and 1.450 (for a 15-cm-thick Be region) respectively. The method of calculation and calculational models are given.

6.2.2 Method of Calculation and Group Constants

The calculations were performed with a multigroup diffusion theory code for the IBM 7090 written by the Oak Ridge Central Data Processing Facility. (The help of G. E. Whitesides and, especially, J. Replogle in performing the machine calculations is gratefully acknowledged.) It is similar to the GNU code[10] but differs from it in that transfer cross sections rather than age theory are used to treat heavy-element slowing down, inelastic scattering may be handled more flexibly, and more general boundary conditions are permitted.

The group structure to 0.1 Mev is given in Table 6.1. Neutrons were introduced in the narrow group at 14.5 Mev. All cross sections were averaged with a $1/E$ spectrum. Hafele's beryllium (n,α) and maximum $(n,2n)$ cross sections were used.[11] Other cross sections above 1 Mev were taken from Howerton's compilation.[12] Cross sections and the group structure below 1 Mev are those of Nestor.[13] The thermal group cross sections were computed for a temperature of 360°C.

The $(n,2n)$ spectrum was treated by considering the incident neutron to be inelastically scattered, leaving the Be^9 nucleus in a 2.43-Mev excited state. The Be^9 nucleus was then assumed to emit the second neutron, leaving the Be^8 nucleus with 1.67-Mev energy relative to the Be^9 ground state. This treatment does not extent the spectrum to zero energy and hence gives a conservative estimate of the breeding ratio. Iron inelastic scattering transfer was treated with the evaporation model. Iron and beryllium transfer cross sections above 1 Mev are given in Table 6.2. Note that for beryllium,

$$\sum_j \sigma_{n,2n}(i \to j) = 2\sigma_{n,2n}(i) .$$

Removal of neutrons is treated correctly by using a fictitious $\sigma_a = -\sigma_{n,2n}(i)$. Elastic transfers from a group to the next group below were taken as $\xi\sigma_s/\Delta u$.

6.2.3 Calculational Models

The calculations were performed in infinite cylindrical geometry. A central void 107 cm in radius represented the plasma. The blankets, all 61 cm thick, surrounded the void. Two types of blankets, homogeneous and heterogeneous, were studied. Neutrons were introduced by means of an appropriate boundary condition at the void-blanket interface.

The first homogeneous blanket was that considered by Spitzer *et al.*[9] The composition is given in Table 6.3. The second homogeneous blanket had a beryllium density ten times that of the first. Though the second blanket is physically unrealizable, an expanded blanket consistent with the densities would give the same result.

[10] C. L. Davis, J. M. Bookston, and B. E. Smith, *GNU II – A Multigroup One-Dimensional Diffusion Program*, GMR-101 (1957).

[11] W. Hafele, *The Fast Multiplication Effect of Beryllium in Reactors*, ORNL-2779 (Sept. 8, 1959).

[12] R. J. Howerton, *Semi-Empirical Neutron Cross Sections*, Part II, vol 1, UCRL-5351 (November 1958).

[13] C. W. Nestor, *Multigroup Neutron Cross Sections*, ORNL CF-60-3-35 (March 1960).

Table 6.1. Group Structure Used in Tritium Breeding-Ratio Calculations

Group	Upper Energy (Mev)	Lower Energy (Mev)
1	14.5	14.49
2	14.49	10.0
3	10.0	5.0
4	5.0	4.0
5	4.0	3.0
6	3.0	2.0
7	2.0	1.0
8	1.0	0.3
9	0.3	0.1

Table 6.2. Beryllium and Iron Transfer Cross Sections

Group (i)	Cross Sections (barns)						
	$k = 1$	$k = 2$	$k = 3$	$k = 4$	$k = 5$	$k = 6$	$k = 7$
	Beryllium, $\sigma_{n,2n}(i \to i + k)$						
1	0.242	0.308	0	0	0.209	0.283	0.063
2	0.50	0	0	0.119	0.335	0.096	
3	0.115	0.143	0.148	0.368	0.237		
4	0	0.064	0.614	0.434			
5	0	0.166	0.838	0.042			
6	0	0.115	0.115				
	Iron, $\sigma_{in}(i \to i + k)$						
1	0.018	0.228	0.159	0.202	0.265	0.285	0.143
2	0.184	0.129	0.195	0.272	0.317	0.167	0.028
3	0.091	0.171	0.296	0.422	0.261	0.037	
4	0.133	0.286	0.502	0.380	0.066		
5	0.244	0.502	0.423	0.072			
6	0.406	0.413	0.086				
7	0.358	0.087					

Table 6.3. Composition of the First Homogeneous Blanket

Element	Nuclear Density ($\times 10^{-24}$ nuclei/cm^3)
H	0.0176
O	0.0088
Li^7	0.0106
Li^6	0.000865
Fe	0.352
Be	0.0062

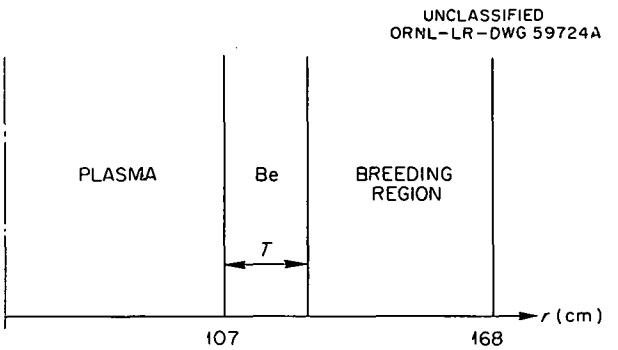

Fig. 6.1. Model of the Heterogeneous Blankets.

A layer of beryllium was interposed between the plasma and the H^3 breeding region to form the heterogeneous blankets as indicated in Fig. 6.1. The compositions of the breeding region and the first homogeneous blanket were the same except that the former contained no beryllium. Three blankets with beryllium region thicknesses of 5, 10, and 15 cm were studied.

6.2.4 Results and Conclusions

The homogeneous blanket results, given in Table 6.4, are in general agreement with those of Spitzer *et al.*[9] The heterogeneous blanket results are listed in Table 6.5 and plotted in Fig. 6.2. The breeding ratio is given directly by the Li(n,α) events, and the neutron multiplication due to beryllium is equal to [1 + Be($n,2n$) events]. As

Table 6.4. Events per Neutron Introduced into the Homogeneous Blankets

Event	Beryllium Density (nuclei/cm^3)	
	0.0062×10^{24}	0.062×10^{24}
$Li^6(n,\alpha)$	0.860	1.228
$Fe(n,\gamma)$	0.199	0.257
$Be(n,\alpha)$	0.009	0.069
$Be(n,2n)$	0.076	0.560
Leakage	0.004	0.0006

Table 6.5. Events per Neutron Introduced into the Heterogeneous Blanket

Event	Thickness of Be Annulus, T (cm)		
	5	10	15
$Li^6(n,\alpha)$	1.250	1.419	1.450
$Fe(n,\gamma)$	0.257	0.259	0.244
$Be(n,\alpha)$	0.072	0.115	0.142
$Be(n,\gamma)$	0.003	0.030	0.099
$Be(n,2n)$	0.619	0.934	1.120
Leakage	0.031	0.103	0.177

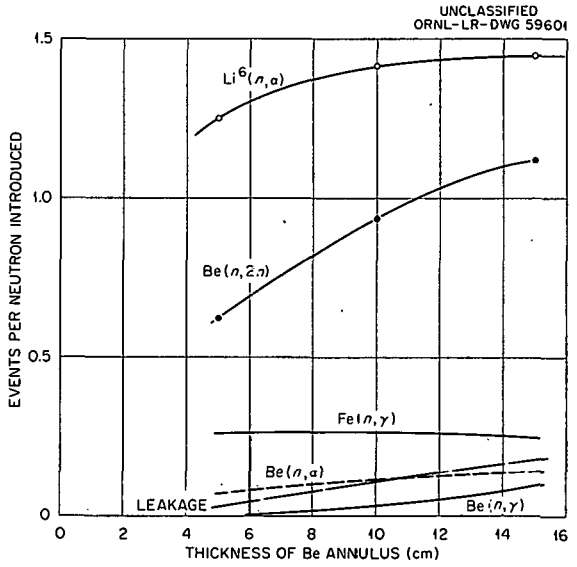

Fig. 6.2. Events per Neutron Introduced vs Thickness of the Beryllium Annulus (Heterogeneous Blanket).

expected, the heterogeneous blanket gives a significantly higher breeding gain than does the homogeneous blanket. Indeed, H^3 breeding appears to be possible.

6.3 ENERGY DISTRIBUTION OF IONS AND ELECTRONS IN DCX AFTER BURNOUT

T. K. Fowler[14] M. Rankin

A previously discussed Oracle code solving coupled Fokker-Planck equations for ion and electron energy distributions in DCX in steady state has been completed and a report issued.[15] Monoenergetic particle sources and loss terms representing scattering out of mirrors are included. The loss rate at each energy depends on the plasma potential, ϕ, which is determined self-consistently along with the energy distributions and which is positive to restrain electrons. Electrons are confined adiabatically; both adiabatic and absolute containment of ions are studied. Two cases of electron injection are studied: electrons arriving from the outside with energy ϕ and zero-energy electrons produced by ionization within the plasma. The electron injection rate, I_-, is left as a parameter. Actually, except for normalization, the energy distributions prove to be functions of I_-/I_+ only. They also scale with the ion injection energy.

Numerous cases have been run. The outstanding features are evident in a typical example, Fig. 6.3. Because electrons are so much more mobile than ions, only the high-energy tail of the electron distribution lies above the potential barrier, ϕ, and the distribution is approximately Maxwellian. Escaping particles carry away energy of $\sim\phi$. It is energy conservation, then, that fixes the potential, and when fixed, the ratio of electron temperature to ϕ adjusts to allow enough of the distribution to escape above the barrier to satisfy particle conservation. It will be observed that in postburnout cases, scattering being the only loss, the potential is quite high. With increasing I_-/I_+, ϕ goes down.

In contrast to the electrons, the distribution of ions, which feel no barrier, is peaked at the

[14] Physics Division.

[15] T. K. Fowler and M. Rankin, *Energy Distributions of Ions and Electrons in DCX After Burnout: Oracle Code EDDIE*, ORNL-3161 (August 1961).

injection energy, as in Fig. 6.3, and is non-Maxwellian. For larger I_-/I_+ the peak is less sharp and may lie lower, as in Fig. 6.4.

In both figures, H_2^+ is injected at 600 kev, H^+ ions from dissociation being deposited in the plasma with energy $\frac{1}{2}(600 \text{ kev} - \phi)$.

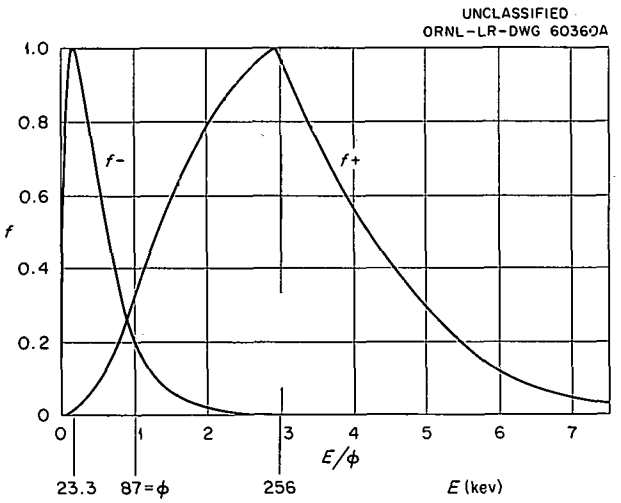

Fig. 6.3. Ion and Electron Energy Distributions, with $I_-/I_+ = 0.87$.

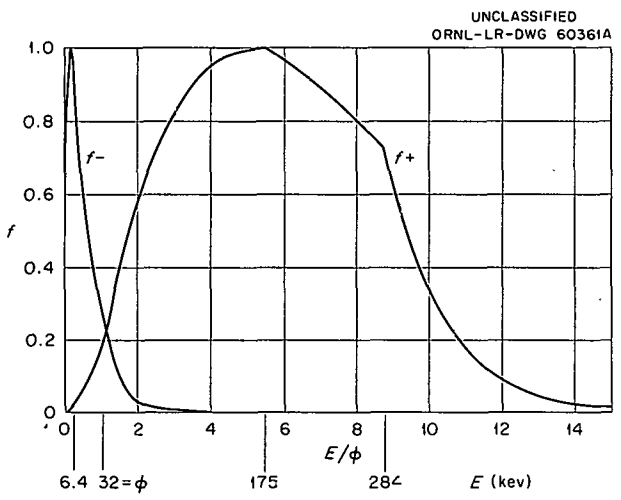

Fig. 6.4. Ion and Electron Energy Distributions, with $I_-/I_+ = 3.7$.

6.4 DISSOCIATION OF THE H_2^+ MOLECULE BY ELECTRONS AND PROTONS

R. G. Alsmiller, Jr.

In a recent publication Gryzinski[16] introduced a formalism for calculating the ionization and excitation of atomic systems by charged-particle impact. Since the theory appears to give reliable results in the low-energy region where the Born approximation is not accurate, it was used to calculate the total cross section for the dissociation of the H_2^+ molecule by electrons and protons for comparison with the Born approximation results.[17,18]

In making the calculation, the velocity distribution of the bound electron was obtained from the usual L.C.A.O. wave function for the ground state of the H_2^+ molecule,[19] the molecular protons were considered to be fixed force centers, and a classical average was taken over molecular orientations. It was further assumed that all excitations of the molecule would lead to dissociation. In the case of dissociation by electrons, electron-electron exchange was not included. (M. Gryzinski has calculated the ionization of the H_2 molecule by electrons and obtained very good results without the inclusion of exchange.[16])

The total cross section for dissociation by electrons is shown in Fig. 6.5 and by protons in Fig. 6.6 (an algebraic error in the published work of Gryzinski was corrected before the proton calculation was done). Also shown are the Born approximation results. The two Born curves in Fig. 6.5 correspond to including no electron-electron exchange and to including the prior-exchange terms. The use of the postexchange terms gives a peak which is considerably larger than those shown in the figure.

---

[16] M. Gryzinski, *Phys. Rev.* 113, 2 (1959).

[17] E. V. Ivash, *Phys. Rev.* 112, 1 (1958).

[18] R. G. Alsmiller, Jr., *Cross Sections for the Dissociation of H_2^+ and D_2^+ by a Vacuum Arc*, ORNL-2766 (Oct. 6, 1959).

[19] L. Pauling and E. B. Wilson, *Introduction to Quantum Mechanics*, McGraw-Hill, New York, 1955.

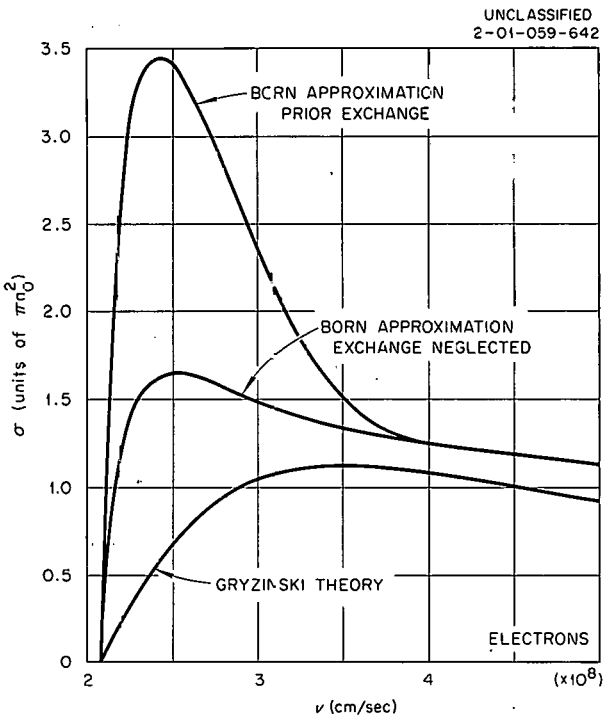

Fig. 6.5. Dissociation of H_2^+ by Electrons.

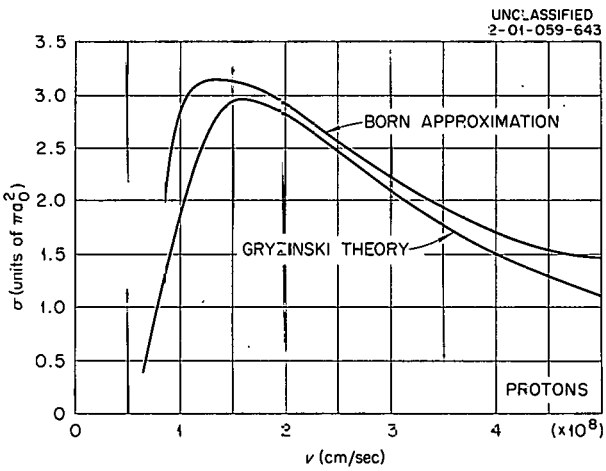

Fig. 6.6. Dissociation of H_2^+ by Protons.

6.5 INSTABILITY IN DCX-1

T. K. Fowler[14] E. G. Harris[20]

An explanation of coherent radiation in DCX-1 indicating instability has been sought in a resonance of ion cyclotron motion with electron plasma oscillations, emphasized by Harris,[21] and in the "negative-mass" instability discovered by Nielsen.[22] The latter approximates the effect of the negative radial gradient of a magnetic mirror field at the midplane. In such a field, a real acceleration moves particles out into weaker field regions where the angular velocity is less, and a real deceleration has the opposite effect. Thus, efforts to relieve space charge by accelerating leading particles in a circulating bunch and decelerating trailing particles actually bunch the particles azimuthally and to a degree not fully compensated by the associated radial spreading. An initial spread in angular velocity, equivalently an energy spread, tends to overcome the effect. Calculations for DCX-1 geometry[23] show the energy spread required for stability to be several tens of kev, the order of the observed spread.

The negative mass effect has been introduced into an approximate calculation of Harris' resonance instability in order to combine the two mechanisms. It was found that the two mechanisms essentially separate according to the direction of propagation of perturbations. With the perturbed electric field pointing strongly along the direction of electron motion along magnetic field lines, the dispersion relation reduces to that of Harris and

[20] Consultant, University of Tennessee.

[21] E. G. Harris, *J. Nuclear Energy, Pt C: Plasma Physics* 2, 138 (1961).

[22] C. E. Nielsen, A. M. Sessler, and K. R. Symon, CERN Conf. Report, 1959.

[23] T. K. Fowler, *Calculation of the "Negative Mass" Instability for DCX-1*, ORNL CF-61-7-1 (July 1961).

resonance dominates. When $\vec{E}$ points perpendicularly to the field along the direction of azimuthal motion of the ions, the dispersion relation of Nielsen is obtained and the field gradient effect is dominant.[24]

6.6 CONCERNING A POSSIBLE APPROACH TO THE MODE I–MODE II TRANSITION PROBLEM

Gareth Guest[25] Albert Simon[26]

An attempt has been made, following the method of Kadomtsev and Nedospasov,[27] to analyze the mode I–mode II instability[28] in terms of a simple model of the gaseous arc discharge in a uniform longitudinal magnetic field. The essential features of the model are the inclusion of streaming effects to the end walls as utilized by Simon[29] and the neglect of lower-order terms in the transverse motion of charged particles due to electrostatic fields. Transverse motion of the ions and electrons is attributed entirely to diffusion processes and to Hall currents arising from $\vec{j} \times \vec{B}$ terms in the equations of motion.

The theory leads to a dispersion relation which predicts instability of the plasma for magnetic fields greater than a critical value, B_c, given by

$$B_c \cong 1.5 \times 10^{13}\, n_0 A \sigma_i \frac{T_i}{T_e} \sqrt{k T_e m_e c^2}\,,$$

where T_e and T_i are the electron and ion temperatures respectively, σ_i is the ion–neutral atom collision cross section, A is the ion mass number, and n_0 is the neutral atom number density.

[24] T. K. Fowler and E. G. Harris, *The Cyclotron Resonance Instability with Negative Mass Ions*, ORNL-TM-25 (October 1961).

[25] Research participant from Department of Physics, North Texas State College, Denton, Texas.

[26] Now at General Atomic Div., General Dynamics Corp., San Diego, Calif.

[27] B. B. Kadomtsev and A. V. Nedospasov, *J. Nuclear Energy, Pt C: Plasma Physics* 1, 230 (1960).

[28] R. V. Neidigh, *The Effect of a Pressure Gradient on a Magnetically Collimated Arc*, ORNL-2288 (May 27, 1957).

[29] A. Simon, *An Introduction to Thermonuclear Research*, chap. IX, Pergamon, New York, 1959.

6.7 STABLE PLASMAS

T. K. Fowler[14]

A new method has been developed for examining the stability of solutions of the Vlasov-Boltzmann equation too complicated to be treated by conventional methods leading to dispersion relations. Less information is obtained. The method employs a sufficiency condition. When applicable, it simply gives the answer that the system is stable, with no details on modes, frequencies, and so forth.

As an illustration of the complexity of situations which may be treated, stability has been proven for all monotonic decreasing functions of the equilibrium energy. This includes the known stable case of spatially infinite "single-humped" functions of v. Because energy rather than v^2 is the variable, the new, larger class of the functions may be spatially varying if the energy contains a potential. If the potential is a well, such as the self-consistent gravitational potential of a star, the plasma may in fact be confined in the well. The proof is approximately valid for plasmas confined by rf radiation pressure, which simulates a static potential well for particles of either sign of charge.

The proof was given first only for electrostatic forces between particles.[30] Now it has been extended to include magnetic forces if retardation is neglected ($c = \infty$). Collisions are neglected as usual. Otherwise the result is more general than is usually possible, even with magnetohydrodynamic approximations. Besides the fact that the plasma can be confined in space, there is no necessity to assume charge neutrality in equilibrium (or $\beta = 1$) or for surface charge and currents to be confined to sheaths of zero thickness. Electrons and any number of ion species may be treated so long as the distribution for each depends properly on the respective equilibrium energy function.

The new method has also been employed to examine stability in magnetic mirrors. The field is taken as cylindrically symmetric but otherwise arbitrary. The only conclusion so far is that, including electrostatic forces only, distributions which are functions only of the equilibrium energy and canonical angular momentum, sufficient for

[30] T. K. Fowler, *Phys. Fluids* 4, 1393 (1961).

describing DCX, are unstable only against perturbations lacking the symmetry of the field. Examples are instabilities due to azimuthal lumping of space charge predicted by Harris[31] and by Nielsen.[32]

The general idea of proof, similar to the method of Low,[33] is to find some Hermitian positive definite operator, H_+, whose expectation value $(f, H_+f) \equiv \int d\vec{x}\, d\vec{v}\, f^* H_+ f$ with respect to distribution perturbations, $f(\vec{x}, \vec{v}, t)$, is independent of time as f varies in time according to the linearized Vlasov-Boltzmann equation. The constancy of such an average over f guarantees that no f grows indefinitely. To show that an H_+ with these properties exists, one seeks as an "integrating factor" an operator whose multiplication with the Vlasov-Boltzmann equation yields the form

$$H_+ \frac{\partial f}{\partial t} + AF = 0 ,$$

where A is anti-Hermitian. That $(\partial/\partial t)(f, H_+ f) = 0$ follows. (Details appear in ref 30.)

6.8 INSTABILITIES IN A HOMOGENEOUS, ANISOTROPIC PLASMA

Y. Shima

It is well known that a homogeneous (in x space) plasma which is situated in a constant magnetic field and whose distribution function in velocity space is Maxwellian is stable against small perturbations. More generally, it was shown by Rosenbluth[34] that a sufficient condition for stability is that the distribution function be isotropic and a decreasing function of v^2.

It has been conjectured that all anisotropic plasmas are unstable, but no general proof has yet been given. A somewhat general investigation of the problem of homogeneous anisotropic plasmas has now been made. For the sake of simplicity, only systems with no initial electric or magnetic field were considered. Also, the ions were assumed to be infinitely heavy so that in each case there was only one distribution function, namely that of the electrons.

Using the Vlasov equation, it was shown that the following general classes of distribution functions are indeed unstable:

$$f_0 = \delta(v_1)\, f(v_2^2, v_3^2) , \qquad (1)$$

where $f(v_2^2, v_3^2)$ may be any arbitrary function except $\delta(v_2^2)\,\delta(v_3^2)$;

$$f_0 = f_0(v_1^2 + \alpha v_2^2, v_3^2) , \qquad 0 < \alpha < 1 , \quad \alpha > 1 . \qquad (2)$$

It should be noted that the second class of functions includes distribution functions of two- and three-temperature plasmas.

In addition to the above, it was shown that a sufficient condition for instability of a distribution function $f_0(v_1^2, v_2^2, v_3^2)$ is that $g < 0$, where

$$g = \left(1 - \frac{\omega_p^2}{k^2} \int \frac{\vec{k} \cdot \partial f_0 / \partial \vec{v}}{(\vec{k} \cdot \vec{v})}\, d^3 v \right) \times \left(c^4 k^4 + c^2 k^2 \omega_p^2 A + \omega_p^4 \frac{k^2}{4 k_1^2 k_2^2 k_3^2} B \right) ,$$

$$A = a_{11} + a_{22} + a_{33} ,$$

$$B = -k_1^4 a_{11}^2 - k_2^4 a_{22}^2 - k_3^4 a_{33}^2 + 2k_1 k_2 a_{11} a_{22} + 2k_1 k_3 a_{11} a_{33} + 2k_2 k_3 a_{22} a_{33} ,$$

$$a_{ii} = 1 + \int \frac{v_i^2\, \vec{k} \cdot \partial f_0 / \partial \vec{v}}{(\vec{k} \cdot \vec{v})}\, d^3 v ,$$

ω_p = plasma frequency $\sqrt{4\pi n e^2 / m}$.

The meaning of the condition is that the distribution function will be unstable if a vector $\vec{k}$ can be found such that $g < 0$. It should be emphasized that this is only a sufficient condition.

The topic is discussed in detail elsewhere.[35]

[31] E. G. Harris, *J. Nuclear Energy; Pt C: Plasma Physics* 2, 138 (1961).

[32] C. E. Nielsen, A. M. Sessler, and K. R. Symon, CERN Conf. Report, 1959.

[33] F. E. Low, *Phys. Fluids* 4, 842 (1961).

[34] M. N. Rosenbluth, Lecture in the International Summer Course in Plasma Physics, Denmark, August 1960.

[35] Y. Shima, *Instabilities in a Homogeneous, Anisotropic Plasma*, ORNL CF-61-7-69 (July 31, 1961).

6.9 ELECTROSTATIC ION-CYCLOTRON PLASMA INSTABILITIES IN A TWO-FLUID HYDRODYNAMIC THEORY

H. K. Wimmel[36]

A two-fluid hydrodynamic theory is shown to describe certain electrostatic ion-cyclotron plasma instabilities of the Harris[37] type in a semiquantitative way. The ions (electrons) are described by the first three (two) moment equations of the collisionless Boltzmann equation, implying zero electron temperature. Only purely longitudinal ("electrostatic") oscillations are considered. If the electron plasma frequency ω_p is greater than the ion cyclotron frequency Ω_c and if the ion pressure is sufficiently anisotropic, unstable oscillations occur with $|\mathrm{Re}(\omega)| \simeq \Omega_c$. Owing to the limitations of the model, only the cases in which the wavelength of the oscillation mode is large compared with the ion cyclotron radius can be treated. Instabilities at higher harmonics of the ion cyclotron frequency are also excluded. Quantitative agreement with the results of Harris' exact treatment of the infinite plasma is found only for k nearly parallel to B^0, whereas otherwise our equations contain stabilizing extra terms not obtained from the rigorous theory. Estimates of the critical pressure anisotropy, at which instability sets in, are given. The critical anisotropy is smallest for the "resonance" case, $\omega_p \cong \Omega_c$, with k lying nearly parallel to B^0. Short-wavelength modes are less stable than long-wavelength modes. The two-fluid hydrodynamic model allows a pictorial understanding of the unstable oscillation modes and of the ract that geometric boundaries have little influence on the conditions for instability. (Details appear in ref 38.)

6.10 REDUCTION OF THE VLASOV EQUATION

T. K. Fowler[14]

A transformation to equilibrium constants of motion is employed to convert the integro-differential linearized Vlasov-Boltzmann equation to an integral equation. The result is an equation in charge and current density perturbations, functions of $\vec{x}$ only. It is homogeneous and poses an eigenvalue problem in order to obtain a dispersion relation. Symmetry in two dimensions, as for the cylindrically symmetric distributions in the uniform magnetic field region of DCX-2, permits further reduction to a one-dimensional equation amenable to numerical solution. An important feature, evident from the equation, is that in *unstable* eigenmodes the charge distribution is confined to the region of space occupied by the equilibrium charge distribution. (Some details appear in ref 39.)

6.11 CALCULATIONS OF H_2^+ ORBITS IN THE DIP REGION OF DCX-2

G. R. North C. E. Parker

TILDA (Trajectories in a Legendre-developed aether) is a code written (in FORTRAN for the IBM 7090) to integrate the usual equations of motion for charged particles in a magnetic field. Nystrom's version of the Runge-Kutta method[40] was used. The only approximation is that of the single-particle orbit (no scattering, interactions, etc.). The orbits can be followed reliably for about 100 turns. It has been found that the use of Cartesian coordinates in the calculation is far more accurate than use of cylindrical coordinates.

The magnetic field is calculated from an expansion in Legendre polynomials. The magnetic field subroutines used in the calculation were written by M. W. Garrett and C. E. Parker. These routines permit the rapid and accurate calculation of the required quantities. It might also be noted that magnetic parameters (dimensions, currents, etc.) are input data for the code and are very easily changed. A limitation is that fields may not be calculated near the coil edges. The code is reasonably economical in that 1 turn in the

---

[36] On loan from Yale University.

[37] E. G. Harris, *Phys. Rev. Letters* 2, 34 (1959); ORNL-2728 (1959); *Proc. Conf. Theor. Aspects Contr. Fusion Res.*, Gatlinburg, Tennessee [TID-7582 (ORNL-2805), 1959], p 131; P. B. Burt and E. G. Harris, *Bull. Am. Phys. Soc.* 6, 300 (1961).

[38] H. K. Wimmel, *Electrostatic Ion-Cyclotron Plasma Instabilities in a Two-Fluid Hydrodynamic Theory*, ORNL-3170 (August 1961).

[39] T. K. Fowler, *Plasma Stability Analysis Employing Equilibrium Constants of Motion*, ORNL-3123 (1961).

[40] Acknowledgement is made to W. Gautchi (Mathematics Panel) for this helpful advice.

DCX-2 field takes about 15 sec (70 cents) of computer time.

It was found that the field dip decreases the pitch of the orbit to about 1 or 2° and that this pitch is maintained after the particle reflects from the mirror. Also, the orbits were not too sensitive to changes of dip current over a range of 300 amp/in.^{2}.

7. Magnetics

7.1 ACTIVITIES OF THE ENGINEERING SCIENCES GROUP

The Engineering Sciences Group continued to do service work for the Division in magnetic-field and coil design, ion trajectories, and magnetic measurements. Special efforts were devoted to DCX-2.

Some experimental and theoretical work has been done on superconductivity. D. L. Coffey investigated especially the methods for making joints between superconducting wires and the external current leads. In the following section, a short paper by Gauster and Parker considers procedures for calculating superconducting solenoids. Methods for coil optimization are shown, and numerical examples illustrate the calculations. The case of a superconducting coil in an external, coaxial, homogeneous magnet field is considered in greater detail, since this arrangement can be used advantageously for experiments with medium and high magnetic field strength without the requirement of excessive wire lengths.

Calculations and experiments deal with the design of safety barriers to be used for tests with magnet coils where parts might be ejected in case of failure. A report will be given in the first semiannual report for 1962.

7.2 SOME CONCEPTS FOR THE DESIGN OF SUPERCONDUCTING SOLENOIDS

W. F. Gauster C. E. Parker

7.2.1 Introduction

The starting point for every calculation procedure for superconducting magnet coils is the "quenching characteristic" of the superconducting wire, that is to say, the correlation between transition current and transverse magnetic field. Some observations suggest that mechanical forces acting on the superconducting wire influence the quenching characteristic. It would, however, be very difficult to consider this factor in calculating a superconducting solenoid. Therefore the assumption will be made here that the quenching characteristic of a wire sample is also valid for a wire of any length, as used for winding a coil.

The following discussion on some typical cases of optimized superconducting solenoids is shown here without any mathematical derivations. It is based on calculation procedures presented by the authors in a paper with the same title as this report, to be published in the *Proceedings of the International Conference on High Magnetic Fields, November 1–4, 1961*, Massachusetts Institute of Technology, Cambridge, Mass. The authors wish to acknowledge many useful and stimulating discussions with D. L. Coffey, J. N. Luton, Jr., R. G. Mallon,[1] and P. A. Thompson, and the invaluable help of J. E. Simpkins in numerical calculations.

7.2.2 Coils with Rectangular Cross Section and Homogeneous Current Density

As is well known, the theory of conventional magnet coils, that is, coils having ohmic losses, has been ceveloped in great detail.[2] For instance, the problem of designing solenoids with rectangular cross section and homogeneous current density, having a minimum volume, has been solved by C. Fabry.[3] This solution, modified for superconducting coils, yields only approximate design data. The differences become very appreciable when coil outside diameter and length are not much greater

[1] Astra, Inc., Raleigh, N.C.

[2] W. F. Gauster, *Communication and Electronics* No. 52, 822–28 (January 1961). Contains a list of references on calculations for conventional coil design.

[3] C. Fabry, *L'Eclairage Electrique* (*Paris*) XVIII(43), 133–41 (1898), and *Journal de Physique* (*Paris*) IX, 129–34 (1910).

than the aperture of the solenoid. A new calculation procedure has been developed which holds for any shape of the superconducting magnet coils. The following example is illustrative.

Example 1. – An Nb-Zr wire (25% Zr) 20 mils in diameter is used at a temperature of 4.2°K. A representative quenching characteristic is shown in Fig. 7.1 (ref 4). The coil parameters are: inside radius a_1 = 5 cm (see Fig. 7.2); wire length l = 1400 ft; turn density n = 320 turns/cm^2. The total number of turns of the coil is N. The cases "zero external field" (B_0 = 0) and a coaxial, homogeneous, external field B_0 = 40 kilogauss are considered. Table 7.1 summarizes the results.

A superconducting coil in an external, coaxial, homogeneous magnetic field is a convenient experimental arrangement. Relatively strong magnetic fields acting on the superconductor can be achieved with small numbers of turns, and, therefore, relatively large radii can be used without excessive wire length. Such experiments are desirable in order to clarify the observed differences between the quenching characteristic of a short piece of superconducting wire and that derived from the performance of superconducting coils.

[4]The representative quenching characteristics shown in Fig. 7.1 are based on data taken from articles by R. H. Kropschot and V. Arp, *Cryogenics* 2(1), 1–15 (September 1961), and R. W. Boom and R. S. Livingston, "Superconducting Solenoids," to be published in the *Institute of Radio Engineers Proceedings*, and from experiments by D. L. Coffey, ORNL (private communications).

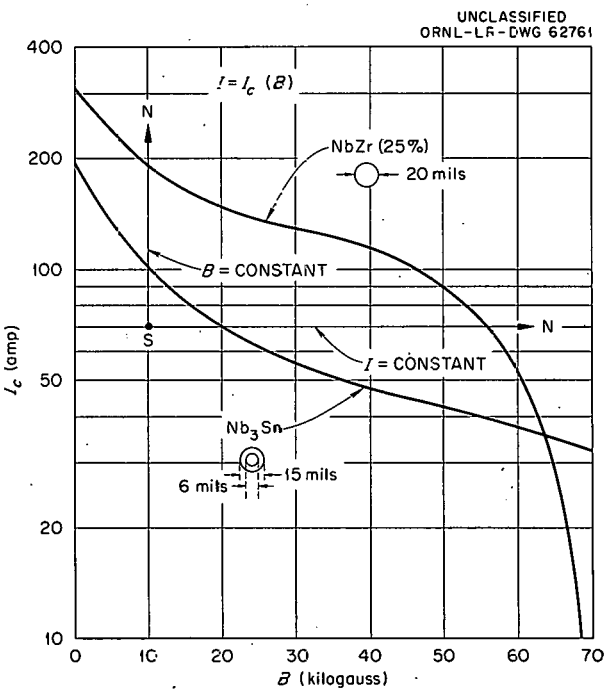

Fig. 7.1. Representative Quenching Characteristics of Superconducting Wires. Transversal field, dc; 4.2°K.

UNCLASSIFIED
ORNL-LR-DWG 62763R

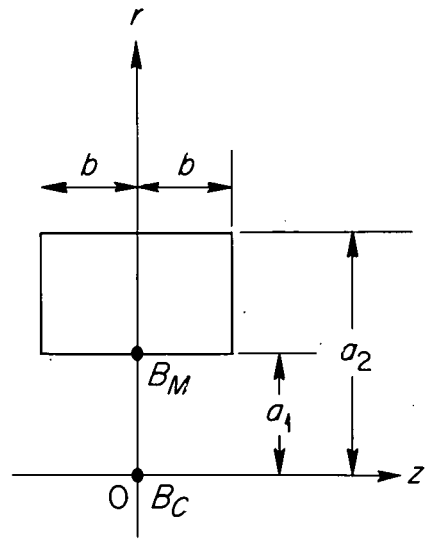

Fig. 7.2. Coil with Rectangular Cross Section.

Table 7.1. Volume-Optimized Superconducting Coils with Homogeneous Current Densities

a_1 = 5 cm; l = 1400 ft; n = 320 turns/cm^2; Nb-Zr wire

	$B_{c\ max}$ (kilogauss)	I (amp)	a_2 (cm)	b (cm)	N (No. of turns in coil)
$B_0 = 0$	17.8	138	5.60	3.40	1280
$B_0 = 40$	50.1	84	5.44	4.71	1300

7.2.3 Long Solenoids

By a long solenoid is meant one in which the length is very large compared to the inside diameter. It is assumed that all quantities are functions only of the radial distance r. In this case

only the axial component $B_z = B$ of the flux density, and the tangential component $i_\theta = nI$ of the current density, are present.

Example 2. – A long solenoid is wound with Nb_3Sn wire (quenching characteristic shown in Fig. 7.1); the turn density is $n = 200$ turns/cm^2. Under these conditions, in a single-layer long solenoid a current of 17.5 amp is necessary to produce 100 kilogauss in the aperture of the coil. The winding thickness $a_2 - a_1$ in this case is 22.7 cm. Much less superconducting wire is necessary if m concentric layers are used in such a way that the current I_k and the maximum flux density $B_{max,k}$ in each layer are correlated by means of the quenching characteristic ("volume-optimized coil"). A theoretical lower limit for the total wire length (and winding thickness $a_2 - a_1$) exists for $m \to \infty$. Under this condition for $B_0 = 100$ kilogauss the minimum coil thickness becomes $a_2 - a_1 = 10.1$ cm (to be compared with the winding thickness of 22.7 cm of a single-layer solenoid mentioned previously).

Example 3. – Winding thickness $a_2 - a_1 = 10.1$ cm (as calculated for $m = \infty$). If different numbers of layers m are considered, what optimum flux density can be achieved in the coil aperture? How large are the optimized layer currents I_k? The results are shown in Table 7.2.

Table 7.2. Optimized Superconducting Long Solenoid

$a_2 - a_1 = 10.1$ cm; $n = 200$ turns/cm^2; Nb_3Sn (6 to 15 mils); 4.2°K

m	B_0 (kilogauss)	I_k (amp)
∞	100.0	200 to 17.5
1	75.2	29.9
2	84.1	41.1; 25.2
6	92.5	59.5; 45.2; 37.3; 30.7; 25.5; 21.1

7.2.4 Field Optimization of a Superconducting Coil with Rectangular Cross Section and Nonhomogeneous Current Density

In general the field optimization of a superconducting coil with nonhomogeneous current density calls for an iteration method. If an initial current-density distribution over a given cross section is assumed, the corresponding flux-density distribution can be calculated. For each conductor the flux density dictates a maximum allowable current for the maintenance of superconductivity, determined by the quenching characteristic. This new current distribution produces another flux-density distribution, a new allowable current distribution, and so on. There is, however, no general criterion that indicates how good the initially assumed current density must be so that the iteration process converges.

A special iteration method which converges very fast is demonstrated in example 4, which follows. A coil with rectangular cross section (inside radius 20 cm, outside radius 40 cm, length 60 cm) is divided in ten layers, each 2 cm thick. An Nb_3Sn wire is used, having the quenching characteristic shown in Fig. 7.1. In a range 40 kilogauss $\leqq B_\perp \leqq$ 110 kilogauss, the quenching characteristic can be replaced with sufficient accuracy by the linear equation

$$B_\perp = M_0 - MI = 135 - 2I ,$$

where B is in kilogauss, and I is in amperes.

Table 7.3 shows the results of the iteration method. The layer currents are represented by $I_k^{(l)}$; $B_{max,k}^{(l)}$ represents the resulting maximum flux density in layer k; $l = 0$ indicates zero iteration; and $l = 1$ indicates the first iteration.

This optimization method is based on the observation that B_{max} occurs in the midplane for about half of the innermost layers and at the endplanes for the outside layers. The first-mentioned maxima are B_z values ($B_r = 0$), whereas the others are total flux density values $\sqrt{B_r^2 + B_z^2}$. For that reason this iteration method can match the maximum flux densities over the first inside layers identically with $M_0 - MI_k^{(0)}$. For the following layers, however, the values of $B_{max,k}^{(0)}$ are appreciably larger than the "allowed" values $M_0 - MI_k^{(0)}$, and more iterations are required to make these differences successively smaller. In the numerical example shown, however, already after the first additional iteration, "allowed" and actual flux-density values are so nearly the same that from a practical viewpoint no further iterations are necessary.

The field-optimized ten-layer coil produces in its center a flux density of $B_c = 100.81$ kilogauss. If the same coil is operated as a single-layer

Table 7.3. Field Optimization of a Superconducting Magnet Coil with Nonhomogeneous Current Density

$a_1 = 20$ cm; $a_2 = 40$ cm; $b = 30$ cm; $n = 200$ turns/cm^2

Nb_3Sn wire; 6 to 15 mils; 4.2°K

r (cm)	$I_k^{(0)}$ (amp)	M_0-$MI_k^{(0)}$ (kilogauss)	$B_{max,k}^{(0)}$ (kilogauss)	$I_k^{(1)}$ (amp)	M_0-$MI_k^{(1)}$ (kilogauss)	$B_{max,k}^{(1)}$ (kilogauss)
20–22	12.84	109.32	109.32	13.21	108.58	108.58
22–24	15.30	104.41	104.41	15.77	103.46	103.46
24–26	18.33	98.35	98.35	18.93	97.15	97.15
26–28	22.08	90.84	90.84	22.84	89.33	89.33
28–30	26.75	81.50	81.50	27.71	79.59	79.59
30–32	32.57	69.86	69.86	33.78	67.44	67.44
32–34	41.04	52.92	63.42	36.42	62.17	61.71
34–36	40.71	53.59	59.14	38.70	57.60	57.65
36–38	41.56	51.88	54.00	41.06	52.88	52.97
38–40	43.60	47.80	48.03	43.86	47.28	47.30

coil, $B_c = 82.55$ kilogauss, and $I = 23.12$ amp. An optimum single-layer coil with homogeneous current density, having an inner radius $a_1 = 20$ cm and producing $B_c = 100.6$ kilogauss (a flux density very near the 100.81 kilogauss shown above), was calculated as discussed in Sec 7.2.2. The results are:

$$a_2 = 52 \text{ cm}, \quad b = 46.9 \text{ cm}, \quad I = 15.76 \text{ amp}.$$

The volume of this coil is 3.0 times the volume of the field-optimized superconducting coil with nonhomogeneous current density that was described above.

7.3 COIL-DISLOCATION CALCULATIONS

G. R. North

The effects of small perturbations on the characteristics of coils are here estimated. Only four types of perturbations are considered: a lateral displacement, a small tilt, an axial displacement, and a small current change. The basic concept used is to imagine the coils as parts of an infinite solenoid and then to move a small section of the solenoid. This is equivalent to subtracting the field of the unperturbed coil from that of the perturbed coil. In all cases only the lowest-order term in the perturbation parameter is considered, and pessimistic assumptions are made throughout.

7.3.1 Lateral Dislocation

A useful form for the magnetic field is:

$$B_z(\rho, z_0) = \sum_0^\infty B_0^{(n)} P_n(0) \frac{\rho^n}{n!}$$

$$\cong B_0 - B_0'' \frac{\rho^2}{4}, \qquad (1)$$

where

B_0 = axial field,

$$B_0'' = \left.\frac{d^2 B_z}{dz^2}\right]_{z=z_0,\, r=0}.$$

Consider a coil dislocated laterally by an amount ϵ. Our problem is simply a change of coordinate systems:

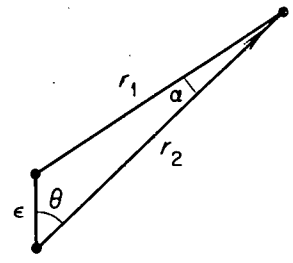

where

r_1 = distance from perturbed axis,
r_2 = distance from old axis.

By the sine law,

$$r_1 = r_2 \frac{\sin\theta}{\sin(\theta+\alpha)}, \tag{2}$$

which gives after expansion to first order in ϵ:

$$r_1 \cong r_2 \left(1 - \frac{\epsilon}{r}\cos\theta\right). \tag{3}$$

Taking the difference between the two fields:

$$\Delta B_z = B_0 - \frac{B_0''}{4} r_2^2 - \left[B_0 - \frac{B_0''}{4} r_2^2 \left(1 - \frac{\epsilon}{r}\cos\theta\right)^2\right],$$

$$\Delta B_z \cong -\frac{B_0''}{2} r\epsilon\cos\theta .$$

Taking the coil to be a single loop should be sufficient for our purposes (probably a pessimistic assumption, too):

$$B_0 = \frac{\mu_0 I R^2}{2} \frac{1}{(z^2+R^2)^{3/2}}, \tag{4}$$

$$B_0'' = \frac{3}{2}\mu_0 I R^2 \frac{4z^2 - R^2}{(z^2+R^2)^{7/2}}, \tag{5}$$

giving

$$\Delta B_z = -\frac{3}{4}\mu_0 I R^2 r\epsilon\cos\theta \left[\frac{4z^2 - R^2}{(z^2+R^2)^{7/2}}\right], \tag{6}$$

with

$$\mu_0 = 4\pi \times 39.3 \times 10^{-3} = 0.494 \text{ gauss-in./amp}$$
(gauss-inch-ampere system) .

We take $z = 0$, $\theta = 0$ such that $\Delta B|$ is largest; then

$$\Delta B_z \lesssim 0.37 \frac{Ir\epsilon}{R^3} \text{ gauss} . \tag{7}$$

For a bump to stop a particle of pitch α, we have

$$\Delta B = B\alpha^2 \text{ (adiabatic approximation)} , \tag{8}$$

or,

$$\epsilon \gtrsim \frac{B\alpha^2 R^3}{Ir\,(0.37)} .$$

As a numerical example take $I = 5 \times 10^5$ amp, $r =$ 5 in., $R = 25$ in., $B = 12{,}000$ gauss, $\alpha = 1° = 0.0175$ radian. Then, $\epsilon \gtrsim 0.062$ in.

7.3.2 Angular Dislocations

The lowest-order effect of an angular dislocation is to bend the field lines along with the coil. This will always reduce the B_z component of the field:

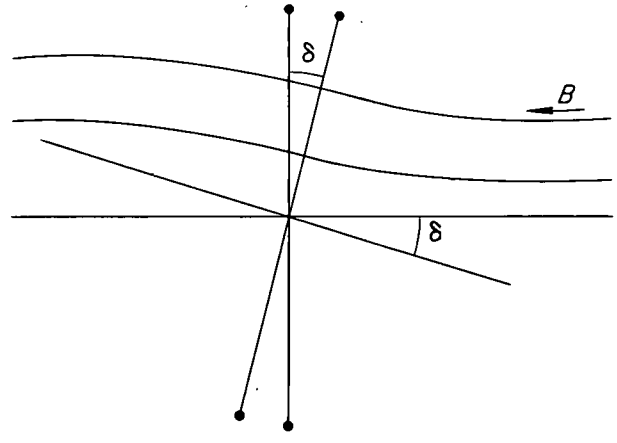

The perturbation then becomes

$$\Delta B_z = B_0 - B_0\cos\delta ,$$

$$\Delta B_z \cong \frac{B_0\delta^2}{2} .$$

In the single-loop approximation we get from Eq. (4)

$$\Delta B_z = \frac{\mu_0 I R^2}{2} \frac{1}{(z^2+R^2)^{3/2}} \frac{\delta^2}{2},$$

$$\Delta B_z \lesssim \frac{\mu_0 I}{4R}\delta^2 . \tag{9}$$

Taking the same dimensions as before with a tilt of $\delta = 1°$,

$$\Delta B_z = \frac{(0.494)(5 \times 10^5)(0.0175)^2}{10^2} = 0.76 \text{ gauss} .$$

This effect may not be very serious because the distortion should be gradual over long axial distances, and particles can move along the bent flux tubes.

7.3.3 Axial Dislocations

In practice the most likely dislocation will be axial because of the magnetic forces. In this case we have simply

$$\Delta B_z = B_0' \epsilon ,$$

$$\Delta B_z \cong -\frac{3}{2} \mu_0 I R^2 \frac{z\epsilon}{(z^2 + R^2)^{5/2}} . \quad (10)$$

The effect is largest when z is such that $B_0'' = 0$, or $z = R/2$. Then,

$$\Delta B \lesssim \frac{24}{56} \mu_0 \frac{I\epsilon}{R^2} ,$$

$$\Delta B \lesssim 0.21 \frac{I\epsilon}{R^2} .$$

Using the numbers from the last example we get:

$$\Delta B \lesssim 168\, \epsilon . \quad (11)$$

Considering the effect on orbits from Eq. (8),

$$\epsilon \gtrsim \frac{B\alpha^2}{168} . \quad (12)$$

Taking $\alpha = 1°$, $B = 12{,}000$ gauss, we obtain

$$\epsilon \gtrsim 0.02 \text{ in.}, \quad (13)$$

a staggering result. This implies that currents in the inboard booster coils will have to be adjusted experimentally to their proper working values.

7.3.4 Current Adjustments

As before, we calculate the change in field:

$$\Delta B \lesssim \frac{(\Delta I)\mu_0}{2R} \cong \frac{\Delta I}{100} \cong \Delta J \quad \text{(current density)} .$$

A change of 1 amp/in.^{2} is equivalent to about 1 gauss. Relating this now to orbits, we have $\Delta J = B\alpha^2$. For $\alpha = 1°$, $B = 12{,}000$ gauss, $\Delta J = 3.7$ amp/in.^{2}.

8. Vacuum Systems and Techniques

C. E. Normand
R. V. Neidigh
R. E. Clausing[1]
R. A. Strehlow[2]

8.1 EVAPORATIVE PUMPING

Operation of the large-scale getter pump test has demonstrated the feasibility of such systems.[3,4] Recent modifications of the evaporation procedure have yielded sticking coefficients of 0.8 and higher for hydrogen, oxygen, nitrogen, carbon monoxide, and carbon dioxide on vapor-deposited titanium films. This work has been reported[5] and is summarized here.

Following the previously reported sorption measurements on titanium films deposited in high vacuum on water-cooled copper, several exploratory evaporations were carried out which included deposition on liquid-nitrogen-cooled substrates and evaporation in the presence of several microns pressure of inert gas. The resulting deposits had much-increased sorption rates. The rates were large enough to lead to difficulty in interpretation of the data, and a new method of measuring sorption was developed which allows meaningful data to be obtained at very high sticking fractions. Indeed the measurement becomes more accurate as the sticking fraction approaches unity.

Consideration of a hollow sphere with a centrally located gas source leads to relations (1) to (4):

$$n_t = n_a + (1-\alpha)n_a + (1-\alpha)^2 n_a + (1-\alpha)^3 n_a \ldots , \quad (1)$$

$$n_t = \frac{n_a}{1-(1-\alpha)} , \quad (2)$$

$$n_t = n_a/\alpha , \quad (3)$$

$$\alpha = n_a/n_t , \quad (4)$$

where

n_t = total molecule flux to wall, $cm^{-2}\ sec^{-1}$,

n_a = molecules emitted from source, and, in steady state, the total number sorbed, $cm^{-2}\ sec^{-1}$,

α = sticking probability for gas molecules on the adsorbant wall, the number of particles that have collided with the wall at least once without being sorbed,

$(1-\alpha)$ = molecules not adsorbed per molecule impinging.

By properly positioning an ion gage it is possible to determine n_g, where n_g is given by Eq. (5):

$$n_g = (1-\alpha)n_a + (1-\alpha)^2 n_a + (1-\alpha)^3 n_a \ldots . \quad (5)$$

From Eqs. (1) and (4) above,

$$n_t = n_a + n_g , \quad (6)$$

$$\alpha = n_a/(n_a + n_g) . \quad (7)$$

[1]Metallurgy Division.

[2]Reactor Chemistry Division.

[3]C. E. Normand *et al.*, *Thermonuclear Project Semiann. Rept. July 31, 1960*, ORNL-3011, pp 118 ff.

[4]C. E. Normand *et al.*, *Thermonuclear Div. Semiann. Rept. Jan. 31, 1961*, ORNL-3104, pp 123–25.

[5]R. E. Clausing, *A Large Scale Getter Pumping Experiment*, ORNL-3217 (October 1961).

Stated in terms of measurable quantities (n_a is known if a metered gas leak is used),

$$\alpha = \frac{1}{1 + (n_g/n_a)} . \qquad (8)$$

For α near 1.0 the ratio n_g/n_a will be a small number giving relatively accurate values of α even if n_g (measured by an ion gage) is known only to 10 to 20%. The modified test system is shown in Fig. 8.1. The shape used in these experiments is that of a right cylinder of about $d = h \cong 30$ in. and is believed to approximate the sphere sufficiently well.

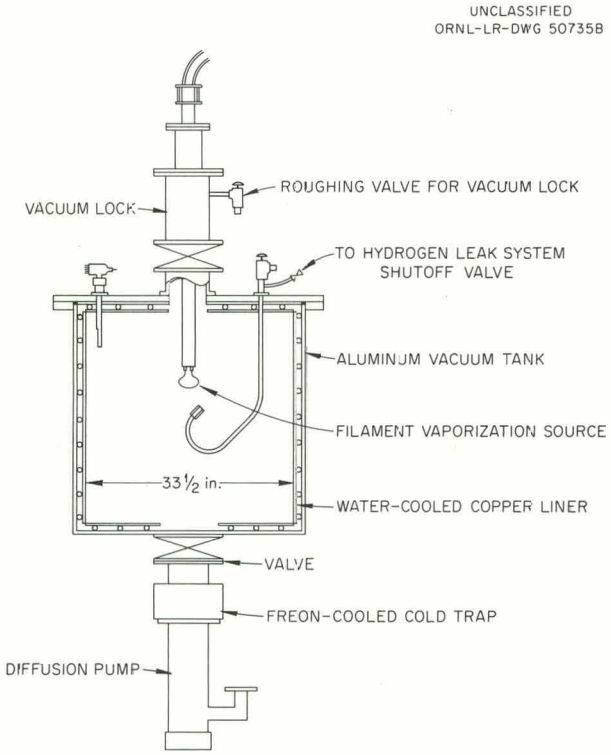

Fig. 8.1. Large-Scale Getter Test Experiment as Modified for Measuring Sticking Fractions.

The results obtained for sorption of several gases on films formed by various techniques are shown in Figs. 8.2 through 8.7 and are summarized in Table 8.1, which presents the initial sticking fractions for various combinations of gases and films. Since these data are discussed in ORNL-3217,[5] only a few aspects will be discussed here.

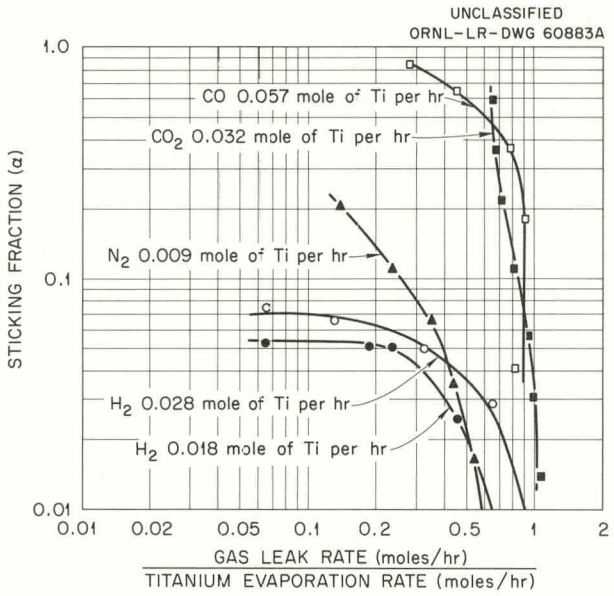

Fig. 8.2. Sorption of Gases onto Films Formed During Continuous Evaporation of Titanium onto a Surface at 10°C.

Note that α for hydrogen has been increased from 0.05 in the simple evaporations to about 0.2 by either evaporation onto substrates at −195°C or evaporation in the presence of 2.5 μ of inert gas (helium, argon, and methane have been used) and to 0.8 by a combination of both techniques. These data indicate that the improved sorption is brought about by independent mechanisms – one associated with the low-temperature substrate and the other with the presence of inert gas during the film deposition. These mechanisms will be studied with the aid of electron diffraction and electron microscopy.

Note that at 10°C the equivalent of a large number of geometric monolayers of hydrogen is sorbed with only a minor decrease in sorption rates while at −195°C the rates decrease much more rapidly as hydrogen is sorbed. This effect is attributed to the decreased diffusion rates at low temperature. If this is so, allowing the temperature to rise somewhat above −195°C to permit diffusion to occur more readily might be advisable where large quantities of hydrogen are to be sorbed. The diffusion of other gases appears to be very slow even at room temperature, as evidenced by the shape of their sorption curves.

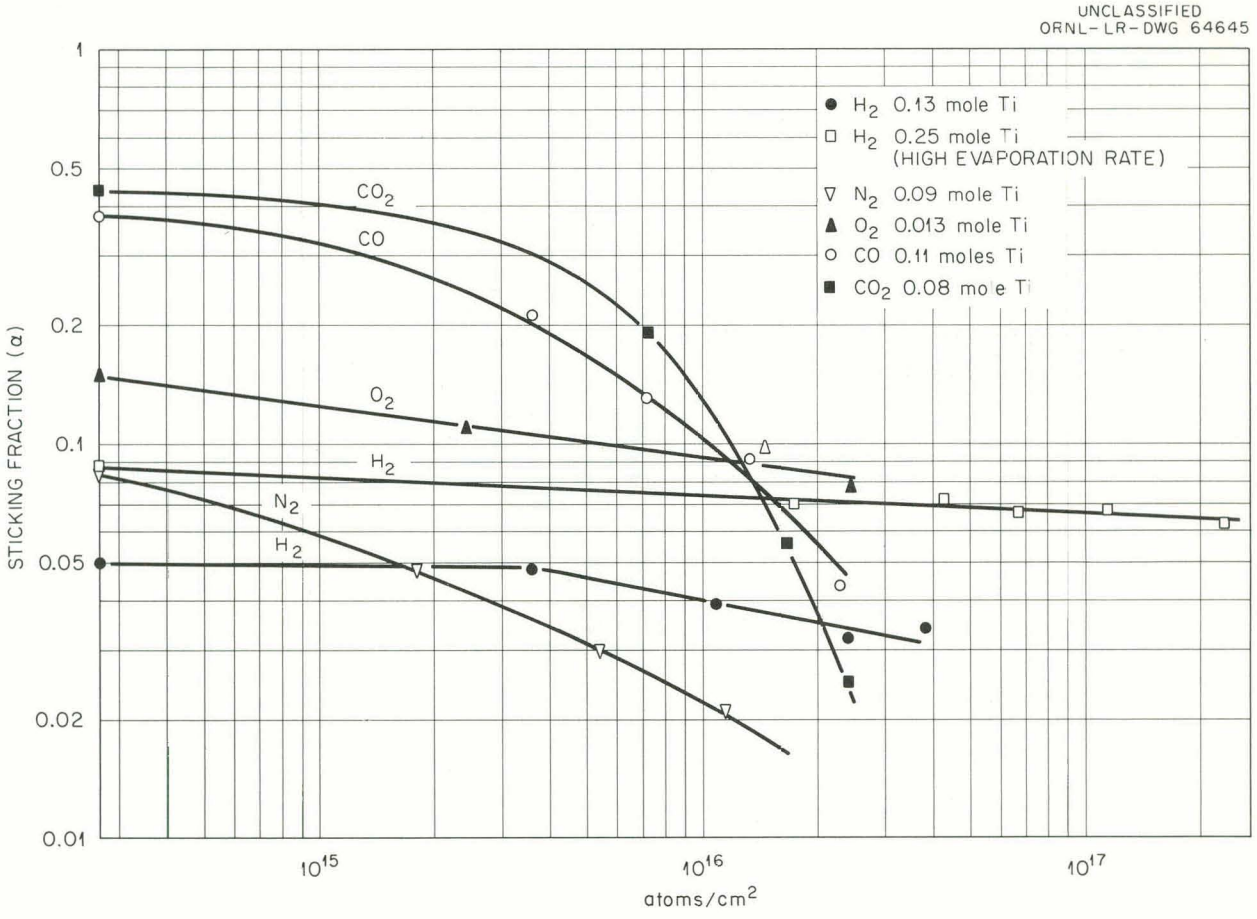

Fig. 8.3. Sorption of Gases onto Films Formed by Titanium Evaporation in High Vacuum onto a Surface at 10°C.

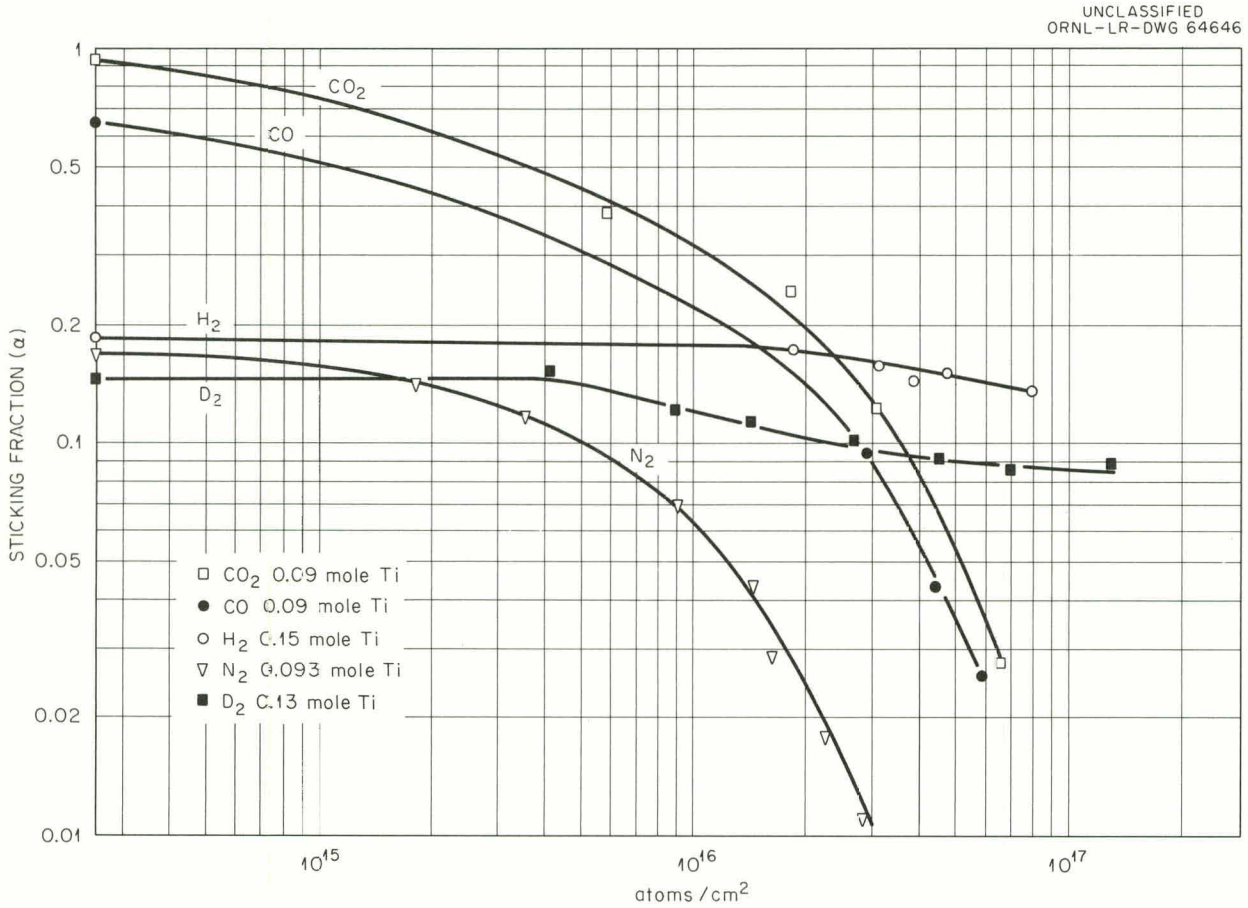

Fig. 8.4. Sorption of Gases onto Films Formed by Titanium Evaporation onto a Surface at 10°C in the Presence of 2.5×10^{-3} mm of Helium.

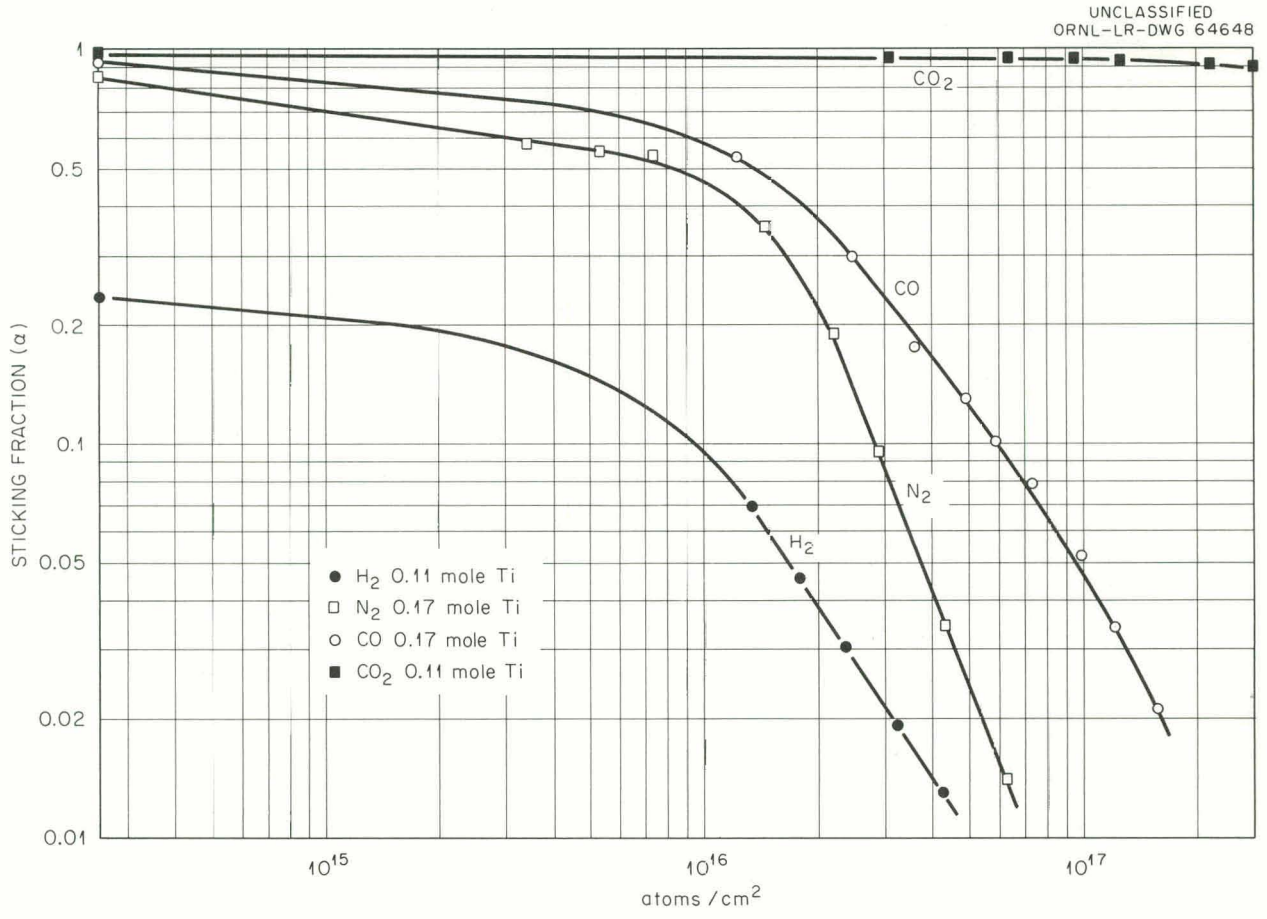

Fig. 8.5. Sorption of Gases onto Films Formed by Titanium Evaporation in High Vacuum onto a Surface at −195°C.

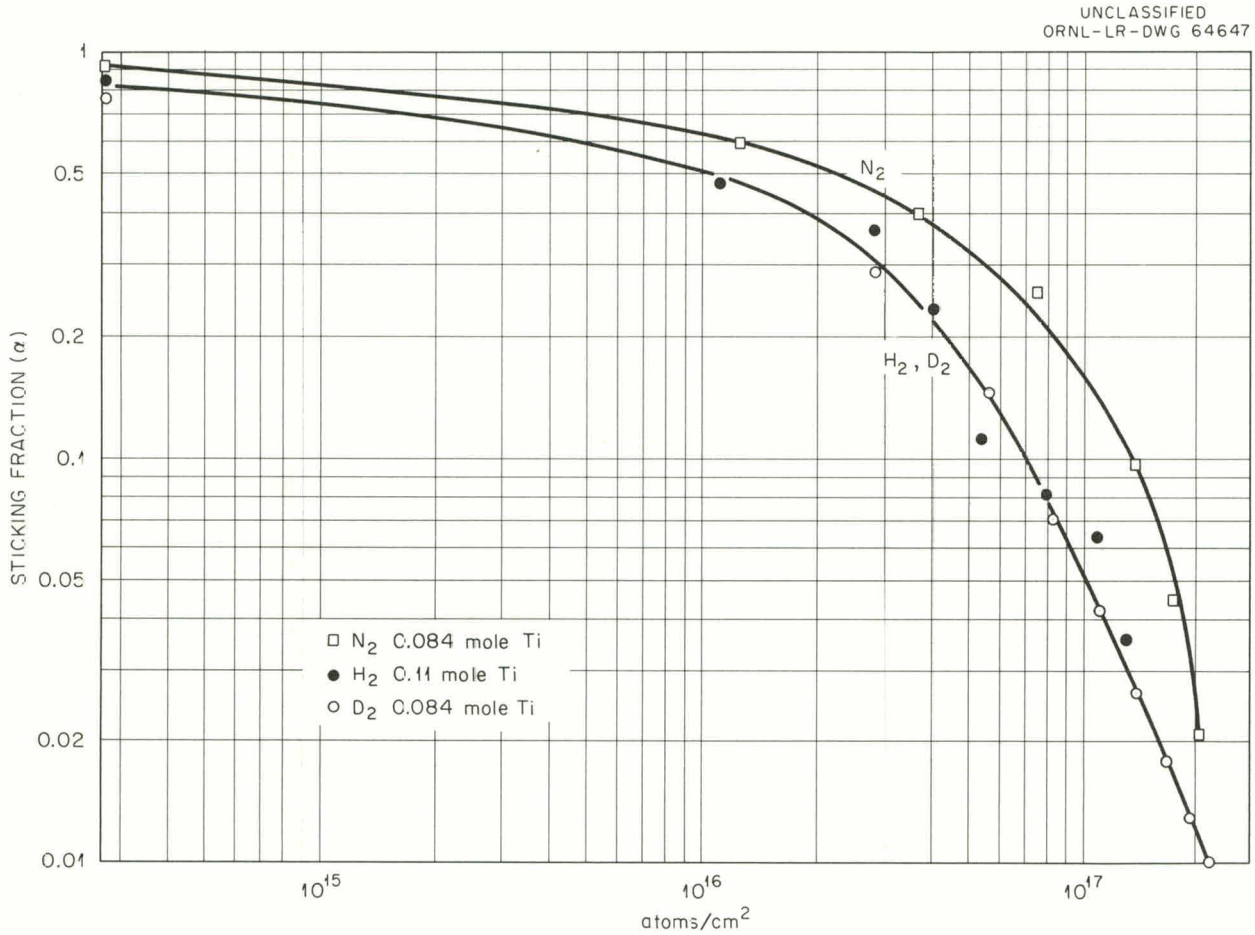

Fig. 8.6. Sorption of Gases onto Films Formed by Titanium Evaporation onto a Surface at −195°C in the Presence of 2.5×10^{-3} mm of Helium.

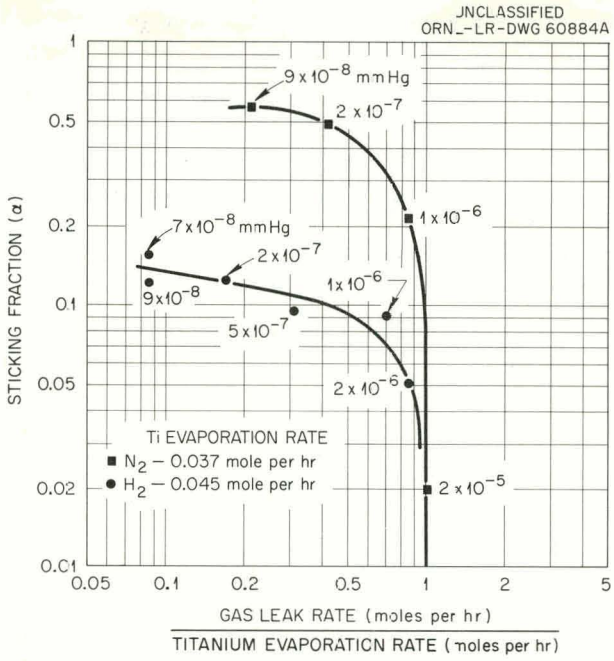

Fig. 8.7. Sorption of Gases onto Films Formed During Continuous Evaporation of Titanium onto a Surface at −195° C.

Table 8.1. Initial Sticking Fractions (α) for Various Gases on Titanium Films Deposited Under Several Conditions

Gas Species	High Vacuum, 10°C		2-μ He, 10°C	High Vacuum, −195°C		2-μ He, −195°C
	Continuous Evaporation	Batch Evaporation	Batch Evaporation	Continuous Evaporation	Batch Evaporation	Batch Evaporation
Hydrogen	0.07	0.05	0.19	0.14	0.24	0.85
Deuterium			0.14			0.78
Nitrogen	0.20[a]	0.08	0.17	0.5	0.85	0.93
Carbon monoxide	0.86	0.38	0.66		0.95	
Oxygen	0.63	0.85	0.82		0.85	
Carbon dioxide	0.5[a]	0.4[a]	0.92		0.98	
Helium	0.0005[a]					
Argon	0.0005[a]					
Methane	0.0005[a]					

[a]These data are estimated from measurements obtained from the original geometry.

8.2 VACUUM INSTRUMENTATION

8.2.1 Ionization Gage Calibrations

Two additional series of gage calibrations have been carried out using the test facility previously described.[6,7]

Calibrations of Gages in Magnetic Fields. – Ionization gages of three types (Veeco RG-75, Hughes 7169, and CVC-VG-1A) were calibrated for three orthogonal orientations in magnetic fields ranging in intensity up to 300 oersteds.

[6]C. E. Normand *et al.*, *Thermonuclear Project Semiann. Rept. July 31, 1960*, ORNL-3011, pp 129–32.

[7]C. E. Normand *et al.*, *Thermonuclear Div. Semiann. Rept. Jan. 31, 1961*, ORNL-3104, pp 133–36.

The routine given below was followed throughout this series of calibrations:

1. With the gage in any one of the chosen orientations, and with zero magnetic field, calibrations were made at a number of pressures between 10^{-6} and 10^{-4} Torr, and the average calibration factor at zero field ($\overline{f}_0$) was determined.
2. This procedure was then repeated at a series of fields (H_1, H_2, etc.), yielding average calibration factors ($\overline{f}_1$, $\overline{f}_2$, etc.).
3. For purposes of comparison, average calibration factors at the various fields were normalized to the factor at zero field ($\overline{f}_N$).
4. Steps (1), (2), and (3) were then repeated for each orientation of the gage.

The variation of gage factor (reciprocal sensitivity) as a function of field strength is shown for three orientations of the three gage studies in Figs. 8.8–8.10. Curves extend either to the maximum field available with our equipment (300 oersteds) or to the "critical field" at which the response of the gage became manifestly abnormal.

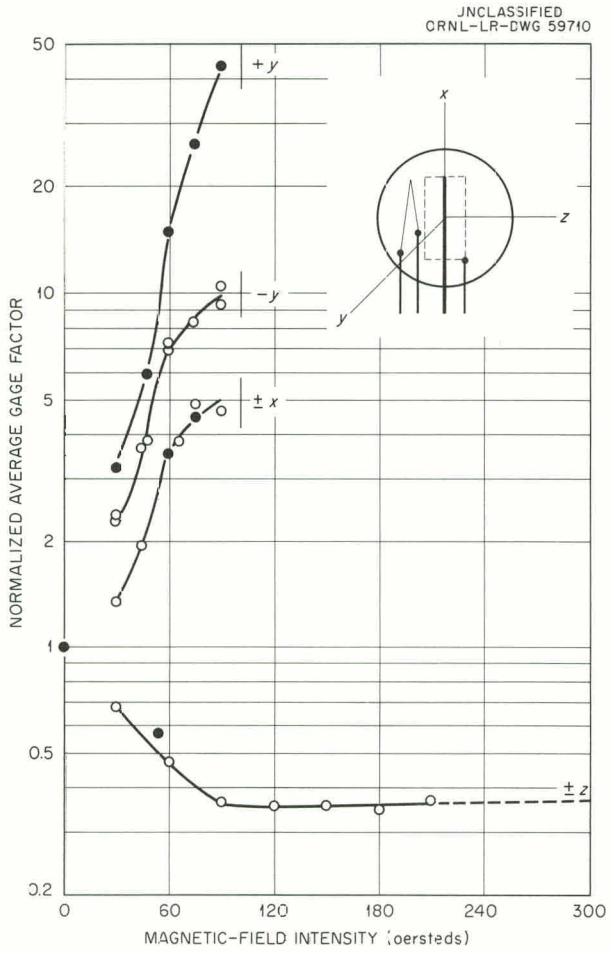

Fig. 8.8. Gage Correction Factor vs Magnetic Field Intensity. Veeco RG-75. (For coordinate system see insert.)

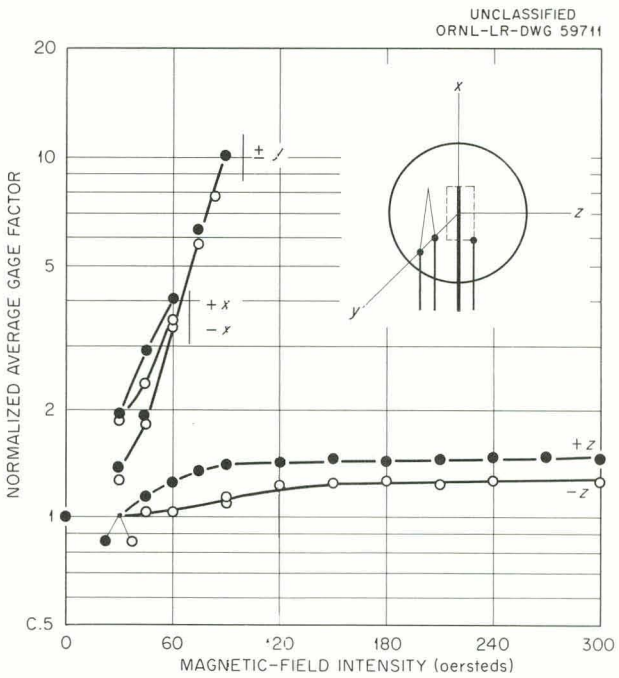

Fig. 8.9. Gage Correction Factor vs Magnetic Field Intensity. Hughes 7169. (For coordinate system see insert.)

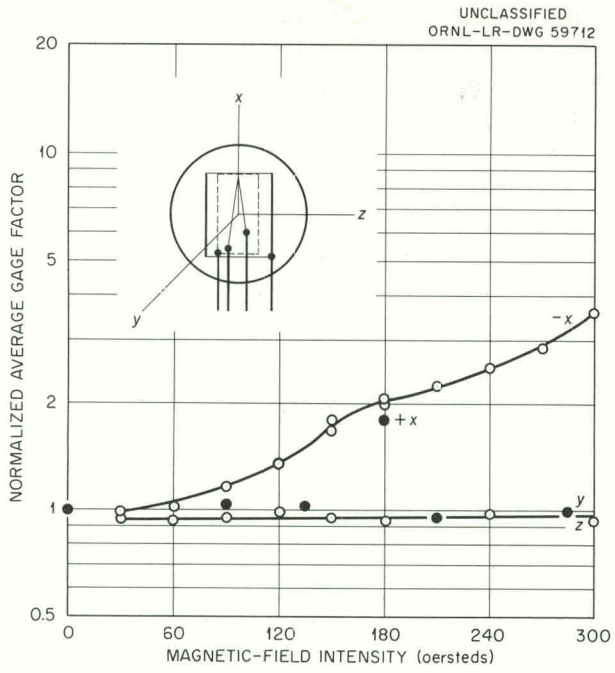

Fig. 8.10. Gage Correction Factor vs Magnetic Field Intensity. VG-1A. (For coordinate system see insert.)

This critical field was quite sharply defined by the sudden onset of one or more of the following abnormalities: (a) negative ion current, (b) deficient electron emission, (c) reduced collector potential.

The two Bayard-Alpert-type gages RG-75 (Fig. 8.8) and Hughes 7169 (Fig. 8.9) show similar characteristics. Both are quite sensitive to magnetic fields that must be crossed by electrons passing from filament to grid. Gage readings are depressed by such fields, and the field becomes critical at 100 oersteds or less. The orbital radius of 130-v electrons in a 100-oersted field is 0.38 cm. This is about equal to the filament-grid spacing. For fields parallel to the filament-to-grid direction, the electrons are accelerated along the field. In this case no critical field is observed, and the gages are much less, but not negligibly, field sensitive. For fields parallel to the tube axis, gage readings are significantly depressed. Even at the maximum applied field, however, the field does not become critical.

Calibration of Ionization Gages with Different Gases. – Two RG-75 gages were simultaneously calibrated for response to hydrogen, helium, nitrogen, argon, and air. Analysis of this work is still far from complete. It appears, however, that the relative sensitivity of these gages to the various gases studied is not significantly different from that reported by other workers for other types of gages.[8]

In the course of calibrations with air, occasion was taken to vary the humidity of the air used from dew points –78°C to +25°C. Any difference in gage sensitivity due to such a change in humidity is undetectable, and probably less than 1%.

8.3 DIFFUSION PUMPS

8.3.1 Diffusion Pump Oil Decomposition

Initial studies of pump oil decomposition were carried out by heating samples of the various oils sealed under vacuum in glass. Although the temperature used (400°C) is 150° or more higher than the usual operating temperature in a pump, the results tabulated in Table 8.2 give information about the relative stability of these materials. One may gather from these data that – excepting a catalytic effect of hot metal surfaces – the polyethers (materials with vapor pressures as low as 10^{-11} Torr at 25°C for the six-ring compound) should produce less decomposition gases in vacuum systems than presently used oils.

[8] S. Dushman, *Vacuum Technique*, p 350, Wiley, New York, 1949.

Table 8.2. Qualitative Results of Accelerated Diffusion Pump Oil Decomposition

Oil	Temperature (°C)	Time (hr)	Appearance
Convoil	400	1.0	Transparent with brown coloration
	400	7.4	Deep brown color almost opaque
	250	1.0	Slight discoloration
Octoil	400	3.3	Colorless with white solid precipitating on cooling
	450	2.3	Brown with tan precipitate
Octoil-S	400	2.3	Almost entirely converted to a white solid on cooling
Pentaphenylpolyether			
Crude	400	424	Noticeable discoloration
Purified	400	475	Some discoloration but not as much as the unpurified
Hexaphenylpolyether	400	232	Very slight discoloration

8.4 BOMBARDMENT OF TITANIUM BY D^+

No detectable sputtering of titanium by deuterium was observed in recent experiments, and a substantial fraction of the bombarding beam could be accounted for by a net increase in the weight of the titanium target. Eleven samples of titanium ($6 \times 3\frac{1}{2} \times \frac{1}{8}$ in.) were separately bombarded with D^+ ions which had been accelerated to 10–25 kev. The total flux to each of the targets was about 1.7×10^{21} particles. The data from this determination are tabulated in Table 8.3.

The background pressure (D_2) was $(2–3) \times 10^{-5}$ mm Hg. Some unknown part of the target weight increase can be attributed to pickup by the specimen after the beam was turned off. Assuming a value of 10^{-14} (cm^2 ev)/atom for the stopping cross section of titanium for deuterons, one would expect the direct penetration to be of the order of 300 A. Figure 8.11 shows a cross-sectional view of a different titanium specimen which had been bombarded for 2500 ma-hr at 25 kev at a current of 50–60 ma. Deuteride formation is apparent. X-ray diffraction patterns yield peaks characteristic of $TiD_{1.97}$ with very little discrepancy. The TiD_2 extends to a maximum depth of about 0.04 in. The thickness of the two-phase region obtained from microscopic examination is close to 0.01 cm. A diffusion constant of 10^{-6} cm^2/sec and a concentration difference of 10^{23} atoms of D per cm^3 lead to a flux of 10^{19} atoms cm^{-2} sec^{-1}. The bombarding beam at even 150 ma is but 1.5×10^{17} atoms and for the present experiment is no more than 3×10^{16} cm^{-2} sec^{-1}. It seems that the process of bombarding the surface allows the deuteron to penetrate the usual surface layer, thus allowing uptake to occur.

Table 8.3. Absorption of Energetic Deuterons by Titanium

I (ma)	Energy (kev)	ma-hr	Power Density (w/cm^2)	Input Beam Accounted for by Weight Increase (%)
28	10	829	15	15
55	15	897	34	24
48	15	721	30	93
27	20	854	225	45
48	20	717	40	80
55	20	844	45.5	85
90	20	1132	75	86
150	25	905	150	57
94	25	1099	97	78
51	25	807	54	92
74	20 (D_2^+)	813	36	69

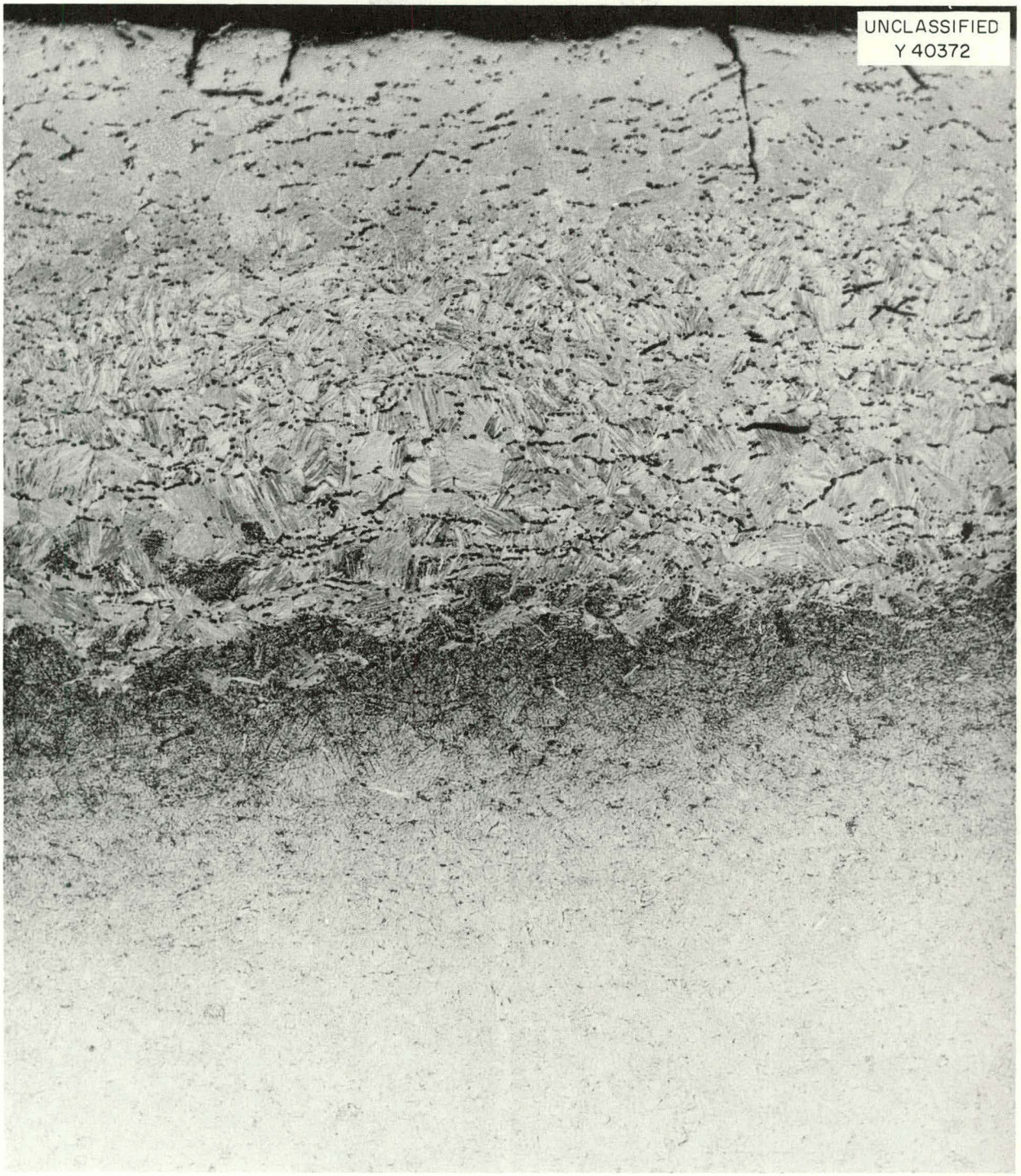

Fig. 8.11. Photomicrograph Showing the Formation of Titanium Deuteride at the Surface of a Titanium Specimen Bombarded for 2500 ma-hr at 25 kv. (The current was 50 to 60 ma.) 100X. Reduced 20%.

9. Design and Engineering

J. F. Potts, Jr.

Engineering Services Group design activities are summarized as follows:

Jobs on hand Feb. 1, 1961, on which work had not started	14
New jobs received	207
Total jobs	221
Jobs completed	189
Jobs in progress	10
Backlog of jobs Oct. 31, 1961	22
Total drawings completed for period	495
Overtime (draftsmen, man-days)	49

During this interval a significant part of the design activity was in support of DCX-2 and electron-cyclotron heating experiments. Six man-weeks of drafting help were borrowed from ORNL Engineering and Mechanical Division. One electrical and one mechanical engineer have been added to the Engineering Services Group.

Shop fabrication for the period is summarized as follows:

Jobs requiring 16 man-hours or less	222
Jobs requiring up to 1200 man-hours	530
Jobs over 1200 man-hours	8
Jobs of miscellaneous character in plating, carpenter, electrical, and millwright shops	275
Jobs by outside contractors	3

During this interval shop manpower has fluctuated from a low of 30 to a high of approximately 200 craftsmen. Since considerable fabrication was done on an accelerated program the necessary multiple-shift and overtime arrangements made an average manpower number meaningless.

In addition to a gradual upgrading of utilities and other building services, the Engineering Services Group is establishing more complete job history records. This is facilitating improvement in designs and service activities of the group.

PUBLICATIONS

OPEN LITERATURE

Author(s)	Title of Article	Journal
C. F. Barnett, J. L. Dunlap, R. S. Edwards, G. R. Haste, Herman Postma, J. A. Ray, R. G. Reinhardt, W. J. Schill, R. M. Warner, and E. R. Wells	Lifetimes of Fast Ions in the Plasma of DCX	*Phys. Rev. Letters* 6(11), 589–91 (1961)
R. J. Mackin, Jr.	Plasma Accumulation in a Device Fed by Energetic-Ion Trapping	*Nuclear Fusion* 1, 131–38 (1961)
Igor Alexeff and R. V. Neidigh	Observations of Ionic Sound Waves in Plasmas	*Phys. Rev. Letters* 7(6), 223–25 (1961)

ORNL REPORTS

Author(s)	Title	Number	Date
Albert Simon	Exact Relativistic Fokker-Planck Coefficients for Plasma and Radiation: III	ORNL-3066	3-16-61
F. T. May	The Development of a Direct Coupled, Transistorized, Sub-Millimicroampere Current Amplifier	ORNL-3098	7-28-61
C. F. Barnett, W. B. Gauster, and J. A. Ray	Atomic and Molecular Collision Cross Sections of Interest in Controlled Thermonuclear Research	ORNL-3113	5-2-61
T. K. Fowler	Plasma Stability Analysis Employing Equilibrium Constants of Motion	ORNL-3123	5-26-61
T. K. Fowler and F. M. Rankin	Energy Distribution of Ions and Electrons in DCX After Burnout: Oracle Code EDDIE	ORNL-3161	8-29-61
T. K. Fowler	Stability of Plasmas Against Electrostatic Perturbations	ORNL-3162	7-27-61
R. E. Clausing	A Large-Scale Getter Pumping Experiment Using Vapor Deposited Titanium Films	ORNL-3217	10-24-61
T. K. Fowler and E. G. Harris*	The Cyclotron Resonance Instability with Negative Mass Ions	ORNL-TM-25	10-17-61

*Consultant from the University of Tennessee

PAPERS PRESENTED AT SCIENTIFIC AND TECHNICAL MEETINGS

Optical Society of America and Conference on Analytical Chemistry and Applied Spectroscopy, Pittsburgh, Pennsylvania, March 2, 1961

J. R. McNally, Jr., P. M. Griffin, W. F. Peed, M. R. Skidmore, and G. K. Werner, "Spectroscopic Studies in the Thermonuclear Field at the Oak Ridge National Laboratory."

Second Annual Meeting, Southeastern Chapter, Society of Nuclear Medicine, Atlanta, Georgia, March 10 and 11, 1961

C. C. Harris, P. R. Bell, and J. E. Francis, "An Aural Method of Analyzing Scan Records."

Third Symposium on Temperature, Its Measurement and Control in Science and Industry, Columbus, Ohio, March 27–31, 1961

P. M. Griffin, G. K. Werner, and J. R. McNally, Jr., "Ion Energy Evaluation from Spectrum Line Contours."

Joint Symposium and Exposition of Cincinnati Sections, Society for Applied Spectroscopy and Instrument Society, Cincinnati, Ohio, April 11, 1961

P. M. Griffin, "Spectroscopy of High-Temperature Plasmas."

American Rocket Society, Gatlinburg, Tennessee, May 3–5, 1961

D. E. Harrison, Jr., and O. C. Yonts, "Survey of High-Energy Sputtering Experiments."
A. H. Snell, "The Oak Ridge DCX Program."

American Physical Society, Washington, D.C., April 24–27, 1961

Igor Alexeff and R. V. Neidigh, "Apparent Observation of Ionic Sound Waves in a Plasma."
C. F. Barnett, J. L. Dunlap, R. S. Edwards, G. R. Haste, Herman Postma, J. A. Ray, R. G. Reinhardt, W. J. Schill, R. M. Warner, and E. R. Wells, "Lifetimes of Fast Ions in the Plasma of DCX."

American Physical Society, Mexico City, Mexico, June 22–24, 1961

R. A. Gibbons and R. J. Mackin, Jr., "Properties of a Highly Ionized Steady-State Deuterium Plasma."

Fifth International Conference on Ionization Phenomena in Gases, Munich, Germany, August 28–September 1, 1961

R. A. Gibbons and R. J. Mackin, Jr., "Development and Study of a Highly Ionized Steady-State Deuterium Plasma."
R. V. Neidigh and Igor Alexeff, "Observation of Ionic Sound Waves in Gaseous Discharge Tubes."

IAEA Conference on Plasma Physics and Controlled Nuclear Fusion Research, Salzburg, Austria, September 4–9, 1961

M. C. Becker, R. A. Dandl, H. O. Eason, Jr., A. C. England, R. J. Kerr, and W. B. Ard,* "An Investigation of Electron Heating at the Cyclotron Frequency."
P. R. Bell, G. G. Kelley, N. H. Lazar, and R. J. Mackin, Jr., "The DCX-2 Program of Plasma Accumulation by High Energy Injection."
J. L. Dunlap, C. F. Barnett, R. A. Dandl, and Herman Postma, "Radiation and Ion Energy Distributions of the DCX-1 Plasma."

*Consultant from the University of Florida.

W. F. Gauster, G. G. Kelley, R. J. Mackin, Jr., and G. R. North, "Calculation of Ion Trajectories and Magnetic Fields for the Magnetic Trapping of High Energy Particles."

Albert Simon and Norman Rostoker, "Fokker-Planck Coefficients for a Plasma, Including Cyclotron Radiation."

Fourth Japan Conference on Radioisotopes, Kyoto, Japan, October 10–12, 1961

P. R. Bell, J. E. Francis, and C. C. Harris, "A Radioactivity Scanning Method Using Tracers for Diagnosis of Disease in Humans."

American Rocket Society Space Flight Report to the Nation, New York, N.Y., October 9–13, 1961

W. L. Stirling, "Experimental Investigation of Ion Beam Neutralization by Coaxially Injected Electrons."

Gaseous Electronics Conference, Schenectady, New York, October 12–14, 1961

Igor Alexeff and R. V. Neidigh, "Electron Temperatures from Ionic Sound Waves."

Second International Vacuum Conference, Washington, D.C., October 16–19, 1961

C. E. Normand, "Use of a Standard Orifice in the Calibration of Vacuum Gauges."

THIS PAGE

WAS INTENTIONALLY

LEFT BLANK

ORNL-3239
UC-20 – Controlled Thermonuclear Processes
TID-4500 (16th ed. Rev.)

INTERNAL DISTRIBUTION

1. I. Alexeff
2. R. G. Alsmiller
3. C. F. Barnett
4. M. C. Becker
5. P. R. Bell
6. D. S. Billington
7. E. P. Blizard
8. C. W. Blue
9. G. E. Boyd
10. R. L. Brown
11. R. E. Clausing
12. D. L. Coffey
13. F. L. Culler
14. J. S. Culver
15. R. A. Dandl
16. R. C. Davis
17. S. M. DeCamp
18. J. L. Dunlap
19. H. O. Eason, Jr.
20. R. S. Edwards
21. A. C. England
22. J. C. Ezell
23. J. L. Fowler
24. T. K. Fowler
25. J. E. Francis, Jr.
26. J. H. Frye, Jr.
27. W. F. Gauster
28. R. A. Gibbons
29. P. M. Griffin
30. W. R. Grimes
31. E. Guth
32. C. C. Harris
33. G. R. Haste
34. R. E. Hill
35. A. S. Householder
36. H. C. Hoy
37. R. P. Jernigan, Jr.
38. R. G. Jordan (Y-12)
39. G. G. Kelley
40. M. T. Kelley
41. R. J. Kerr
42. R. L. Knight
43. P. Lafyatis
44. J. A. Lane
45. C. E. Larson
46. N. H. Lazar
47. G. F. Leichsenrig
48. J. Lewin
49. R. S. Livingston
50. J. N. Luton, Jr.
51. J. R. McNally, Jr.
52. R. J. Mackin, Jr.
53. W. D. Manly
54. O. D. Matlock
55. K. Z. Morgan
56. O. B. Morgan
57. J. P. Murray (K-25)
58. R. V. Neidigh
59. M. L. Nelson
60. J. Neufeld
61. C. E. Normand
62. C. E. Parker
63. W. F. Peed
64. D. Phillips
65. H. Postma
66. J. F. Potts
67. M. Rankin
68. J. A. Ray
69. R. G. Reinhardt
70. P. W. Rueff
71. W. K. Russell
72. H. E. Seagren
73. Y. Shima
74. E. D. Shipley
75. M. R. Skidmore
76. M. J. Skinner
77. A. H. Snell
78. W. L. Stirling
79. R. F. Stratton, Jr.
80. R. A. Strehlow
81. J. A. Swartout
82. E. H. Taylor
83. P. A. Thompson
84. R. M. Warner
85. H. L. Watts
86. A. M. Weinberg
87. E. R. Wells
88. T. A. Welton

89. G. K. Werner
90. C. E. Winters
91. W. L. Wright
92. O. C. Yonts
93. W. P. Allis (consultant)
94. W. B. Ard, Jr. (consultant)
95. J. F. Bailey (consultant)
96. W. H. Bostick (consultant)
97. W. R. Chambers (consultant)
98. F. E. Dunnam (consultant)
99. J. W. Flowers (consultant)
100. M. W. Garrett (consultant)
101. E. G. Harris (consultant)
102. D. E. Harrison (consultant)
103. O. G. Harrold, Jr. (consultant)
104. R. Hefferlin (consultant)
105. G. W. Hoffman (consultant
106. V. W. Hughes (consultant)
107. D. W. Kerst (consultant)
108. E. W. McDaniel (consultant)
109. M. R. C. McDowell (consultant)
110. J. E. Mott (consultant)
111. W. B. Pardo (consultant)
112. F. F. Rieke (consultant)
113. H. S. Robertson (consultant)
114. D. J. Rose (consultant)
115. L. P. Smith (consultant)
116. H. S. Snyder (consultant)
117. P. M. Stier (consultant)
118. C. H. Weaver (consultant)
119. A. Simon (consultant)
120. J. D. Tillman (consultant)
121. Thermonuclear Division Library
122. Reactor Division Library
123. Biology Library
124-126. Central Research Library
127-151. Laboratory Records Department
152. Laboratory Records, ORNL RC
153-154. ORNL – Y-12 Technical Library, Document Reference Section

EXTERNAL DISTRIBUTION

155. S. C. Brown, Massachusetts Institute of Technology
156. M. B. Gottlieb, Princeton University
157. J. M. B. Kellogg, Los Alamos Scientific Laboratory
158. A. C. Kolb, Naval Research Laboratory
159. J. A. Phillips, Los Alamos Scientific Laboratory
160. R. F. Post, University of California, Lawrence Radiation Laboratory
161. E. Teller, University of California, Lawrence Radiation Laboratory
162. C. M. Van Atta, University of California, Lawrence Radiation Laboratory
163-164. Research and Development Division, AEC, ORO (1 copy each to H. M. Roth and R. B. Martin)
165-166. Controlled Thermonuclear Branch, AEC, Washington (1 copy each to A. E. Ruark and H. S. Morton, Jr.)
167. R. W. McNamee, Union Carbide Corporation
168. E. P. Gyftopoulos, Massachusetts Institute of Technology
169-774. Given distribution as shown in TID-4500 (16th ed., Rev.) under Controlled Thermonuclear Processes category (75 copies – OTS)